

Magnetic and Transport Properties of $\text{YBa}_2\text{Cu}_3\text{O}_7 - \text{La}_{0.7}\text{Ca}_{0.3}\text{MnO}_3$ Heterostructures

Von der Fakultät Mathematik und Physik der Universität Stuttgart
zur Erlangung der Würde eines
Doktors der Naturwissenschaften (Dr. rer. nat.)
genehmigte Abhandlung

Vorgelegt von

Luqman Mustafa

aus Zarqa, Jordanien.

Hauptberichter:

Prof. Dr. B. Keimer

Mitberichter:

Prof. Dr. M. Dressel

Prüfungsvorsitzende:

Prof. Dr. M. Daghofer

Tag der Einreichung:

31.10.2016

Tag der mündlichen Prüfung:

25.11.2016

Max-Planck-Institut für Festkörperforschung, Stuttgart
Universität Stuttgart
Stuttgart 2016

Table of Contents

Chapter 1: Introduction ...	9
Chapter 2: Overview	17
2.1 Cuprate Superconductors	17
2.1.1 High T_c superconductivity	17
2.1.2 Properties of $\text{YBa}_2\text{Cu}_3\text{O}_{7-\delta}$	19
2.2 Manganites	24
2.2.1 Manganites in complex oxide research	24
2.2.2 The role of chemical composition and structure in LCMO	26
2.2.4 Strain effects	31
2.2.5 Oxygen stoichiometry effect.....	32
2.3 YBCO-LCMO heterostructures	33
2.3.1 General remarks on complex oxide heterostructures and superlattices	33
2.3.2 Superconductivity and ferromagnetism	34
2.3.2 c-axis oriented YBCO-LCMO heterostructures and superlattices	36
Chapter 3: Experimental techniques	43
3.1 PLD technique – general description	43
3.2 Essentials of thin film nucleation and growth	46
3.3 Optimized growth process for YBCO-LCMO heterostructures	51
3.4 Thin Film characterization techniques	54
3.4.1 Structural and microscopic analysis.....	54
3.4.2 Magnetometry	54
3.4.3 Transport measurement	56
3.3.5 Raman spectroscopy	58
Chapter 4: Results and discussions	61
4.1 (110)-oriented YBCO and LCMO thin films	61
4.1.1 (110)-oriented YBCO thin films	61
4.1.2 LCMO (110)-oriented films	69
4.2 (110)-Oriented YBCO-LCMO Heterostructures.....	71
4.3 FSF LCMO/YBCO/LCMO (LYL) Trilayers	77

4.4 SFS YBCO/LCMO/YBCO (YLY) (110)-oriented Trilayers	86
Chapter 5: Conclusions and Outlook	97
References	99
Acknowledgements	109
Publication list	111

Abstract (English)

The exploration of interface properties in complex oxide heterostructures and superlattices is one of the new exciting fields in condensed matter sciences. This is particularly originating from the technological advances in synthesizing heterostructures with atomic scale precision by advanced thin film deposition techniques. There is a plethora of novel achievements culminating in unexpected results, such as generating artificial multifunctional materials with the prominent example of the appearance of interface electrical conductivity and even superconductivity in between insulating films ($\text{SrTiO}_3 - \text{LaAlO}_3$).

In this thesis a special case of heterostructures is treated. Here, heterostructures composed of superconducting $\text{YBa}_2\text{Cu}_3\text{O}_7$ and half-metallic ferromagnetic $\text{La}_{2/3}\text{Ca}_{1/3}\text{MnO}_3$ are investigated and the interplay of the two long-range antagonistic ordering principles – superconductivity and ferromagnetism - is intended to be studied. Whereas the physics of such structures with the CuO_2 planes of the superconducting $\text{YBa}_2\text{Cu}_3\text{O}_7$ oriented parallel to the substrate plane (i.e. the short coherence length of the superconductor, $\xi_c \sim 0.1$ nm is facing the interface perpendicular) has been explored in great detail, little is known in the case of the CuO_2 planes oriented perpendicular to the substrate plane and thus $a_b \sim 1.6$ nm is pointing perpendicular to the interface. In the former case, the properties of the heterostructures and superlattices are determined by an interplay of charge transfer and orbital reconstruction, but the mechanisms occurring in the latter case are unknown so far. Prior to elaborated experiments to study the interface properties at an atomistic scale, the technology of fabricating such structures has to be accomplished and their macroscopic properties (structure, transport and magnetic properties) have to be investigated. It is the goal of this thesis to prepare the ground for the atomistic studies by developing the technological prerequisites for the growth of (110)-oriented YBCO-LCMO heterostructures and characterize their structural, electric and magnetic macroscopic properties. Due to the sensitivity of the macroscopic properties of such structures to the crystallographic perfection of the interfaces a substantial part of this thesis is devoted to the corresponding enabling technology. Advanced PLD techniques are used to fabricate single layer (110)-oriented YBCO and LCMO films, bilayers as

well as twin-free (103)-oriented LCMO-YBCO-LCMO trilayers and (110)-oriented YBCO-LCMO-YBCO structures with ultrathin LCMO films (nominally 1-2 nm) in between 50 nm YBCO. These (110)-oriented trilayers serve as a precursor for a prototype planar Josephson junction technology. A comparison of the experimental results for (001) and (110) – oriented heterostructures reveals distinct changes in the ordering temperatures T_c and T_{Curie} giving a fingerprint of different microscopic mechanisms taking place at the interfaces. Furthermore, in the twin-free (103)-oriented trilayer samples a novel positive Meissner effect has been observed which is ascribed to the magnetic domain arrangement of the LCMO.

Abstract (Deutsch)

Gegenwärtig stellt die Erforschung der physikalischen Eigenschaften oxidischer Heterostrukturen einen faszinierenden neuen Zweig der Festkörperforschung dar. Die erzielten Fortschritte auf diesem Gebiet sind wesentlich auf die Entwicklungen bei der Synthese dünner Schichten und Heterostrukturen zurückzuführen, die mittlerweile die Präzision atomarer Skalen erreicht hat. An Heterostrukturen und Übergittern wurden bereits eine Vielzahl unerwarteter Ergebnisse erzielt, wobei künstliche multifunktionale (z. B. multiferroische) Systeme und das Auftreten elektrisch leitender Grenzflächen zwischen Bandisolatoren als prominente Beispiele dienen.

In dieser Dissertation wird ein spezielles Beispiel solcher Heterostrukturen behandelt. Vielsichtsysteme bestehend aus supraleitendem $\text{YBa}_2\text{Cu}_3\text{O}_7$ (YBCO) und halbmetallischem ferromagnetischem $\text{La}_{2/3}\text{Ca}_{1/3}\text{MnO}_3$ (LCMO) werden hergestellt und mit der Zielsetzung untersucht, ein vertieftes Verständnis für die Wechselwirkung langreichweitiger gegensätzlicher Ordnungsprinzipien (Ferromagnetismus und Supraleitung) zu erzielen. Während solche Untersuchungen bereits am System YBCO-LCMO durchgeführt wurden, in dem die CuO_2 -Ebenen des Kuprats parallel zur Substratoberfläche und damit die kurze Kohärenzlänge des Supraleiters, ξ_c , senkrecht zur Grenzfläche orientiert sind, wurden bisher Systeme mit den CuO_2 -Ebenen senkrecht zur Substratoberfläche und damit die grosse Kohärenzlänge, ξ_{ab} , senkrecht zur Grenzfläche kaum untersucht. Die vorgelegte Dissertation stellt einen Beitrag dar, diese Lücke zu füllen. Im ersten Fall (CuO_2 parallel zur Filmebene) hat sich gezeigt, dass die Wechselwirkung der ferromagnetischen und der supraleitenden Lagen durch Ladungsaustausch und Rekonstruktion der Atomorbitale an der Grenzfläche charakterisiert und für die makroskopischen Effekte (Reduktion der Sprungtemperatur, T_C , und der Curietemperatur, T_{Curie}) verantwortlich ist. Entsprechende Untersuchungen für den Fall der CuO_2 -Ebenen senkrecht zur Filmebene fehlen weitgehend. Bevor solche Experimente durchgeführt werden können, müssen die technologischen Voraussetzungen der Synthese solcher Vielfachschichten erfüllt sein. Es ist das Ziel dieser Arbeit, die technologische Basis für solche Untersuchungen zu legen, phasenreine (110)-orientierte YBCO-LCMO Heterostrukturen herzustellen und ihre

strukturellen, elektrischen und magnetischen makroskopischen Eigenschaften zu untersuchen. Wegen der Empfindlichkeit solcher Strukturen bezüglich der kristallographischen Perfektion der Grenzflächen ist ein substantieller Teil der Arbeit der Technologie der Präparation der (110)-orientierten Einzelschichten, Zwei- und Dreilagensysteme wie auch zwillingsfreier (103) Dreilagensysteme gewidmet. (110)-orientierte YBCO-LCMO-YBCO Dreilagensysteme mit ultradünner LCMO-Schicht (1-2 nm) wurden hergestellt und untersucht, um den Weg zu einer planaren Josephson-technologie mit magnetischen Barrieren zu bereiten. Der Vergleich der makroskopischen magnetischen und elektrischer Eigenschaften (001)- und (110)-orientierter Heterostrukturen zeigt eine stärkere Reduktion der supraleitenden Sprungtemperatur wie auch der Curietemperatur bei den (110) Schichten. Dies kann als Hinweis auf Unterschiede bei den mikroskopischen Mechanismen gewertet werden, die an den Grenzflächen zwischen YBCO und LCMO auftreten. Bei den (103)-orientierten Zweilagensystemen wurde darüber hinaus ein bisher kaum beachteter positiver Meissner Effekt nahe der supraleitenden Übergangstemperatur beobachtet, der auf die magnetische Domänenstruktur der LCMO Schicht zurückgeführt werden kann.

CHAPTER 1

Introduction

Amongst the solid inorganic materials, oxides display perhaps the most diverse range of functionality. The nature of cation–oxygen bonding results in electronic properties that can be described within the context of a combination of solid state band theory and ionic bonding concepts derived by solid-state chemistry. It results in an interplay between localized and itinerant character of the electrons that is superimposed by strong electron-electron correlation and lattice effects arising from the crystal field of the oxygen octahedra and Jahn-Teller distortion of the oxygen sublattice surrounding those cations. Their degenerate electronic ground state is lifted by a structural distortion, thus lowering the total energy. Additionally, the interaction between charge-, orbital-, spin- and lattice degrees of freedom can cause drastic changes in the electronic properties upon subtle extrinsic perturbations. The metal oxide materials possess a wide range of electronic properties. Closed shell compounds, such as Al_2O_3 and TiO_2 with a strong ionic character of the bonds are insulators with large band gaps. For closed-shell oxides based on cations with high electronegativity, such as in ZnO and SnO_2 , the more covalent nature of bonding yields semiconductors with relatively high carrier mobility.

Transition metal oxides with more than one cation frequently crystallize in the perovskite structure with the general formula ABO_3 where A and B are the large and small (mostly the transition metal) cations, respectively. Fig. 1 shows a typical example of a perfect perovskite structure, where A corresponds to Ca, B to Ti, forming the parent compound CaTiO_3 , a mineral found in the Ural mountains with the name perovskite, a name coined by the Russian mineralogist L.A. Perovski.

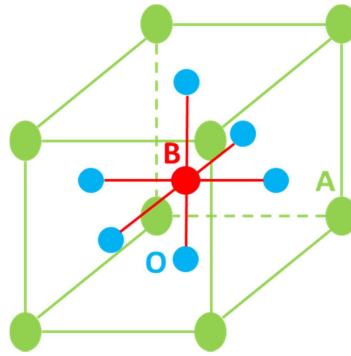


Fig. 1: Perfect structure of a ABO_3 perovskite (green Ca, red Ti, and blue oxygen)

Oxides with partial filling of the conduction band containing transition metal cations with a tendency to form mixed valence compounds, can yield either Mott-insulators ($LaMnO_3$) or high conductivity metals, such as $SrRuO_3$, or even superconductors with $YBa_2Cu_3O_7$ as the most popular representative. Collective phenomena involving electric dipole interactions in insulators can give rise to ferroelectricity such as in $BaTiO_3$. Ordering in the spin system may result in nearly all varieties of magnetism ranging from ferromagnetism (CrO_2), antiferromagnetism ($LaMnO_3$) to ferrimagnetism, as in Fe_3O_4 . Furthermore, many oxides display interesting metal–insulator transitions that are dependent on temperature (V_2O_3), pressure (NiO), or magnetic field ($(La,Sr)MnO_3$). In addition to all this, the topic of electronic inhomogeneity in chemically and crystallographically homogeneous systems has attracted much attention, recently (mesoscopic phase separation). The whole field is covered in several books and review papers mainly describing the crystal chemistry of complex oxides, their physical properties and the structure – property relations [1-3]. The attraction of the complex oxide systems with the perovskite structure is that they can be found in almost every possible (even macroscopically ordered) electronic ground state such as metals, insulators, superconductors, ferromagnets, ferroelectrics, multiferroics and more. Many of the perovskites have a transition metal as one cation component whose valency can be changed in a wide range by partial substitution of A-site cations with different valency, thus generating a mixed valence state of it with implications on the spin arrangement and spin dynamics. Frequently, they show strong electron correlations causing a competition between lattice, orbital, charge and spin interactions. Due to the balance between kinetic energy and Coulomb repulsion, these

systems tend to stabilize different phases with energetically slightly different ground states that can easily be converted upon small extrinsic perturbations in temperature, electric or magnetic fields or mechanical strain. The specimens to be studied in physics experiments cover the whole range from single crystals, bulk ceramics and especially single-crystal-type thin films. Whereas the exploration of the conditions for epitaxial thin film growth of complex oxides and the interrelation between growth conditions, microstructure and physical properties is already a research field of growing interest, in the past few years, activities emerged with the goal to prepare heterostructures with components of different functionality. The enabling technologies to pursue this goal are based on the advancements of thin film deposition methods suitable to prepare thin films of complex oxides with the precision of one unit cell (typically $\sim 4\text{\AA}$). They include Pulsed Laser Deposition (PLD) and Oxide Molecular Beam Epitaxy (MBE).

Artificial superlattices (SL's) represent a well-established research topic in condensed matter physics and modern device technology. Semiconductor heterostructures and SL's have proven to form the basis for unexpected advances in science and device physics over the past decades. A prominent example is the formation of a 2-dimensional electron gas in III-V-compound semiconductor heterostructures or in silicon metal-oxide-semiconductor field-effect transistors with the subsequent discovery of the quantum Hall effect by von Klitzing et al. [4]. Similarly, metallic SL's consisting of paramagnetic and ferromagnetic layers give rise to a giant magnetoresistance [5], a discovery that made a fast implementation into practical devices. They serve now as sensing elements in reading heads of hard disk drives. The attempt to replicate such SL's using transition metal oxides (TMO's) will pave the way for an even more exciting research area due to the delicate interplay of spin-, charge-, orbital and lattice interactions of electrons arising from the sensitivity of the orbital ordering patterns of electrons in the 3d shells to external perturbations such as strain, electrical and magnetic fields, photon flux etc. Combining such TMO's in heterostructures (HS's) or SL's gives rise to expectations that at their interfaces novel correlation driven quantum states are appearing with functionalities qualitatively beyond those attainable in metals or semiconductors. Based on the improvement of the technological basis to prepare high quality complex oxide thin films (COTF's) and HS's this field has attracted

increasing interest in the science community in the past decade and is listed amongst the “runners-up” within the “breakthrough of the year 2007” in Science magazine [6-10]. Recently, several review papers covering the field of oxide electronics have been published in the MRS Bulletin [11] as well as by Mannhart et al. and Hwang et al. [12, 13].

Complex oxides with strong electron correlation are characterized by a fierce competition between lattice-, orbital-, charge- and spin ordering, all of them occurring at similar energy scales. The electron-electron correlations are related to parameters such as the on-site Coulomb repulsion energy and the exchange energies, J . Candidates for heteroepitaxial thin film growth of complex oxides can be chosen from a long list of materials with nearly perfect lattice match and good chemical compatibility. Thus, structurally highly ordered interfaces are achieved with negligible cation interdiffusion. Ohtomo et al. observed electrical conductivity at the interface of two band insulators [6] such as SrTiO_3 and LaAlO_3 and interpreted that unexpected finding by the formation of a 2-D electron gas originating from a charge transfer from polar to nonpolar surfaces of LaAlO_3 and SrTiO_3 , respectively, to avoid what is described in the literature as polar catastrophe. Fig. 2 shows this model to explain the interface conductivity, schematically.

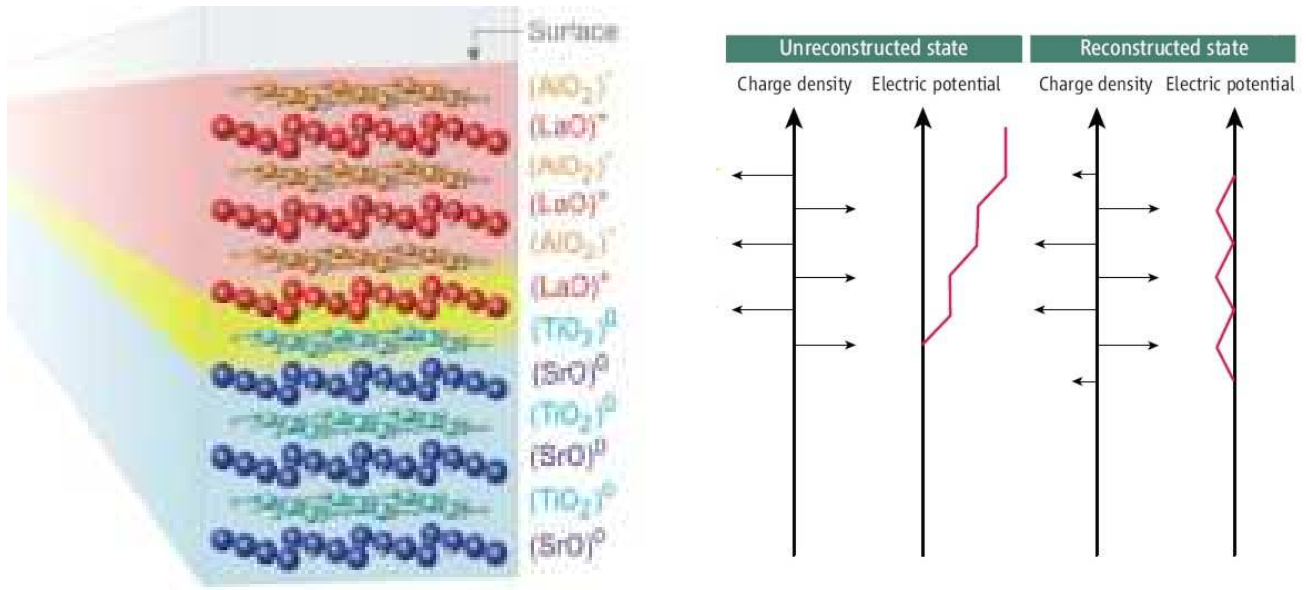


Fig. 2: Explanation of the interface conductivity in the SrTiO₃ / LaAlO₃ system [6].

Changes in the bonding characteristics at the interface may modify the spin properties due to the strong interaction between the spin and orbital degrees of freedom. Furthermore, electronic reconstruction at the interface in conjunction with broken lattice symmetry modifies the orbital state at the interface thus affecting the exchange interactions [14]. Consequently, the physical properties of an interface dominated sample will be different from those of the individual layers and the simple picture of a linear combination of the properties of both constituents – albeit modified by strain effects – is far from the reality.

A special topic in this field is to combine materials with different ground states (functionalities) with long range order in the form of epitaxially grown thin film hybrids and to investigate the mutual interaction of the long range order. Oxide ferromagnets (FM) and high temperature cuprate superconductors (HTSC) serve as prototypes for the combination of such materials. Whereas the oxide ferromagnets used in these investigations are mainly perovskites with nominally cubic symmetry, the superconducting part consists of YBa₂Cu₃O₇ whose structure can be approximated by tripled perovskite-type elements. In Fig. 3 the basic structure of YBa₂Cu₃O₇ is depicted. It is obvious that due to the crystallographic anisotropy, based on the

It is the goal of this thesis to prepare YBCO/LCMO heterostructures and superlattices where CuO_2 planes with the long coherence length, $\xi_{a,b} \sim 20 \text{ \AA}$ are perpendicular to the interface and thus to explore the electronic interaction of the ferromagnetic and the superconducting parts of the heterostructures at a longer length scale. The prerequisite to achieve this goal is the fabrication of film heterostructures and superlattices with the (110)-film plane parallel to the substrate (c.f. Fig. 4a)

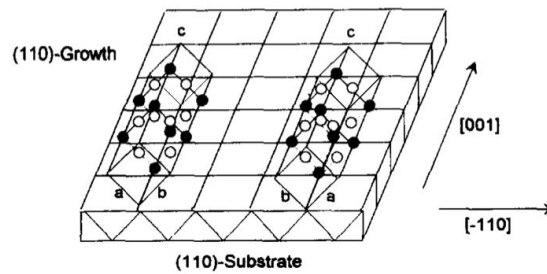


Fig. 4a: Schematic representation of YBCO growth in (110) orientation on a (110)-oriented lattice matched substrate [21].

Additionally, heterostructures and superlattices will be investigated in the YBCO (103)-orientation; here, $\xi_{a,b}$ is oriented 45° with respect to the film plane (see Fig. 4b).

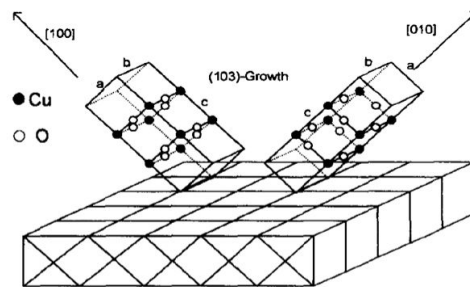


Fig. 4b: Schematic representation of YBCO growth in competing (103)/(103̄) orientations on a (110)-oriented lattice matched substrate [21].

Using a slight miscut of the (110)-oriented SrTiO₃ substrate ensures the suppression of the YBCO (a,b) twinning, usually inherent to YBCO thin film growth. A large part of this thesis deals with these technological prerequisites and ways to overcome the problems of growth of single layer films, heterostructures and superlattices with these special orientations. Success in technology precedes success in physics.

This thesis is organized as follows:

In Chapter 2 an overview over the basic crystallographic properties of the materials (YBCO, LCMO) as well as a summary of the experiments on (100)-oriented YBCO/LCMO heterostructures and superlattices are given. Chapter 3 deals with the fundamentals of complex oxide thin film heterostructure growth and the experimental techniques to analyze their properties. The main part is presented in Chapter 4 where single layer (110)-oriented YBCO films are analyzed and the implications of strain and oxygen stoichiometry of (110)-oriented LCMO films are discussed. The main part of this chapter deals with the fabrication of (110)-oriented YBCO-LCMO heterostructures and their properties, results of (103) – oriented bi- and trilayers and finally with (110)-oriented YBCO-LCMO-YBCO trilayers where ultrathin ferromagnetic barriers are used to pave the way for the fabrication of planar Josephson junctions of the SFS-type and address potential approaches to unconventional pairing mechanisms. In Chapter 5 the work will be summarized.

CHAPTER 2

Overview

2.1 Cuprate Superconductors

2.1.1 High T_c superconductivity

Liquefaction of Helium in 1908 by the Dutch physicist Heike Kamerlingh Onnes opened the door to a new era of experimental low temperature physics. In 1911 he observed a vanishing resistance in mercury by exploring the low temperature resistance behavior of pure metals. The resistance of mercury drops to a value below the experimental detection limit near the boiling temperature of liquid helium of 4.2 K and he named this unexpected phenomenon superconductivity [22]. At a later date, in 1933, W. Meissner and R. Ochsenfeld demonstrated that the superconducting state exhibits perfect diamagnetism as the magnetic flux is expelled from the material in the superconducting state in weak magnetic fields [23]. These combined properties, the vanishing of electrical resistance and the perfect diamagnetism in weak magnetic fields constitute the fundamental properties of superconductors. Afterwards, a number of other elements like Al, Bi, Zn, Nb etc. and different alloys were shown to be superconducting. In the early 1950`s, the critical temperature, T_c , of the superconductors was shown to be sensitive to the isotopic mass of the constituent elements, pointing towards a role of phonons in models developed to explain superconductivity [24]. This observation led to the major theoretical breakthrough in 1957 where a microscopic theory of superconductivity was introduced by Bardeen, Cooper and Schrieffer, abbreviated as BCS theory, which explained quite well superconductivity in metallic superconductors like elements and alloys [25]. The BCS theory interpreted the occurrence of superconductivity by the formation of electron pairs,

called Cooper pairs, resulting from the attractive interaction of electrons with opposite spins and momenta near the Fermi surface, mediated by the lattice vibration of ions. The Cooper pairs are composite Bosons and are not subjected to scattering by lattice imperfections (like electrons which are Fermions) and can condense to a common ground state that causes the peculiarities of superconductivity.

Since the discovery of superconductivity about 100 years ago, research efforts are aimed to find materials with higher T_c 's. Until the early 80's of the last century the record for the highest T_c was held by an intermetallic compound Nb_3Ge crystallizing in the A-15 structure with a T_c of 23.3 K. [26] In 1986, J.G. Bednorz and K.A. Muller discovered superconductivity in the ceramic La-Ba-Cu-O cuprate system with a T_c of about 35 K [27], which is considered as the beginning of the field of high temperature superconductivity. Their search for new superconductors was stimulated by the ideas of Jahn- Teller based polaronic effects which could be of major importance for the formation of electron pairs and thus superconductivity. This discovery was a breakthrough in the field of superconductivity and was followed by avalanche-like activities in searching for materials with higher superconducting transition temperatures T_c . Just after one year, in 1987, Wu et al. found a multiphase Y-Ba-Cu-O cuprate system to be superconducting at 93K that is well above 77K the boiling temperature of liquid nitrogen [28] thus opening the possibilities for applications in an experimentally much more easily accessible temperature range. The superconducting phase in Y-Ba-Cu-O system was identified as $YBa_2Cu_3O_{7-\delta}$ – abbreviated as YBCO in the following. [29] Since then, different structural and physical properties of cuprates have been extensively studied and to raise the T_c for these materials by cation substitution has been extensively investigated. At present the highest T_c , of 133K is found in the mercury-cuprate system which increases to $\sim 150K$ under high pressure conditions [30].

Whereas the pairing mechanism of electrons to form Cooper-pairs in conventional metallic superconductors is identified to be phonon mediated, and the BCS theory gives framework to describe their physical properties, for the cuprate superconductors a generally accepted unified theoretical picture has not emerged. 20 years after the discovery of HTS Zaanen [31] organized

a collection of opinions towards a complete theory of high T_c where the major players in theory expressed their opinions about the origin of HTC; they range from polaron-bipolaron mechanisms to t-J and spin fluctuation models. Extensive experimental work using improved techniques have helped researchers to weed out the more exotic theories and refine those that remain. Currently two main directions are pursued. The first, resonating-valence-bond theory, is largely the creation of Philip Anderson. The theory states that the electron-pairing mechanism is imprinted in the cuprates' structure. Neighbouring copper atoms can become linked through chemical valence bonds, in which they share electrons with opposite spins. Typically, the bonding locks these spin pairs in place, preventing any current from being carried. But when the material is doped, the pairs become mobile and the valence bonds become Cooper pairs that condense into a superconducting state [32].

The second theory, called spin fluctuation, has the strongest support in the community. It postulates that without doping, cuprates are locked into an ordered state called an antiferromagnet [33]. That means that the outer electron on each copper atom lines up such that its spin is opposite to that of its neighbor: one electron will have its spin up, the next down, the next up, and so on. The magnetic fields produced by the spins lock the electrons in place. But in doped cuprates, mobile charge carriers break up this rigid checkerboard pattern, giving the spins room to wobble. A passing electron can then set up a pulsating pattern of spins analogous to the lattice distortions of conventional superconductivity. This disturbance then draws moving electrons together, allowing them to associate into Cooper pairs and achieve a superconducting state.

2.1.2 Properties of $\text{YBa}_2\text{Cu}_3\text{O}_{7-\delta}$

Since in this thesis exclusively YBCO is used as the superconducting layer material in the heterostructures and superlattices, its structural and physical properties are described in some detail.

Crystal structure

YBCO has layered structure which could be described as distorted, oxygen deficient perovskite of the form ABO_3 tripled along the c -axis, where Y and Ba are central cations A which are stacked in -Ba-Y-Ba- sequence and Cu is the corner cation B. [34] Yttrium is coordinated to 8 oxygen atoms forming a square prism while Barium is coordinated to 10 oxygen atoms. The valence of Y and Ba are +3 and +2, respectively, while Cu has mixed valence of +2 or +3 to ensure charge neutrality. The structure of stoichiometric superconducting $YBa_2Cu_3O_{7-\delta}$ is orthorhombic belonging to P_{mmm} symmetry, however highly oxygen deficient non-superconducting $YBa_2Cu_3O_{7-\delta}$ with $\delta > 0.6$ has tetragonal structure with $P_{4/mmm}$ symmetry (see Figure 5 of YBCO structures O_6 -tetragonal- and O_7 - orthorhombic).

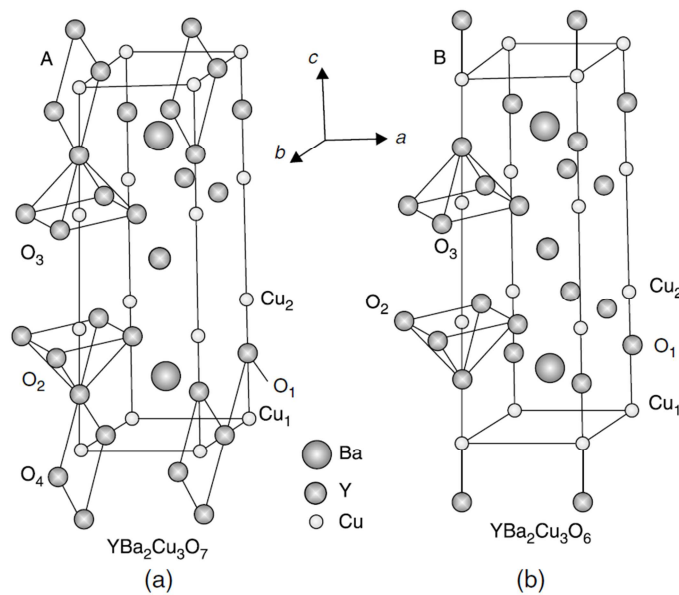


Fig. 5: $YBa_2Cu_3O_6$ (right) and $YBa_2Cu_3O_7$ (left) taken from [35].

Cu_1 is at the center of a rectangle formed by its coordination with two O_1 and two O_4 atoms, these rectangles are connected by the vertices and give rise to CuO chains along b -axis. Cu_2 is coordinated in the form of square pyramid to two O_2 and two O_3 atoms in the a - b plane and one O_4 atom along the c -axis. [36] CuO_2 planes formed by Cu_2 , O_2 , and O_3 atoms are extended infinitely in the specimen and are crucial to determine the transport and superconducting properties of the material. For $\delta = 0$, i.e., $YBa_2Cu_3O_7$ the oxygen sites along a -axis in the basal

CuO chain plane are completely empty. With increasing δ , the one dimensional chains in the orthorhombic phase are disrupted by an increasing number of oxygen vacancies at the O_4 site along b-axis. All oxygen sites in the basal plane become empty for $\delta = 1$, i.e. $YBa_2Cu_3O_6$ [36]. The lattice parameters for this material are $a = 3.822 \text{ \AA}$, $b = 3.891 \text{ \AA}$ and $c = 11.677 \text{ \AA}$ making the unit cell volume 3 times the standard perovskite cell [28].

Phase diagram

Hole doped cuprates have a generic phase diagram of their phase evolution in terms of temperature vs. hole doping as depicted in figure 6. The insulating parent compound $YBa_2Cu_3O_6$ is an antiferromagnetic Mott insulator [37]. It can be doped either by substituting trivalent cations with divalent ones (such as, Ca) as in the case of La_2CuO_4 or by oxygen filling the Cu-O chains. With increasing doping, the antiferromagnetic transition temperature is rapidly suppressed and becomes zero; upon further increase of the doping level the superconducting state emerges with low T_c at the beginning. T_c gradually increases with the doping level, reaching a maximum at ~ 0.16 and then falls down slowly to zero. The shape of the curve T_c vs. doping level looks like a dome. The region in the phase diagram where T_c increases with increasing doping level is called underdoped region and the one where T_c decreases is called overdoped region. The doping level where T_c has maximum is called optimal doping level.

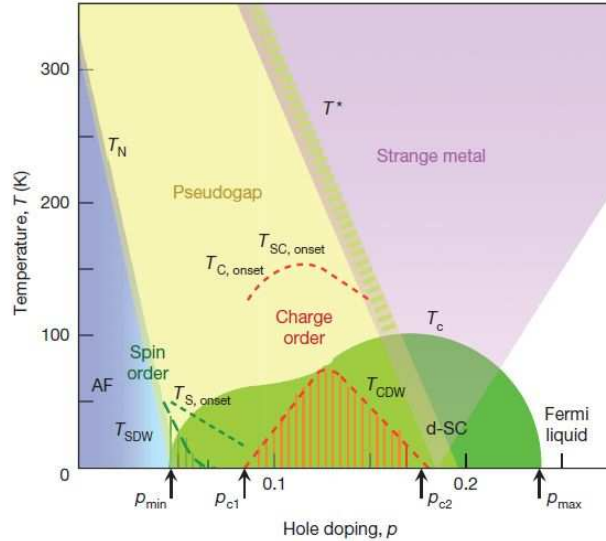


Figure 6: Phase diagram Temperature versus hole doping level for the copper oxides, indicating where various phases occur. (taken from ref [38])

In the underdoped region above T_c , the normal state of cuprates is characterized by an intriguing feature called pseudogap which results in a depletion of the electronic density of states. It was observed first in the NMR and inelastic neutron studies and was interpreted as a spin gap. Later, ARPES, heat capacity and tunneling studies showed it to be a gap in the spectrum of the quasiparticles. The exact origin of pseudogap in cuprates is not yet clear. However, in one scenario the claim is that it arises from fluctuations of preformed Cooper-pairs above T_c with no phase coherence, while in an alternative view the pseudogap is a competing correlation that takes away the spectral weight that would be otherwise available for superconductivity [39]. The pseudogap temperature specified in the phase diagram is not a sharp transition temperature but marks a gradual crossover into pseudogap region. The normal state in highly overdoped region is more like a normal metal or Fermi liquid as the resistivity in this regime follows the T^2 dependence, however the normal state above T_c in underdoped superconducting region is called strange metal or non-Fermi liquid as the resistivity in this regime follows power laws in T different than T^2 .

Superconducting properties

YBCO with a $T_c = 92\text{K}$, is a highly anisotropic material based on the anisotropic crystal structure. It belongs to the Type II class of superconductors characterized by a large ($> 2^{-1/2}$) Ginzburg-Landau parameter $\kappa = \lambda/\xi$ with λ being the magnetic penetration depth and ξ the superconducting coherence length. Type II superconductors differ from type I superconductors, because in the latter the superconductivity is lost above a critical magnetic field H_c abruptly, whereas the former exhibits a Meissner state below a lower critical field H_{c1} and above in a mixed state in which the magnetic field penetrates in the specimen in the form of flux filaments, called vortices, up to the upper critical field H_{c2} . For optimally doped YBCO the upper critical field is about 150T in the ab-plane and 40T for the c-axis direction. The superconducting gap in YBCO has a large value of about 30meV which is much higher than that of conventional BCS superconductors with typical values below 1meV. The superconducting gap in conventional superconductors has an s-wave symmetry around the Fermi surface but in the case of YBCO it has d-wave symmetry with nodes in different directions. The gap is zero in Cu-Cu direction whereas it maximizes along the Cu-O direction. The distance between two electrons of a Cooper pair is described by BCS coherence length given by $\xi \sim v_F/k_B T_c$, where v_F is the Fermi velocity and in conventional metal superconductors it is quite large, e.g. $\xi = 16000\text{\AA}$ for Aluminium. Since $T_c = 92\text{K}$ in YBCO we can expect a small coherence length, however, due to the low density of carriers in cuprates, the Fermi velocity is also very small which makes the coherence length even smaller such that $\xi_{ab} = 15\text{\AA}$ and $\xi_c = 2\text{\AA}$. [41] The extremely short coherence length poses some conceptual problem about pairing mechanism. The penetration depth λ of a superconductor, which measures the distance to which magnetic field penetrates into a superconductor, is related to the superfluid density n_s by the relation $n_s \propto 1/\lambda^2$. For YBCO the penetration depth is $\lambda_{ab} = 1500\text{\AA}$ and $\lambda_c = 6000\text{\AA}$. Due to the presence of Cu-O chains along b-axis, the coherence length is smaller compared to that along a-axis, the value λ_{ab} is calculated as $(\lambda_a \lambda_b)^{1/2}$. The large value of the penetration depth corresponds to a low superfluid density in YBCO.

The critical current density j_c is an important figure of merit for a superconductor for potential applications' point of view. The critical current for layered cuprates is very anisotropic, in case of YBCO, the value of j_c depends upon the nature of the specimen itself. For bulk single crystal specimens the j_c typically ranges from 10^{-10^3} A/cm² at 77K, the highest values are however obtained for epitaxial thin films of YBCO with $j_c \sim 10^7$ A/cm² at 77K. Lower j_c value for bulk specimens come mainly from intergrain weak links [42].

2.2 Manganites

2.2.1 Manganites in complex oxide research

The research in the field of complex oxides has been determined by the wealth of interesting properties suitable for applications including magnetic order, high temperature superconductivity (HTS), colossal magneto-resistance (CMR), metal to insulator transitions (TMI), high electronic and/or ionic conductivity. They make them candidates for several application areas such as microelectronics, spintronics, nanotechnology, energy conversion and storage (e.g. fuel cells, batteries and thermoelectrics) [43, 44]. In the past decade, the manganite oxides with the general formula $RE_{(1-x)}A_xMnO_3$ (where RE is a rare earth element e.g. Pr, La, Y; A is a divalent alkaline earth element e.g. Ba, Ca, Sr) gained special because of three main driving forces:

(i) Manganites are a subgroup of strongly-correlated electron systems, for which interaction between d-electrons is pronounced and responsible for many peculiar properties. Therefore, understanding the new physics appearing in manganites is of fundamental importance as a basic research problem. It is clear that information obtained from manganites can be transferred to other subgroups of strongly-correlated electron systems by analogy and in turn will shed more light on hot topics like high temperature superconductivity.

(ii) They exhibit the CMR phenomenon [45-47] which is a large change in the electrical conductivity of the specimen caused by the application of a magnetic field (c.f. Fig. 7).

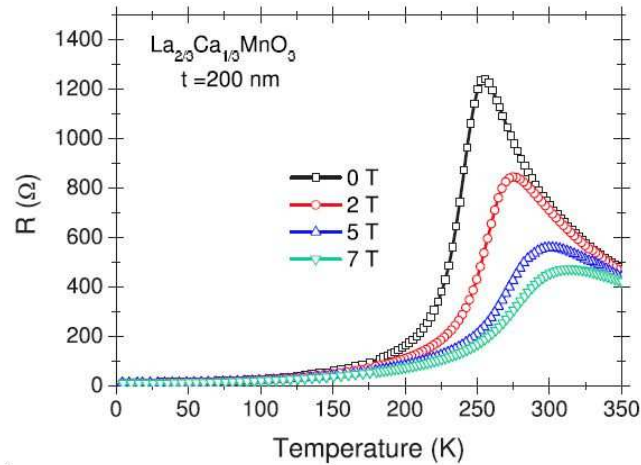


Fig. 7: Resistance vs. temperature dependence of a 200 nm thick LCMO film in different applied magnetic fields [48].

It should be noted that due to this property, they are regarded as promising candidates for switching and sensor applications [49]. One of these applications are tunnel magnetoresistance (TMR) sensors which consist of two layers of ferromagnetic materials separated by a thin tunnel barrier [50-52]. A further area gaining increasing application oriented interest is multiferroicity in thin films. Multiferroic materials are formally defined as materials showing more than one primary ferroic order parameter (ferromagnetic, ferroelectric, ferroelastic) simultaneously.. With these materials, the magnetic state can be manipulated by an electric field or vice versa. In such a device, the transport of spins through the barrier can be electrically tuned and magnetoresistance of the device can be controlled by the applied electric field.

(iii) The electrical properties of some manganites (i.e. having high electronic and ionic conductivity) satisfy the requirements as a cathode material for solid oxide fuel cells (SOFC), based on the conversion of chemical energy to electrical energy with reasonable efficiency [53, 54]. This technology is considered to be one of the most promising options for new and environmentally friendly electrical energy sources; however, the development and application of improved electrode materials requires electrochemical processes at lower operating temperature (below 900°C). For this purpose, lanthanum strontium manganite oxide (LSMO) as

a cathode material for oxide-ion SOFC has been investigated systematically by varying geometrical parameters and modifying dopant ion-type and/or concentration in the material [55-57].

2.2.2 The role of chemical composition and structure in LCMO

ABO_3 compounds (e.g. $LaMnO_3$ -LMO-, an antiferromagnetic insulator), where A and B are large and small cations, respectively, are the parent compounds for the rare earth manganites. They have a nearly cubic perovskite-like crystal structure, shown in Fig.8. This structure can be regarded as a three-dimensional network of corner sharing MnO_6 octahedra, where the Mn ions are at the center (see Fig. 8). Eight octahedra form a cube with the A site, e.g. La^{3+} or Ca^{2+} , at its center [56,57].

The properties of the perovskites are mainly determined by the band structure and band filling, but also depend on the cation ordering, presence of vacancies and dopants. In the pure LMO compound, the partial substitution of the La^{3+} site by Ca^{2+} opens the possibility of phase changes with temperature (stated in the following section) by producing charge compensation with increasing the hole densities [58-64] which are responsible of higher electrical conductivity of the manganese oxides. Nonstoichiometry and lattice defects in lanthanum manganite influence the multivalent nature of Mn.

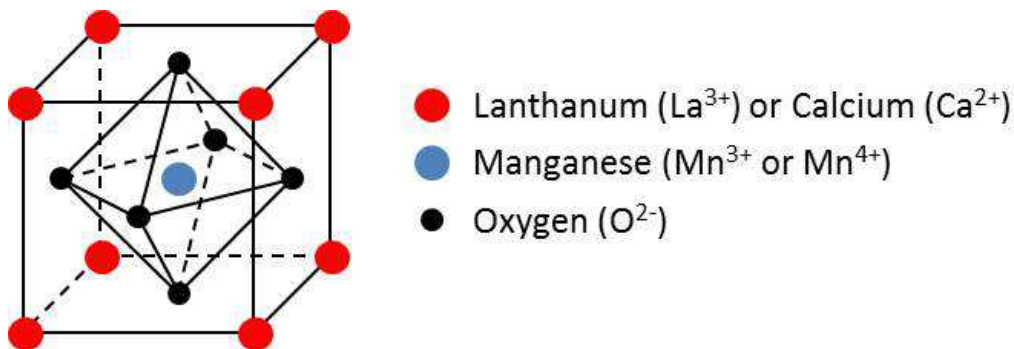


Fig. 8: The crystal structure of $LaMnO_3$ as a representative of the perovskite family.

Charge equilibrium is maintained by the oxidation of a corresponding fraction of Mn^{3+} ions to the oxidation state Mn^{4+} [62]. The oxidation state of Mn also depends on the oxygen stoichiometry in $\text{LaMnO}_{3\pm x}$ and can be enhanced by the presence of transition metal vacancies or reduced by oxygen vacancies in the lattice. Moreover, the cation-doping is strongly related with the ionic radii mismatch, which also influences the electronic structure of the material via the tolerance factor. The Goldschmidt tolerance factor, t , defined in Eq. (1), was proposed to describe the distortion and stability of any ABO_3 perovskite lattice [64].

$$t = r(A) + r(O) / \sqrt{2} [r(B) + r(O)] \quad (1)$$

The terms $r(A)$, $r(B)$ and $r(O)$ stand for the ionic radii of A, B cations and O anion, respectively. The structure is predicted to be cubic if t equals to 1. On the other hand, the distorted perovskite-like lattices exist approximately in the ranges of $0.89 < t < 1$ and $1 < t < 1.02$. For most of the manganites t is smaller than 1, i. e. the A cations are too small for a cubic lattice. As a result, a buckling of octahedra occurs, leading to orthorhombic crystal symmetry, as shown in Fig 9. Apart from structural reasons, some distortion can also have an electronic origin such as in the case of Jahn-Teller effect of Mn^{3+} cations, which will be discussed in the subsequent section of this chapter

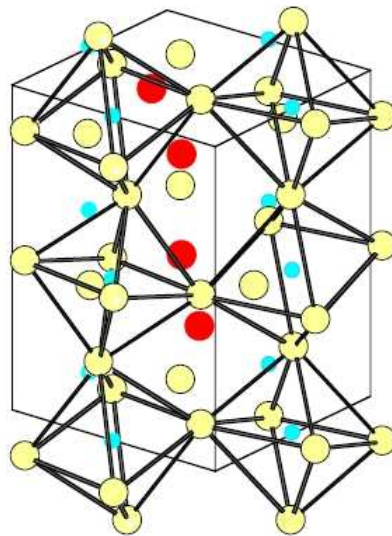


Fig. 9: The orthorhombic structure caused by distortion of the perovskite lattice [65].

2.2.3 Electronic and magnetic interactions in LCMO

The electrical and magnetic properties of manganites result from a competition between several mechanisms such as a charge, orbital and spin ordering [66, 67] superimposed by lattice effects. The phase diagram of the $\text{La}_{(1-x)}\text{Ca}_x\text{MnO}_3$ system [68] shown in Fig. 10 as an example, can be considered as a consequence of this competition.

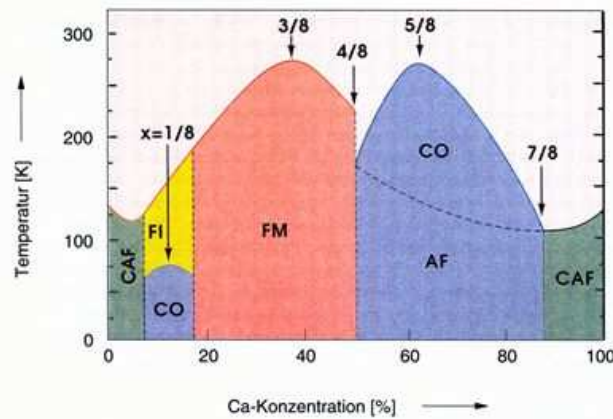


Fig.10: Phase diagram ($\text{La}_{(100-x)\%}\text{Ca}_{x\%}$)MnO FM: Ferromagnetic Metal, FI: Ferromagnetic insulator, AF: Antiferromagnetic, CAF: Canted Ferromagnetic, and CO: Charge-ordered [68]

In Fig. 10 it is seen that several different electronic phases (e.g. paramagnetic -PM-, antiferromagnetic-charge-ordered -AF-CO- and ferromagnetic -FM- phases) can exist according to the temperature and Ca^{2+} doping level of the specimen. At the boundaries of the phase diagram some of these electronic phases coexist (e.g. at 50 % Ca, there is region of high complexity due to the coexistence of three fundamental phases FM, AF-CO and PM) [69]. The equilibrium between these phases can be disturbed quite easily in favor of a certain phase by external perturbations such as magnetic field, electrical field, photon flux and strain.

Despite the ideas proposed to explain the observations such as CMR, inhomogeneous character and strong correlation between ferromagnetic metallic phase and metal-insulator transition [70 -72], most of these points could not be clarified entirely. There are still many open questions in addition to many clues obtained from both experiments and theoretical

investigations. Some of the basic ideas mentioned above are double exchange, electron phonon interaction due to Jahn-Teller distortion, mesoscopic phase separation and percolation phenomena.

The double-exchange model, proposed first by Zener [73], is crucial to explain the electron transfer in the ferromagnetic-metallic phase, demonstrated by a simple sketch in Fig. 11

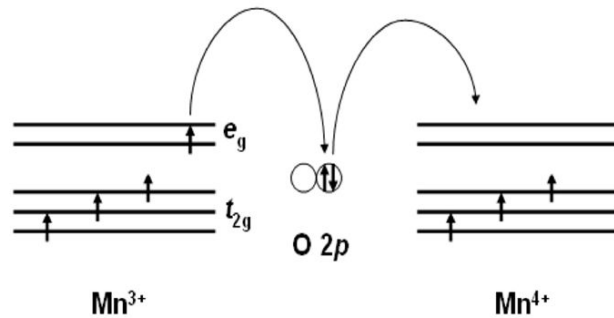


Fig. 11. Principle of the double-exchange mechanism [73].

Whereas an e_g electron of Mn^{3+} is transferred to the O 2p orbital, an electron goes from O 2p orbital to Mn^{4+} simultaneously. Due to strong Hund coupling the probability of electron transfer is larger when spins of neighboring Mn^{3+} and Mn^{4+} ions are parallel. Consequently, strong ferromagnetic interaction is ensured. In a semiclassical treatment, the double exchange mechanism leads to a dependence of the electron transfer between Mn ions on the angle Θ between their spins. Then, the effective hopping probability is proportional to $\cos(\Theta/2)$, which varies from 0 to 1 as the relative orientation of the spins of neighboring Mn ions varies from antiparallel to parallel [74]. Double exchange generally competes with the superexchange mechanism [75-77] representing the electron transfer between two Mn^{4+} ions, which favors antiferromagnetism. This rearrangement is thought to stem from strong Coulomb interaction.

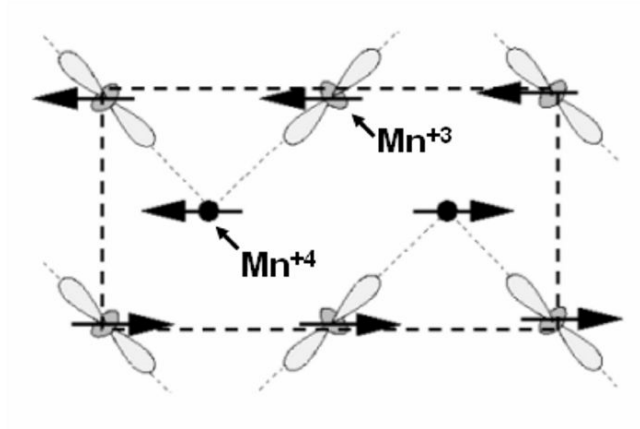


Fig. 12: Charge, spin and orbital ordering in manganites (reproduced from reference [77]).

In addition to charge ordering, there are two more degrees of freedom namely orbital and spin ordering [74]. These three mechanisms are shown in Fig. 12 in a simple sketch. For instance it is seen that a sublattice can be constructed from the ordered arrangement of d_{z^2} orbital of Mn^{3+} ions. Charge ordering leads to localization of the mobile electrons in certain positions in the lattice and reduction of the electrical conductivity whereas orbital and spin ordering give rise to anisotropic electron transfer. The Jahn-Teller effect [78] is the distortion of a non-linear molecule with a degenerate electronic state to remove the degeneracy and to reduce the overall energy. In an octahedral environment, as in the case of Mn^{3+} and Mn^{4+} ions in manganites, two e_g orbitals have larger energy than the remaining t_{2g} orbitals (see Fig. 13). A large distortion is caused by the Mn^{3+} ion since the number of electrons in the e_g orbital is odd. However, no Jahn-Teller effect is expected for the Mn^{4+} ion, which has only three electrons in the t_{2g} orbitals. Pronounced Jahn-Teller distortions are generally associated with the insulating behavior because charge carriers are trapped and electron-lattice polarons are formed in the vicinity of these local distortions. It has also been demonstrated employing several manganite systems that Jahn-Teller distortion gradually decreases as the temperature is decreased. It has the lowest value at the insulator to metal transition and stays practically constant if temperature is reduced further [79].

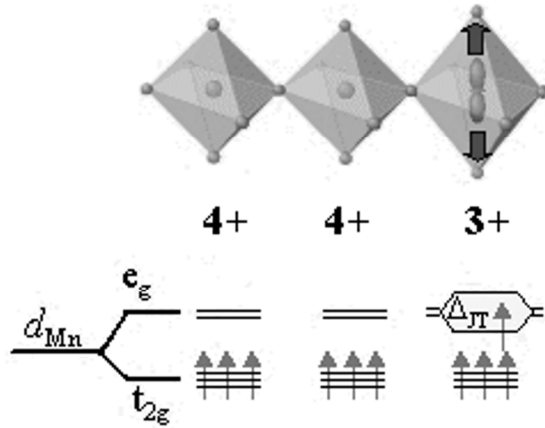


Fig. 13: Jahn-Teller distortion in manganites [77].

2.2.4 Strain effects

One of the main factors distinguishing manganite thin films from bulk ceramic specimens is their residual strain, which can be caused by epitaxial relationship between the film and the substrate, its deposition conditions and some possible temperature variations (if in-plane coefficients of thermal expansion are different for the film and the substrate). It is obvious that the above mentioned strain modifies the Mn-O-Mn bond angle and the Mn-O distances. These variations can have drastic influences on the resulting electrical and magnetic properties due to the fact that the Mn d orbitals and O p orbitals, determining these properties of the film, are strongly coupled to the lattice degree of freedom. Consequently, it is possible to use the strain parameter to deliberately tailor the properties of manganite thin films. Three basic routes can be followed to vary the residual strain in thin films: (i) Deposition conditions (e.g. energy of the atoms leaving the target, temperature of the deposition and pressure inside the chamber) can be altered. However, some other parameters such as grain size and defect concentration are also modified by this approach, making a systematic investigation tedious. (ii) Films can be grown on various substrates having different lattice constants and, in turn, applying epitaxial strains of different extent [80-84]. (iii) The strain in the film can be altered by

depositing layers with different thicknesses (e.g. see Refs. [85-91]). The thinner films are more strained than the thicker ones since a certain amount of epitaxial strain is relaxed by defects like misfit dislocations in the latter. It should be noted here that, apart from the residual strain, there are also additional factors that can influence the bond lengths and angles in the film lattice as externally applied strain (e.g. hydrostatic strain and strain imposed by a piezoelectric substrate) and several types of defects (e.g. dislocations, vacancies and self-interstitials; for the effect of O vacancies see the following section).

2.2.5 Oxygen stoichiometry effect

Oxygen stoichiometry, which can be varied by heat treatments in vacuum and different O₂ environments during preparation, has been shown to have a crucial role in determining the structural and electronic states of several oxide thin films [92-101]. The response of the oxide to the heat treatments mentioned above can be considerably different. For instance, the resistance of Sr₂FeMoO₆ films deposited on (100) SrTiO₃ (STO) substrate increases during O₂ annealing, explained by the formation of high resistance regions in grain boundaries, whereas La_{0.67}Ca_{0.33}MnO₃, in the ferromagnetic (FM) phase, deposited on (100) NdGaO₃ (NGO), becomes more metallic, probably due to the inverse relation between the hole concentration and the oxygen vacancies. The out of plane lattice parameter and resistivity of La_{0.67}Ca_{0.33}MnO₃ films increase with vacuum annealing [92]. Additionally, it was observed by Prellier [101] that oxygen annealing leads to an enhancement of T_M and T_C. It should be noted here that a great majority of the data reported for the La_(1-x)Ca_xMnO₃ system are for the composition around x=0.3 [91-95], and relatively little is known about the response of different compositions of this family to heat treatments in both vacuum and O₂ atmosphere.

2.3 YBCO-LCMO heterostructures

2.3.1 General remarks on complex oxide heterostructures and superlattices

The technological advances in the atomic-scale synthesis of complex oxide heterostructures have provided a flourishing ground to explore electronic interactions either at their interfaces or across the layers in analogy to the mechanisms giving rise to the GMR effect in magnetic multilayers. In several recent review papers Hwang et al. [13], Keimer et al. [38] and Mannhart et al. [12] highlighted the fundamental physics background emerging from the breakthroughs based on advanced oxide thin film technology. In contrast to bulk materials, different symmetry constraints can be artificially imposed at the interfaces and thus offer the opportunity to design structures exhibiting new phenomena with potentially intriguing novel properties. Arising from the experimental results of generating conducting layers between oxide band insulators [6] and the analysis of cuprate/manganite heterostructures and superlattices [18], the concept of reconstruction of the charge, spin and orbital states at interfaces at the nanometer scale turns out to be a new research topic with strong impact on fundamental physics and possible applications as well. Interface superconductivity, magneto-electric coupling, and the quantum Hall effect in oxide heterostructures are representative examples of the scientific and technological achievements in this rapidly growing field. Common to all these activities is the participation of at least one transition metal ion with the potential of occurring in different valence states.

Transition metal oxides (TMOs) are at the core of these research activities and are the ideal playground for the study of electron correlations. The transition metal s electrons are transferred to the oxygen ions, and the remaining d electrons are strongly correlated and determine the physical properties of these complex oxides including electrical transport, magnetism, optical response and thermal conductivity. These electron correlations constrain the number of electrons at a given lattice site, and induce a local entanglement of the charge, spin and orbital degrees of freedom and give rise to a variety of macroscopic phenomena like

Mott insulators, various charge, spin and orbital orderings, metal–insulator transitions, multiferroics and superconductivity. In recent years, there has been a burst of activities to manipulate these phenomena, as well as to create new ones, using oxide heterostructures. As described in detail by Hwang et al [13] the fundamental basis for understanding the physical properties of TMOs is the concept of the symmetry of the order parameter. As Landau has already stated, the essence of phase transitions is the change in symmetry. Manipulating the symmetry at a nanoscale level opens the door for artificially designed phase transitions. The interplay among the electronic degrees of freedom produces various forms of symmetry-breaking patterns of space inversion, time-reversal and gauge symmetry (associated with the change of the phase of the wave function) and is expected to lead to novel emergent phenomena triggered through the collective behavior of electrons.

An especially intriguing case is the combination of ferromagnetic (FM) and superconducting (SC) oxide layers as heterostructures and superlattices. Phenomenologically, ferromagnetic and superconducting order has been regarded to be antagonistic by nature for a long time. Ferromagnetic order consists in the parallel alignment of spins whereas for the essential ingredient of singlet superconductivity, the Cooper pairs, the coupling of electrons with antiparallel spin is mandatory. In this section some basics of the interplay of ferromagnetism and superconductivity are described followed by a compilation of relevant experiments which contributed to the boom of research activities in complex oxide interface investigations. Amongst them are the early activities to grow and analyze SC/FM c-axis oriented heterostructures and superlattices.

2.3.2 Superconductivity and ferromagnetism

The motivation for the research performed in this thesis is briefly mentioned in the section “Introduction”. It is the exploration of the electronic properties of superlattices composed of the high-temperature superconductor $\text{YBa}_2\text{Cu}_3\text{O}_{7-x}$ (YBCO) and the metallic ferromagnet $\text{La}_{2/3}\text{Ca}_{1/3}\text{MnO}_3$ (LCMO). YBCO-LCMO superlattices serve as a model system to

study the interplay between ferromagnetism and superconductivity, which is a special case of a more general topic aimed to search for novel quantum states at the interface of complex oxide layers.

These activities are a special case of the more general topic of coexistence of domains with different long-range ordering in one material with presumably homogeneous chemical composition. Whereas the field of mesoscopic phase separation has been explored only recently by detailed investigations of the balance between competing ferromagnetic and antiferromagnetic order in mixed valence perovskite manganites, the more fundamental question of coexistence of ferromagnetism and superconductivity has been addressed already by Ginzburg 1956 [102] He stated that singlet superconductivity and ferromagnetism do not coexist in homogeneous bulk materials due to the interaction of the superconductor order parameter and the vector potential of a magnetic field. After the development of the BCS theory and the discovery of Cooper pairs, the picture became clearer, that superconductivity will be destroyed by a magnetic exchange mechanism. The exchange field in a ferromagnet tends to align the spins in the same direction, thus preventing the formation of Cooper pairs with an antiparallel spin configuration. Whereas the antiferromagnetism and superconductivity can coexist quite peacefully due to the fact that exchange and orbital fields are zero on average at distances of the order of the Cooper pair size (i.e. the coherence lengths) this averaging process will not work for a ferromagnet.

There is, however, a limited class of superconducting compounds where superconductivity occurs in the presence of magnetic ions occupying a special lattice site. Some examples are found in the rare earth molybdenum selenides (RMO_6Se_8) and the rare earth rhodium borides (RRh_4B_4). All these materials have in common that the superconducting ordering temperature is substantially higher than the Curie temperature and the coexisting phase consists of a domain-like structure. A comprehensive review of the physics of the coexistence of ferromagnetism and superconductivity in these materials is given by Maple [103]. Larkin and Ovchinnikov (1964) [104] and Fulde and Ferrell (1964) [105] could show theoretically, that ferromagnetism and

superconductivity can coexist through a spatial modulation of the pair wave function in heterostructures of F and S materials, the Cooper pair wave function extends from the superconductor to the ferromagnet in a damped oscillatory behavior. These spatial oscillations of the electron density of states imply a non-monotonic dependence of the critical temperature in artificially fabricated S/F bi- and multilayers. There are, however, some cases of truly ferromagnetic superconductors such as UGe_2 and URhGe . These materials exhibit a triplet pairing character which permits the coexistence.

The discovery of ferromagnetism and superconductivity in a completely different class of materials, the cuprate based compound $\text{RuSr}_2\text{GdCu}_2\text{O}_8$ (Ru1212) [106] generated much interest in this field, mainly due to the fact that the Curie temperature is much higher ($\sim 160\text{K}$) than the superconducting T_c ($\sim 50\text{K}$), i.e. superconductivity emerges in a magnetic environment. Since in copper oxide superconductivity appears upon doping of an antiferromagnetic parent compound and $\text{RuSr}_2\text{GdCu}_2\text{O}_8$ has been identified to be a canted antiferromagnet leading to ferromagnetic component, a detailed analysis of the properties of $\text{RuSr}_2\text{GdCu}_2\text{O}_8$ can shed some light on the origin of superconductivity in the cuprates. Structurally, Ru-1212 consists of a charge reservoir block containing magnetically ordered Ru^{5+} ions intercalated by $\text{CuO}_2\text{-Gd-CuO}_2$ layers which are believed to cause superconductivity. Due to the layered structure of Ru1212 a natural extension for the research on ferromagnetic superconductors was to mimic its properties by combining oxide ferromagnets (e.g. LaCaMnO) and oxide superconductors (e.g. YBCO) in heterostructures and superlattices.

2.3.2 c-axis oriented YBCO-LCMO heterostructures and superlattices

Whereas the vast majority of the published work is confined to YBCO-LCMO heterostructures and superlattices in the (100) orientation where the ab- plane of the YBCO is parallel to the film plane, in this thesis the properties of structures in the (110) and (103) orientation is explored. The concept behind this study is the fact, that in the specimens investigated so far the c-axis with very short coherence length is pointing towards the

interfaces, whereas here, a crystallographic axis with a long coherence length is perpendicular to the film plane ((110)-structures) or is pointing at 45° to it ((103)-structures). Additionally, the atomic structure and thus the electronic structure at the interface are quite different from the (100) case, consequently quite different results can be expected. In this section the results found in (100) structures are briefly summarized.

The early explorative activities focus on the mutual influences between both materials on the electrical conductivity [18] and magnetic properties [19,20], the shifts of the superconducting transition temperature [17,19] and Curie-temperature as well. The application of advanced diagnostic techniques such as neutron reflectometry, soft and hard X-ray absorption with emphasis on X-ray linear dichroism and X-ray magnetic circular dichroism, polarized resonant X-ray reflectometry and diffraction and their combination enable a more in-depth investigation of their properties.

Applying the techniques mentioned above, several fundamental properties of the YBCO-LCMO interface could be detected:

Charge transfer across the interface with implications of the ordering temperatures T_c and T_{Curie} .

The most simplistic approach to an explanation of the reduction of T_c and T_{Curie} would be the assumption of a charge transfer from the two components. An electron transfer from the LCMO to the YBCO implies a reduction of holes in the CuO_2 plane of the YBCO and thus a reduction of T_c . Simultaneously, a reduction of a negative charge in the LCMO corresponds to an enrichment of holes and thus according to the phase diagram a shift of the $\text{Mn}^{3+}/\text{Mn}^{4+}$ ratio to the Mn^{4+} site. Indeed, the charge transfer scenario has been experimentally verified by Chakhalian [16] as well as Varela using EELS spectroscopy in a TEM using sputtered YBCO-LCMO heterostructures [107]. In Fig. 14 the principle is outlined schematically.

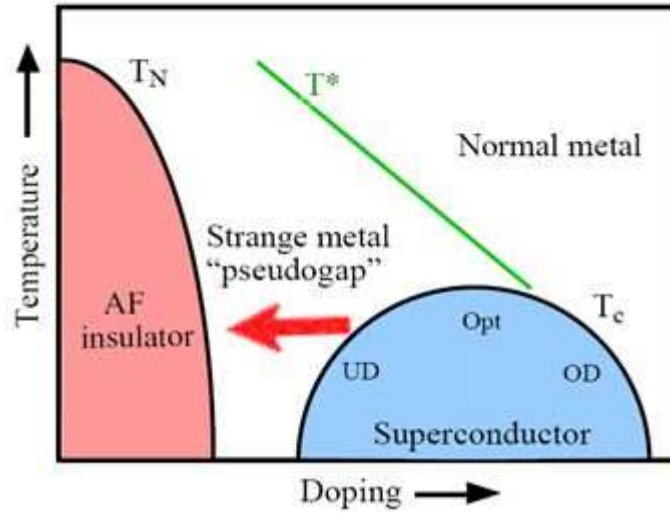


Fig. 14: sketch of the cuprate generic phase diagram with the indication of a reduction of T_c by an electron transfer from the LCMO to YBCO and thus reduction of the hole concentration and thus T_c

Interfacial orbital and magnetic reconstruction restricted to the immediate vicinity of the interface.

As an example for the success in applying different analytical tools the analysis of the magnetic structure of the YBCO-LCMO interface might be mentioned. Here, using a combination of neutron reflectometry, X-ray linear dichroism analysis (XLD), and X-ray magnetic circular dichroism (XMCD) analysis revealed a detailed microscopic element specific picture of charge transfer across oxide interfaces, the magnetization profile both, parallel and perpendicular to the superlattice plane, and offers intriguing insights into the interplay between ferromagnetism and superconductivity at the interface [108]. By its monolayer sensitivity and a penetration depth of typically several 10 nanometers, XMCD is well suited for investigations of nanoscale magnetism at “buried” interfaces. Circularly polarized soft x-rays at the L-absorption edges of Mn and Cu, respectively, have been used and the total electron yield (TEY) and fluorescence yield (FY) data were recorded simultaneously. The surface-sensitive TEY mode was used to acquire information about magnetism at the top-most interface, whereas

the FY mode allowed us to probe deeper layers. Magnetic dichroism is clearly present at both Mn and Cu edges (c.f. Fig.16). Since the manganite layers undergo a ferromagnetic transition at around 150 K, the large dichroism at the Mn edge is expected. The presence of a net ferromagnetic magnetization on Cu is surprising. The data provide clear evidence for the presence of an uncompensated induced magnetic moment in the YBCO layer in proximity to the LCMO interface. As seen in Fig. 16, the Cu dichroism is small compared to that of Mn (27 %) and does not exceed 1.4 %, indicating that only a small fraction of the volume shows the magnetic polarization on Cu. The mutual orientation of the Mn and Cu magnetic moments can be deduced from the relative sign of the L_3 peaks for the same helicity of light. Fig. 15 demonstrates that the Mn and Cu L_3 peaks have opposite signs, which indicates an antiparallel orientation of the corresponding magnetic moments. Comparing the temperature dependence of the XMCD normalized to the 4.2 K value with corresponding data for the magnetic moment it has been found that the re-scaled dichroic signal of Cu closely follows that of Mn and the bulk magnetization. The similar temperature dependence of both signals indicates that the magnetic moment on Cu is induced by strong interactions between Cu spins and the ferromagnetic moment of Mn across the interface [108].

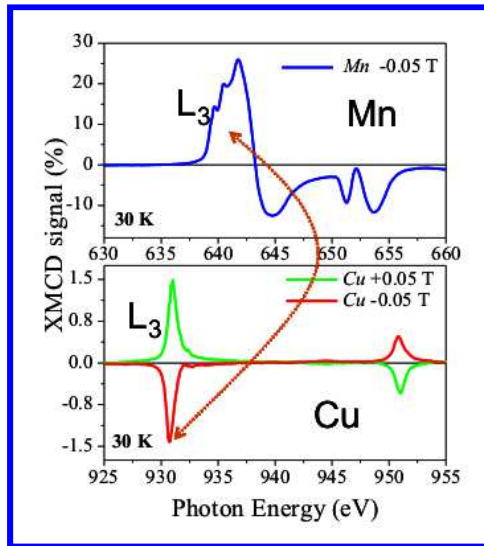


Fig. 15: XMCD signals obtained from the core level absorption spectra for Cu and Mn [108].

XLD and soft x-ray absorption spectroscopy (XAS) was also used to investigate the electronic structure and orbital occupation at the interface between YBCO and LCMO [16]. The experiments were also performed at the L-absorption edges of Mn and Cu. Fig.16 shows the x-ray absorption spectra at the Cu L_3 of the heterostructure. One can notice a shift of the interfacial absorption peak lower energy with respect to the bulk by ~ 0.4 eV. Furthermore the high-energy shoulder is no longer present. This shift is evidence of a change in valence state of Cu ions near the interface which indicates that charge is transferred across the interface. The direction of this charge-transfer is such that the hole density in YBCO is reduced at the interface. The position of the Cu L-absorption peak is independent of doping as shown in previous XAS studies on YBCO and bulk hole-doped high-temperature superconductors. Therefore the readjustment of the hole density alone cannot explain the observed shift of the L_3 absorption peak in the interface-sensitive experiment, which indicates an extreme modification of the electronic structure of the CuO_2 layer at the interface. This implies that the interfacial Cu $d_{3z^2-r^2}$ orbitals, which are fully occupied in bulk YBCO, are partially populated by holes at the interface.

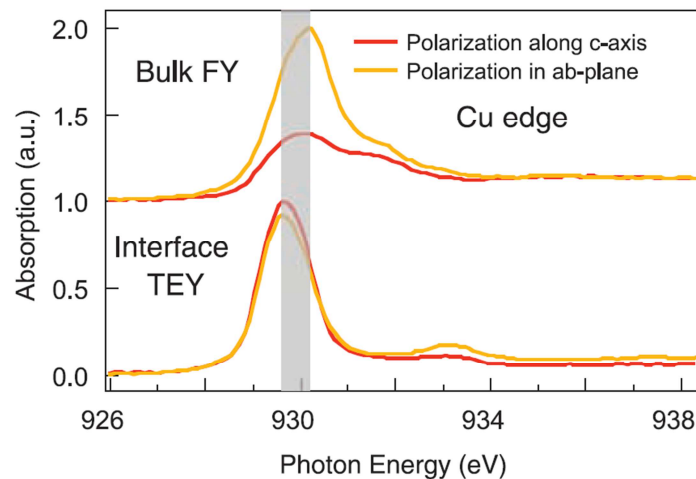


Fig. 16: x-ray absorption spectra at the Cu L_3 absorption edge, taken in bulk-sensitive (FY, top panel) and interface-sensitive (TEY, bottom panel) detection modes with varying photon polarization as indicated in the legend. a.u., arbitrary units [16].

Taking into account the in these heterostructures the Cu $d_{3z^2-r^2}$ orbital points directly toward the interface, it can hybridize effectively with the Mn $d_{3z^2-r^2}$ orbital via the apical oxygen ion generating a covalent chemical bond bridging the interface and forming an extended “molecular orbitals” consisting of atomic Cu and Mn $d_{3z^2-r^2}$ orbitals with an admixture of the P_z orbitals on the apical oxygen.

These results suggest that the orbital rearrangement and strong hybridization are at least partially responsible for the unusual magnetic behavior previously observed at cuprate manganese interfaces [16].

Hybridization of YBCO and LCMO phonon modes persisting over length scales of tens of nanometers.

Whereas the magnetic interactions as shown before, gave indications of long-range mechanisms playing a role in the interpretation of the properties YBCO-LCMO heterostructures and superlattices, dedicated Raman spectroscopy investigations give a further insight in the electron–phonon interaction occurring in this system. Since the non-local nature of the interactions between valence electrons and lattice ions is frequently associated with a multitude of vibrational modes, Raman scattering appears to be an excellent tool to study the lattice dynamics and electron-phonon interactions of YBCO-LCMO heterostructures and superlattices. Driza et al. [109] investigated the temperature dependence of Raman modes (peak positions as well as line-shape analysis) and found superconductivity induced anomalies of LCMO phonons scaling linearly with the YBCO layer thickness over a remarkably long range of several tens of nanometers. The transfer of the electron–phonon coupling between superlattice layers is interpreted as a consequence of long-range Coulomb forces in conjunction with an orbital reconstruction at the interface.

CHAPTER 3

Experimental techniques

3.1 PLD technique – general description

Apart from the more conventional deposition techniques such as sputtering or (thermal as well as electron-beam) multi-source evaporation, pulsed laser deposition (PLD) is one of the most convenient and unique methods to produce epitaxial multi-component oxide thin films with very low defect density. The historical development of the PLD technique starts in 1963 when Ready and White used a ruby laser to vaporize a solid surface [110,111], thereafter, Smith and Turner [112,113] suggested using this effect as a thin film deposition technique. In 1987, Dijkamp and Venkatesan [114] fabricated thin films of high quality of the newly discovered high temperature superconductor $\text{YBa}_2\text{Cu}_3\text{O}_7$ employing PLD. Their success initiated an avalanche of activities in complex oxide thin film research and lifted PLD from an exotic niche-type method towards a mainstream technology. With the increase of the number of research groups working in this field and the development of a new generation of excimer lasers – especially with respect to beam stability and beam homogeneity - PLD became an indispensable tool for the growth of thin films of complex oxides in the 1990's.

Exposing a solid target to a pulsed laser beam in the PLD process, a dynamic plasma is created and the material ejected from the target condenses on a heated substrate located face to face a few centimeters apart. The fast and strong heating of the target surface by the intense laser beam - typically up to temperatures of more than 5000K within a few ns - (corresponding to a heating rate of about 10^{12} K/s) ensures that all target components irrespective of their partial binding energies and individual vapor pressures at a given temperature evaporate at the same time. When the ablation rate is sufficiently high (which normally is the case at a laser fluency well above the ablation threshold), a so-called Knudsen layer is formed and further

heated (for instance by Inverse Bremsstrahlung) generating a high-temperature plasma, which then adiabatically expands in a direction perpendicular to the target surface. Therefore, during PLD, the material transfer between target and substrate occurs in a material package where the separation of the species is negligible. This holds for pulse durations smaller than μs , a criterion always fulfilled by typical excimer lasers. This process ensures the conservation of the chemical composition of the evaporation source and the film well in contrast to conventional evaporation techniques applying multicomponent sources where due to the different vapor pressures of the constituents at a given source temperature the film composition differs substantially from that of the source.

The working principle of PLD seems to be simple and straightforward but its application and precise stoichiometry control are rather complex due to the large number of variables affecting the ablation and film forming process. The distance between target and substrate, residual gas atmosphere, wavelength of the excimer laser, laser fluency, pulse frequency, substrate temperature and post deposition annealing time are some of the important parameters to be optimized in order to produce high-quality thin films. In addition to the ability of producing a film with the same composition as the target, the PLD technique provides the flexibility of using various deposition atmospheres (e.g. inert and/or reactive gases and at different gas pressures). Moreover, it is cost effective (since many vacuum systems can easily be combined with a laser), fast (e.g. deposition rates are typically $\sim 100 \text{ \AA}/\text{min.}$), clean and the thickness can be controlled in real time by counting the number of pulses. However, as a disadvantage, only samples having a limited surface area can be prepared by this method since the cross section of the ablation plume is normally a few cm^2 only due to the small laser spot size at the target site and the highly directional laser plume. As in-situ growth characterization technique, reflection high-energy electron diffraction (RHEED) is well established. This technique enables the control of the film thickness down to one unit cell by monitoring the electron reflectivity of the growing film as a function of the deposition time and counting their maxima and minima. In addition structural details can be revealed by analyzing the stripes and/or spots of the diffracted beam. In contrast to RHEED, optical in-situ methods like

spectroscopic ellipsometry are much less used, they require a special design of the growth chamber and their results are difficult to interpret.

The main components and working principle of the PLD system used in the present study are described in Fig. 17.

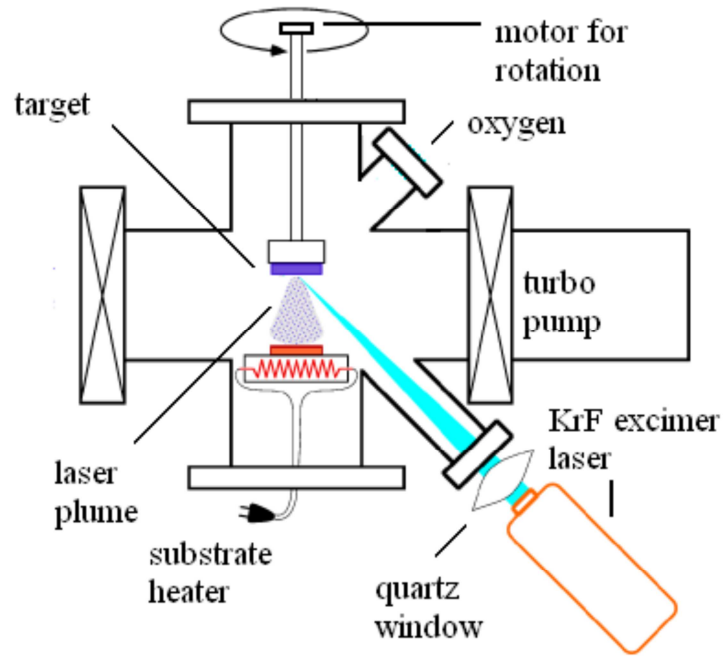


Fig. 17: Scheme of a High Vacuum Pulsed Laser Deposition System.

The laser beam is directed into the vacuum chamber via an UV- transparent quartz window and is focused on the rotating target, a pellet with a typical diameter of 15 mm. The angle between the laser beam and the target surface is adjusted to 45° . Each laser pulse produces a superheated sheath whose thickness corresponds to the penetration depth of the photons. The surface of the target material vaporizes and the atoms ejected from the target are condensed on the surface of the substrate (the distance between the target and the substrate is 4 cm) with the required structure and composition.

3.2 Essentials of thin film nucleation and growth

Film growth and thin film morphology is determined by the thermodynamics and kinetics as a result of the superposition of many individual processes such as adsorption, desorption, diffusion, nucleation and coarsening (see Fig. 18).

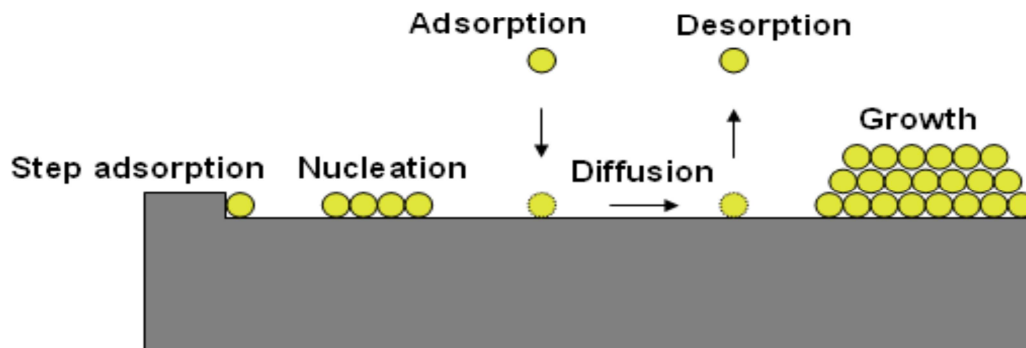


Fig. 18: Schematic representation of atomic processes during film growth.

The energy of the impinging atoms, their surface mobility, deposition rate and atomic structure of the substrate surface (e.g. terraces on the substrate surface may act as additional nucleation sites) are some of the fundamental parameters controlling the above mentioned mechanisms. Deposition starts with the condensation of a sufficient number of vapor atoms and creation of stable nuclei on the substrate. The following stage is the formation of small clusters or islands, distributed more or less homogeneously on the surface of the substrate. Thereafter, the islands grow in size and merge together which is called the coalescence step. Coalescence continues until a connected network with vacant channels is developed. Lastly, a continuous film is formed after the porous channels and, even, the isolated voids are filled in completely [115]. As shown in Fig.19, there are three main modes [116] for growth of thin films on planar substrates:

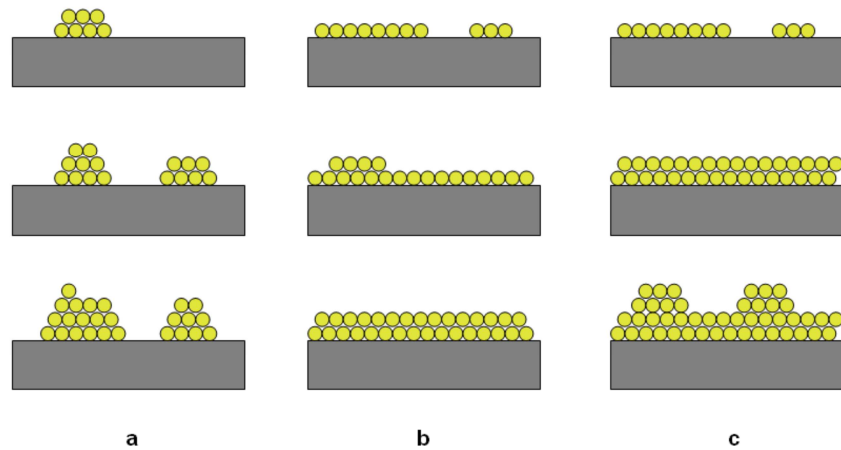


Fig. 19: Schematic representation of the three crystal growth modes: (a) island or Volmer-Weber, (b) layer or Frank-van der Merwe, (c) layer plus island or Stranski-Krastanov.

- (i) The Volmer-Weber (or island growth) mode, where clusters grow to form islands because of the stronger binding between the depositing atoms than the interaction between the depositing and the substrate atoms.
- (ii) The Frank-van der Merwe (or layer-by-layer growth) mode has the opposite characteristics of island growth mode (i.e. the strength of the binding between the adatoms and the substrate atoms is stronger).
- (iii) The Stranski-Krastanov (SK) growth mode where islands become favorable after forming layers of a certain thickness. Although, the reason behind the change from layer growth to three-dimensional growth is not completely clear, it is thought that the transition to island growth mode may be favorable as a relaxation mechanism for the strain energy created by film-substrate lattice mismatch. It should be noted here that in addition to these main three growth modes, a fourth one has been proposed, called the step-flow growth, where the film pursues step-terrace structures on the substrate. In addition to the atomic steps on the substrate other conditions such as high temperature and high deposition rate should also be satisfied to suppress the island growth and make

the step-flow mode active. However, this growth mode usually transforms to the three-dimensional growth mode for the thicker films.

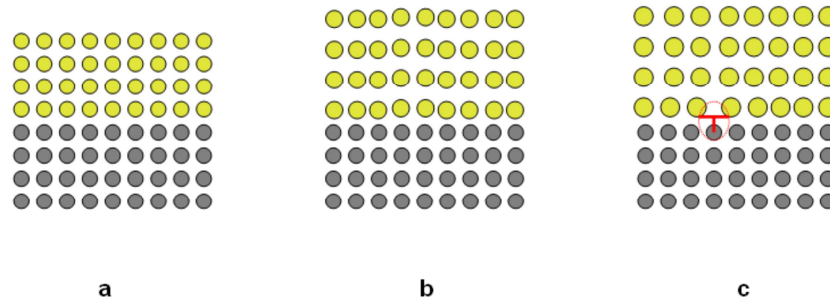


Fig. 20: Schematic illustration of (a) lattice-matched, (b) strained and (c) partially-relaxed epitaxial layers (the misfit dislocation in the partially-relaxed case is shown by a red circle).

If the orientation of the film is strictly defined by a certain relationship with the orientation of a single-crystal substrate, the film is called epitaxial. In this case, the crystal structure of the substrate provides a template for the formation of the film lattice (or in other words the structure of the film imitates the structure of the substrate material) and certain planes and directions in the film correspond to their counterparts of the substrate lattice. Small deviations of the lattice parameters of film and substrate cause up to a critical film thickness homogeneously strained films, a larger mismatch (typically $> 1\%$) generates misfit dislocations to accommodate the strain. In Fig. 20 these cases are depicted, schematically. The choice of substrates for thin films is of fundamental importance. One of the first issues that must be dealt with in determining the suitability of a substrate for thin film is the chemical compatibility of the two materials. The next issue of concern in the selection of substrates for thin films is thermal expansion match as a decent thermal expansion match between thin film and substrate is essential to provide adequate film adhesion and to avoid film cracking during thermal cycling. The substrates used should satisfy several critical conditions in order to be suitable for epitaxial growth.

- (i) It should be single crystalline and stable, chemically and mechanically similar in the range between the deposition and working temperatures.

- (ii) The in-plane lattice mismatch between the film and the substrate should be small – typically < 1%.
- (iii) The coefficients of thermal expansion of the layer and the substrate should be similar in the range between the deposition and working temperatures.
- (iv) It should have no structural phase transition in the range between the deposition and working temperatures.

The growth process of the films starts typically by the formation of a 2D nucleus with radius, r , and an edge free energy, γ , and is governed by the Gibbs free energy

$$G(r) = -\Delta\mu\pi r^2 h + 2\pi r\gamma h \quad (2)$$

with $\Delta\mu$ being the excess chemical potential and h the height of the nucleus. For the formation of a heteroepitaxial nucleus a surface energy term for the interface has to be added. The nucleation and growth mode is governed by the relative supersaturation, p/p_{eq} - with p being the vapor pressure and p_{eq} the equilibrium vapor pressure at a certain temperature - as driving force for the film growth related to the excess chemical potential $\Delta\mu$ by

$$\Delta\mu = k_B T_s \ln(p/p_{eq}) \quad (3)$$

The supersaturation has a strong influence on the growth mode of the films - either dislocation-controlled spiral growth (small supersaturation) or two-dimensional nucleation [island formation] up to a critical supersaturation $(p/p_{eq})^*$. Further increase of (p/p_{eq}) causes a transition to unstable growth, uncontrolled nucleation of growth centers on top of each other lead to a dendritic growth type [117].

The relevant quantity determining the growth kinetics and the surface morphology of the films is the normalized bonding energy, $E_b^{(i)}$, for the different species, i ,

$$E_b^{(i)} = 4\Phi_{ss}^{(i)} / 2k_B T_s \quad (4)$$

($\Phi_{ss}^{(i)}$ denotes the potential energy of a solid-solid nearest neighbor pair of atoms in the substrate unit cell). It is obvious that increasing deposition temperature implies a smaller E_b causing a higher density of kink sites on the surface and a more rapid growth. For the spontaneous nucleation of a unit cell a critical volume of the deposited material is necessary. Since atoms are impinging the substrate, diffusion is required to ensure that a nucleus has the appropriate constituents of the complex material to grow. The surface mobility of the particles impinging the substrate surface is one of the most important growth parameters. The adatom mean diffusion length, λ , is given by $\lambda = (D_s \tau)^{1/2}$ where D_s is the surface diffusion constant and τ the surface residence time. The diffusion coefficients for the different cations, however, can differ drastically; for YBCO e.g. they vary by 4 orders of magnitude from Y (10^{-13} m²/s) to Cu (10^{-9} m²/s) at a deposition temperature, T_s , of 800°C. Consequently, the formation of nanoprecipitates and compositional phase separation is facilitated [118,119].

3. 3 Optimized growth process for YBCO-LCMO heterostructures

In this work, YBCO and/or LCMO single layers and heterostructures were grown on (110) oriented strontium titanium oxide (STO) substrates. STO substrates provide small lattice mismatch with YBCO and LCMO ($\sim <0.5\%$). Also STO has a compatible thermal expansion coefficient with film materials. STO has a cubic structure with lattice constant of 3.905 \AA which is slightly larger than the lattice constants of LCMO and YBCO unit cells thus applying a small tensile strain on the grown films. Fig. 21 shows the unit cell of LCMO with the corresponding lattice parameters. LCMO unit cell can be reduced from the orthorhombic to pseudocubic representation where every orthorhombic unit cell consists of two cubes with lattice constant of 3.87 \AA . When considering the cubic unit cell of LCMO, the diffraction planes of the orthorhombic representation should be transferred to the cubic one. For example, the plane (010) in the orthorhombic representation becomes (110) plane in the cubic one. In this work we will consider the cubic structure of LCMO unless it is reported otherwise.

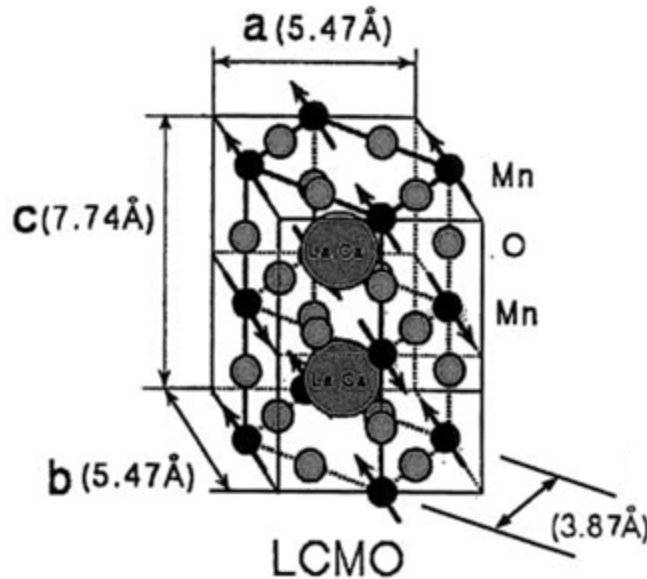


Fig. 21: Unit cell of $\text{La}_{2/3}\text{Ca}_{1/3}\text{MnO}_3$ with cubic and orthorhombic representations [57]

Following the recipe applied by Habermeier et al [120], the growth process has been optimized to produce 100% (110) oriented YBCO thin films with good superconducting properties. First

STO substrates were washed with acetone in ultrasonic bath. Substrates are then introduced to the deposition chamber where an atmosphere of 0.4 mbar Oxygen is established they are then radiatively heated. A FIR pyrometer is used to calibrate the exact temperature at the substrate surface. During deposition, substrate temperature is controlled using a computer program to account for the change in the emission coefficient so that the temperature stays constant at the growth front. The distance between the target and substrate is 40 mm. the optimum laser energy density at the surface of the target is 1.6 J/cm^2 . Before deposition of each layer the target is cleaned with a few hundred laser pulses while the shutter is closed. At substrate temperature $T_s=650 \text{ }^\circ\text{C}$ a template layer of $\text{PrBa}_2\text{Cu}_3\text{O}_7$ (PBCO) with thickness of 500\AA is deposited. The growth rate of the material is calculated by calibration runs and is controlled by pulse frequency. PBCO and YBCO is deposited at pulse frequency of 2Hz which correspond to a growth rate of about 0.62 \AA /sec . this step is very important to insure that the YBCO layer grows purely in (110) orientation without any contribution of (103) orientation. Without it the film will grow in a mixed phase of a minority (110)-oriented and majority (103)-oriented grains. After depositing the template layer, the substrate is heated up to the optimum growth temperature of YBCO which is $720 \text{ }^\circ\text{C}$. At this temperature, the desired YBCO layer is deposited at pulse frequency of 2 Hz which also corresponds to a growth rate of about 0.62 \AA /sec . This slow rate insures a relatively smoother surface while depositing at growth rate higher than 1 \AA /sec produces a very rough surface with column-like spikes on the surface. For heterostructures, LCMO layer is deposited at $720 \text{ }^\circ\text{C}$ directly after the YBCO layer with the same laser energy (1.6 J/cm^2) and at pulse frequency of 3 Hz which corresponds to a growth rate of about 0.4 \AA /sec . once the deposition is finished, the sample is cooled down to $530 \text{ }^\circ\text{C}$ at $20 \text{ }^\circ\text{C/min}$. The film is then in-situ annealed in 1atm oxygen for 1 hour to ensure complete and homogeneous oxygenation throughout the sample. Fig. 20 shows the temperature program for depositing and annealing process [121].

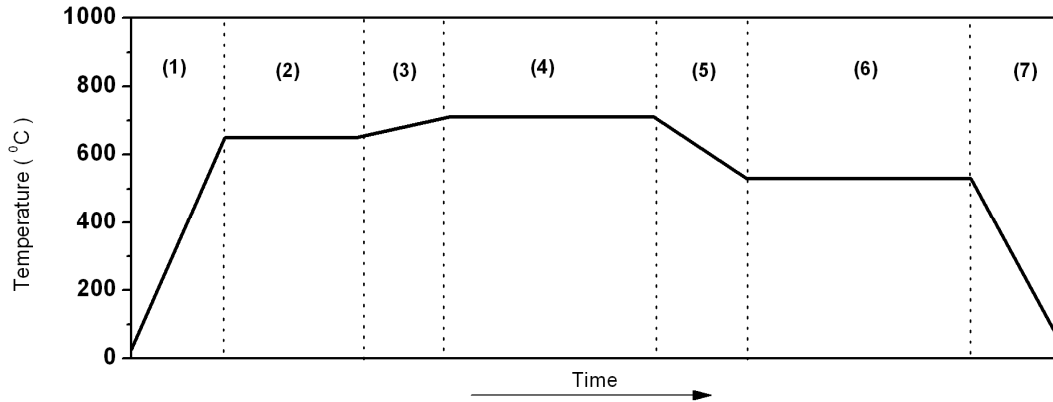


Fig. 22: Temperature program for thin film deposition.

- (1) Heating the substrate to 650 °C.
- (2) Depositing 500 Å of PBCO at 650 °C in 0.4 mbar oxygen partial pressure.
- (3) Heating the substrate to 720 °C..
- (4) Depositing YBCO layer at 720 °C in 0.4 mbar oxygen partial pressure (in heterostructures the LCMO layer is deposited directly after the YBCO layer at the same temperature and oxygen partial pressure).
- (5) Cooling down to 530 °C for annealing step.
- (6) Annealing the film at 530 °C in 1 bar oxygen pressure for 1 hour.
- (7) Cooling down to room temperature.

3. 4 Thin Film characterization techniques

3.4.1 Structural and microscopic analysis

X-ray diffraction

The determination of phase purity and the epitaxial relationship between the film and the substrate and phase analysis were carried out by X-ray diffraction (XRD). The 2Θ - ω (where 2Θ is the angle between the incident and the diffracted X-ray beams and ω is the angle between the incident X-ray beam and the sample surface, (see Fig. 23) scans between 10° and 120° , the rocking curves (or so-called ω scans) [99], reciprocal space mapping (RSM; i.e. combination of several rocking curves at different diffraction angles, $2q$ for the basic features of RSMs of epitaxial thin films) and scans between 0° and 360° were performed using a fourcircle Bruker D8 Discover diffractometer, equipped with a Cu X-ray tube, Göbel mirror, 4- bounce 022 Ge channel-cut monochromator (to select only the Cu $K_{\alpha 1}$ radiation), Eulerian cradle and a scintillation counter. The pole figures of the specimens were measured using Cu K_{α} radiation in a Philips X'Pert MRD diffractometer equipped with an Eulerian cradle and operating in parallel beam geometry. For calculating the lattice parameters accurately, position of the substrate peak was employed as internal reference. Afterwards, lattice spacings were plotted against the Nelson-Riley function from the intercept of the linear fit applied to the data. This method is widely used to eliminate instrumental errors as well as errors from absorption in the specimen and sample displacement.

3.4.2 Magnetometry

The temperature dependence of magnetization was investigated by a Quantum Design Magnetic Property Measurement System (MPMS) and a Quantum Design Vibrating SQUID (superconducting quantum interference device) Magnetometer (VSM). It consists of superconducting magnetic shield and superconducting pickup coils in the vacuum flask. The working principle is the measurement of the flux change through a pick-up coil system (c.f. Fig.24).

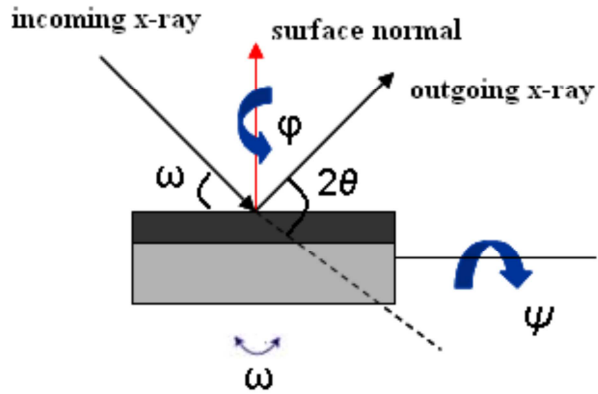


Fig. 23: A systematic view of different angles in the XRD.

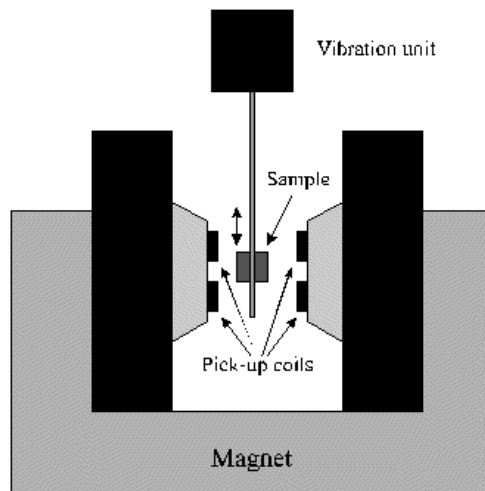


Fig.24: Schematic sketch of a VSM-type Magnetometer

Whereas in the conventional VSM's of the Foner-type the signal is picked-up by dedicated coil assemblies, in the recently developed SQUID-VSM (Quantum Design) the pick-up coils have been replaced by a SQUID assembly, thus ensuring an increase of the sensitivity by a factor of 10^4 . The magnetic field (0.01 and 1 T) was oriented parallel and perpendicular to the film

surface during field cooling (FC) and zero field cooling (ZFC). During ZFC, samples first were cooled to 5 K then field was applied to sample. Afterwards, the magnetization was measured in the heating process up to 300 K. During FC, samples were cooled from 300 K down to 5 K in the same field. It is noted that magnetization measurements were also performed for substrates without film, because the data can be subtracted from the results obtained for particularly thinner films in order to eliminate the possible contribution –at high applied magnetic field- to the magnetization from the substrate (diamagnetic character), the holder and the glue employed to fix the specimens.

3.4.3 Transport measurement

Resistivities of the films were measured within the temperature range between 5 K and 300 K by four-point probe method. A constant DC current (varied between 10^{-7} and 10^{-4} A) is passed through the two outer leads while the potential drop across the sample was measured from the two inner leads. Evaporated chromium/gold pads (20 nm/200 nm) were prepared by photolithography in Technology Service Group, Max Planck Institute, described in Fig. 25.

First, a layer of photoresist with a constant thickness of about 0.1 – 0.2 μm was applied on top of the film by spin coating. Before and after spin coating, samples were annealed at around 100°C for removing any traces of contamination on the surface and hardening the resist, respectively. In the next step, after the mask alignment, the light-sensitive resist was illuminated through a photomask with UV light. The photoresist was then developed using an appropriate alkaline solvent, removing those parts of the resisting material that were previously exposed to UV light. Finally, samples were post-annealed to improve adhesion and if it is necessary, any residue of the resist was carefully removed with Ar plasma. While preparing the contact, silver epoxy were used to attach the gold wires having a diameter of $\sim 20 \mu\text{m}$ to the film surface, as shown in Fig. 26.

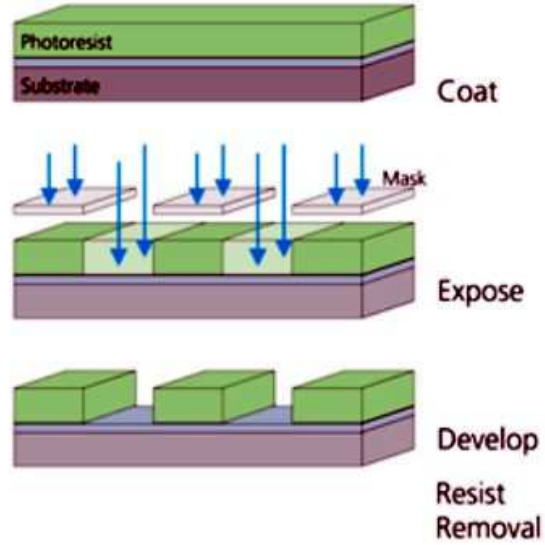


Fig. 25: Main steps of the photolithography process

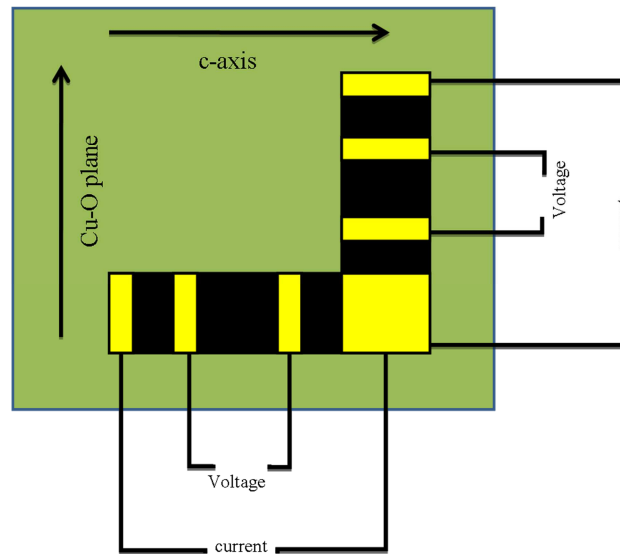


Fig. 26: The sample geometry for four-point probe measurement.

The current source was a programmable Keithley–220 and the voltage was recorded by an HP-8440 Voltmeter. Afterwards, the resistivity values were determined from the measured resistance, R , and the parameters related to the sample and the measurement geometry such

as the film thickness, t , the mask length, w , and the distance between the voltage contacts, l , according to the relation

$$\rho = Rtw/l \quad (5).$$

The effect of a magnetic field on the resistivity of the samples on various substrates was investigated employing a Quantum Design Physical Property Measurement System (PPMS) applying magnetic fields of 0.01, 1, 4, 7 T with the same measurement geometry explained above.

3.3.5 Raman spectroscopy

Raman scattering, , has been demonstrated to be a powerful experimental tool yielding a wealth of information about solid state materials. In a Raman scattering experiment, light of a known frequency and polarization is scattered from the specimen. The frequency of the inelastically scattered light is shifted up or down due to vibrational, rotational and other low frequency transitions specific to the sample under investigation. For the purpose of this thesis Raman scattering is used to analyze the oxygen stoichiometry of YBCO, which can be inferred from the frequency of Raman active phonons and it is also used to investigate the orientation of the grown films taking advantage of the anisotropy of the phonon signal depending on the angle between crystallographic axis and the polarization of incident light. As outlined by Thomsen [122] the following background information is essential for the purposes of thin film analysis: The scattered electric field (E_s) is related to the incident electric field (E_L) via the Raman tensor R . The experimentally determined Raman intensity I is given by

$$I \sim |\vec{E}_s \cdot \vec{R} \cdot \vec{E}_L|^2 \quad (6)$$

As an example we consider the Raman-active phonons in YBCO. The unit cell of YBCO contains 13 atoms. This gives rise to 39 vibrational modes, 36 of them are optical and the other 3 are acoustical modes. Optical modes could be Raman allowed, IR allowed or silent modes (silent

modes means that they are neither Raman-active nor IR-active). There are three different types of Raman modes for YBCO. One is the A_g mode which corresponds to axial motion along the c-axis. The other two modes, known as B_{2g} and B_{3g} , represent transverse motions along the a and b axes and are about two orders of magnitude weaker than the A_g mode. Fig. 27 shows the five A_g allowed phonon modes from xx/yy polarized Raman scattering of optimally doped $\text{YBa}_2\text{Cu}_3\text{O}_{6+\delta}$ single crystal at 100 K with the corresponding vibrations.

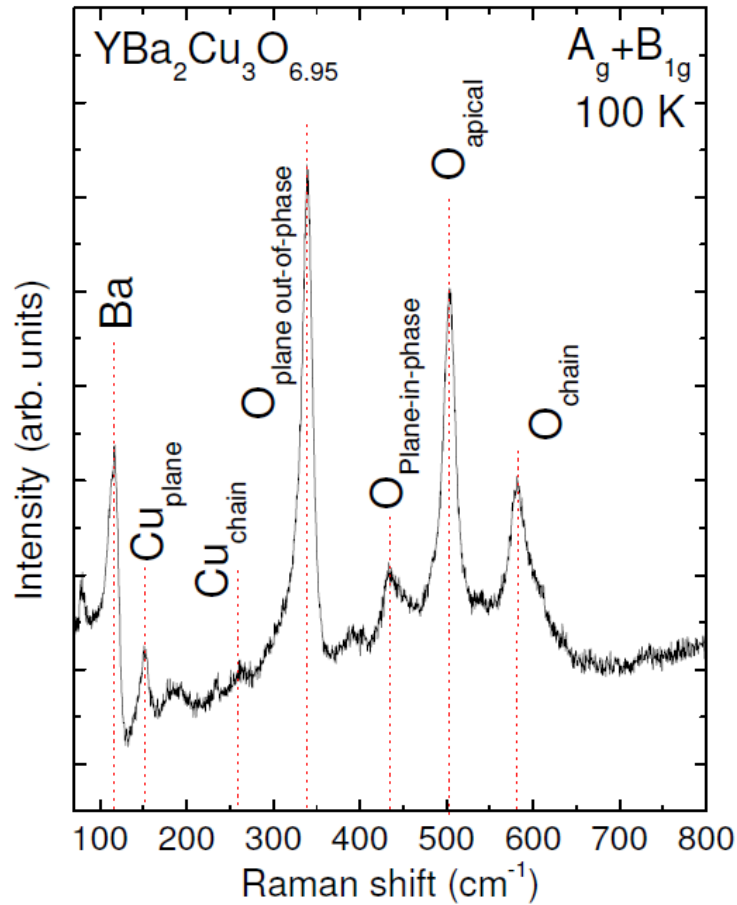


Fig. 27: xx/yy Raman spectrum of YBCO single crystal showing the A_g allowed phonon modes [123].

The 340 cm^{-1} mode have B_{1g} symmetry in the tetragonal structure of YBCO. It should be transferred to A_g symmetry in the orthorhombic structure. But in fact it still has B_{1g} symmetry in orthorhombic structure, since the deviation from B_{1g} vibration is very small. Polarization

configuration of incident and scattered light plays an important role in observation of Raman spectrum. Accordingly, Raman spectroscopy can be a powerful tool to investigate crystal orientation by studying relative phonon intensities with different configurations. Studying phonons which correspond to oxygen atoms can give a reliable estimation for oxygen content in the crystal as will be shown later.

CHAPTER 4

Results and discussions

GENERAL REMARKS

As described in the introduction the main intention of this thesis is the investigation of the physics of electronic interactions occurring in YBCO-LCMO ferromagnet-superconductor bilayer and trilayer systems where the long superconductor coherence length, ξ_{ab} , is pointing perpendicular to the film plane. If the technological hurdles are overcome, a detailed investigation of the anisotropy of the interaction between ferromagnetic LCMO and superconducting YBCO can be achieved, complementary to the well studied case when ξ_c is directed perpendicular to the film plane occurring in c- axis oriented heterostructures and superlattices. The chapter is organized as follows: First, the properties of (110)- oriented single layer YBCO and LCMO are described, then the case of (110)-oriented YBCO-LCMO bilayers is treated, followed by the analysis of (103)- oriented trilayer FSF structures and finally, the properties of (110) SFS structures with ultrathin magnetic layers embedded in between superconducting films are described.

4.1 (110)-oriented YBCO and LCMO thin films

4.1.1 (110)-oriented YBCO thin films

The experimental details of the preparation of (110)-oriented YBCO thin films are already described in Chapter 3, here, the results are presented and discussed.

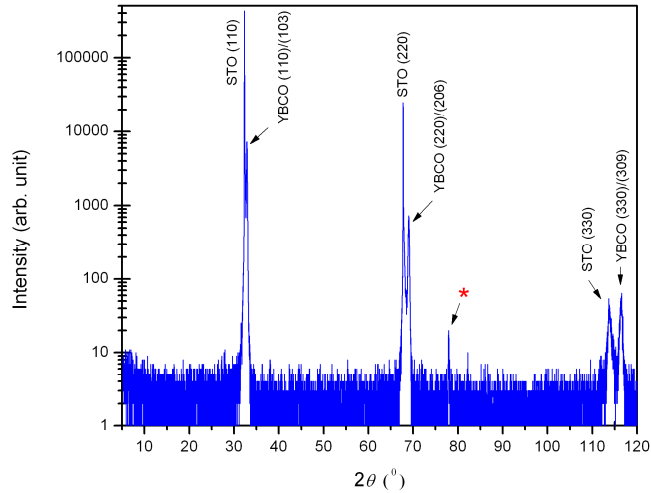


Fig. 28: Representative 2θ - ω scan of a 1000Å YBCO thin film deposited on a (110) STO substrate.

X-ray diffraction (XRD) was used to investigate the structural properties of the specimens, including the determination of the epitaxial relationship between the film and the substrate and the phase analysis. All measurements were carried at ambient temperature. 2θ - ω scan was performed using a four-circle Bruker D8 Discover diffractometer. Fig. 28 shows the diffraction pattern of a 1000 Å thick YBCO film. The observed peaks refer to (110) for STO and (110)/(103) for YBCO only, indicating the absence of phases with other orientations. The peak at $2\theta=78^\circ$ (star sign) is originated from the sample holder which was also observed in the absence of any sample. For these films, conventional 2θ - ω scans are not sufficient to distinguish between the two orientations of the YBCO thin film [(110) or (103)] since these diffraction peaks occur at the same value of 2θ . The two orientations possible are depicted in Fig 4a and 4b in the introduction. The mosaicity of the sample as measured at the (110) position is $0.18\pm 0.01^\circ$ in 2θ [full width at half maximum (FWHM)], which indicates a high-quality crystalline structure.

Diffraction plane	(110)	(103)	(220)	(206)	(330)	(309)
d-spacing (Å)	2.7262	2.7262	1.3613	1.3631	0.9052	0.9073

Table x shows the d-spacing for both (110) and (103) STO (110) substrate.

Pole figure measurements were carried out in order to distinguish between (110) and (103) orientations using Co K α radiation in a Philips X'Pert MRD diffractometer equipped with an Eulerian cradle and operating in parallel beam geometry. The reflection from (117) planes of YBCO was selected for the pole figure measurements since it does not overlap with any of the LCMO reflections (for heterostructures) and does only slightly overlap with the (220) reflection of the substrate.

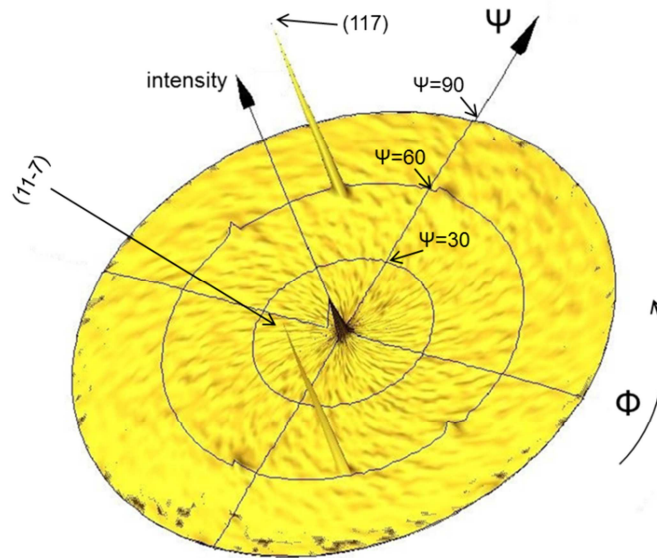


Fig. 29: (117) Pole figure of a 1000 Å (110)-oriented YBCO thin film.

Fig. 29 shows the (117) pole figure of a 1000 Å thick YBCO film. The two peaks at $\psi = 58^\circ$ are consistent with the theoretical values for a (110) oriented YBCO film. If the film would be (103) oriented, four peaks should appear at $\psi = 30^\circ$ and four other peaks at $\psi = 72^\circ$. At $\psi = 60^\circ$ four small peaks are observed which correspond to the strong (220) reflection as the (220) reflection of the STO (110) substrate is located in the vicinity of the (117) reflection of YBCO. The four peaks at $\psi = 30^\circ$ which refer to a (103)-oriented film were not observed. The above mentioned features in the pole figure of the specimen suggest that the YBCO layer is epitaxially grown on (110) STO substrates with no contribution of the (103) orientation. (110) oriented film means that a and b axes of the YBCO unit cell are 45° tilted to the substrate surface whereas the c-axis of the YBCO is oriented parallel to substrate surface.

Raman scattering can also be used to determine the crystal orientation for YBCO films where the Raman spectra of the film are recorded with two perpendicular polarizations of the laser beam, taking advantage of the anisotropy of the signal from YBCO phonons depending on the polarization of incoming light. Additionally, Raman scattering is also helpful to determine the oxygen concentration of YBCO since the position of the oxygen phonons depend on the level of oxygenation of the film, especially pronounced for the apical oxygen. Although Raman scattering is very helpful, however, it remains a local measurement since the probed area is not more than few hundreds of squared micrometers so to get an overall idea of the crystal orientation YBCO film, Raman spectra should be taken on different places of the film. One should also mention that this method is not suited for films with thickness less than 1000 Å, unless the confocal technique is applied.

Fig. 30 shows an example of Raman spectra of a YBCO (110) thin film recorded at room temperature. Raman spectra were taken using green light laser ($\lambda = 514.532$ nm) with two perpendicular polarizations. The phonon intensity in zz configuration is much higher than the other configuration (notice different scales to left and right). These data agree with the experimental results for a twin free YBCO single crystal [124] (shown in Fig. 31). These results confirm that the film is purely (110) oriented. Since the intensity of the apical oxygen phonon at 500 cm^{-1} is higher in zz configuration, it suggests that the polarization of light is parallel to c-axis and xx/yy spectrum indicates that the polarization of light is perpendicular to c-axis.

The apical oxygen phonon at 500 cm^{-1} corresponds to the c-axis vibration of the O_4 oxygen atom and thus corresponds to the level of oxygenation in the film. For $\text{YBa}_2\text{Cu}_3\text{O}_7$, the Raman line is at about 502 cm^{-1} [125]. In our samples the line is at about 500 cm^{-1} which indicates a high but not full oxygenation of the film.

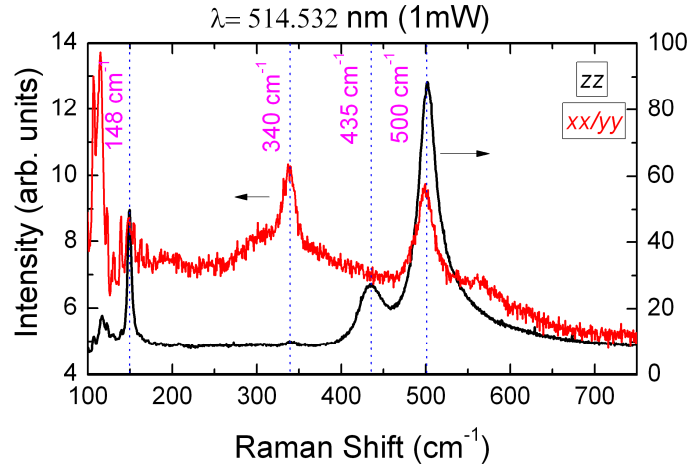


Fig. 30: Raman spectra of a YBCO (110)-oriented thin film of a thickness of 2000 Å with two perpendicular polarizations.

As a reference Raman spectra of a twin-free YBCO single crystal is given in Fig. 31, indicating the same features for the different polarizations of the incident and the scattered beam [124].

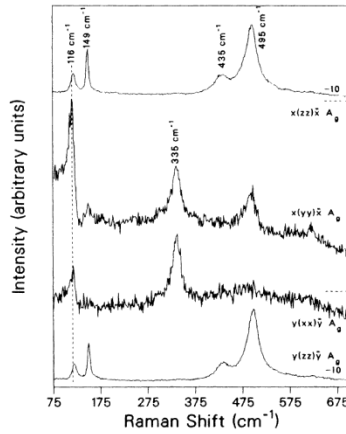


Fig. 31: Raman spectra of twin free YBCO single crystal [124] (zz signal is divided by 10).

The orientation of the c-axis in the film plane can be judged from AFM figures where a nearly perfect alignment of the grains along the [1-10] direction of the substrate is observed (Fig. 32).

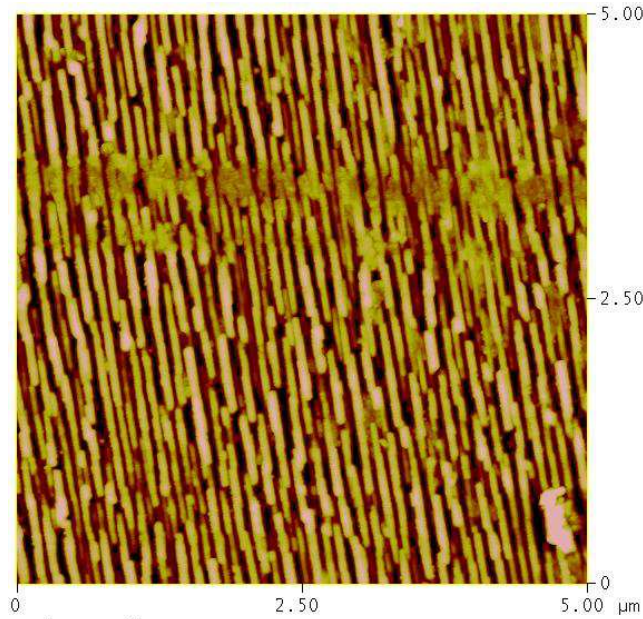


Fig.32: AFM picture of the surface of a YBCO film on (110) oriented substrate.

Magnetic properties of thin films were characterized using a quantum design vibrating SQUID magnetometer (VSM). Fig. 33 shows the temperature dependence of the magnetization $M(T)$ after zero-field cooling (ZFC) and field-cooling (FC) in an external in-plane magnetic field $H_{\text{ext}} = 10$ Oe.

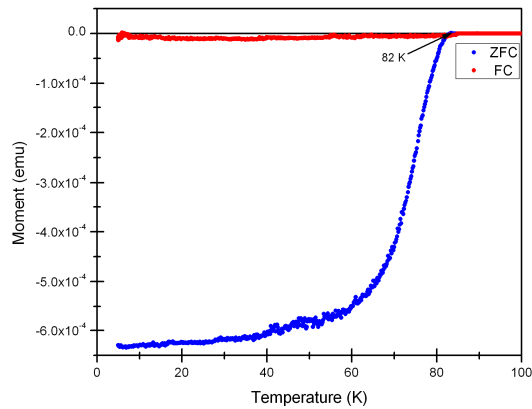


Fig. 33: Temperature dependence of magnetization of a 2000 Å (110)-oriented YBCO film in 10 Oe magnetic field parallel to sample surface (ZFC and FC).

The ZFC curve gives a clear diamagnetic signal starting at $T = 82$ K, at this temperature the superconducting transition takes place. The magnetic field dependence of the magnetization $M(H)$ is shown in Fig. 34. The measurement was taken at 5 K with applied field perpendicular to sample surface. The magnetization curve shows a hysteresis curve typical for superconducting films. From this curve one can estimate the critical current for the thin film:

$$j_c = \frac{15\Delta M}{R} \quad (6)$$

Where j_c is the critical current, ΔM is the difference of the magnetization of the upper and lower branch of the hysteresis curve in emu/cm^3 and R is the average radius of the specimen. In our (110)-oriented films j_c is around $5.4 \cdot 10^5 \text{ A}/\text{cm}^2$ at 5 K which is around a factor of 100 smaller in comparison with c-axis oriented (001) YBCO thin films. This difference in our (110)-oriented films is due to the fact that the supercurrent flowing in the sample plane is flowing the c-direction while in (001) YBCO thin films the supercurrent flows in the Cu-O planes.

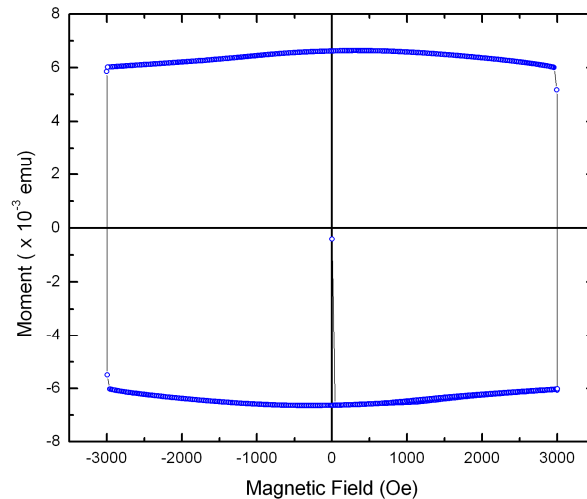


Fig. 34: Magnetization curve of a (110)-oriented YBCO film (thickness ????) $M(H)$ with the field normal to sample surface.

Transport properties

The resistivity of the films and its temperature dependence were measured using the standard four-probe method in a Physical Properties Measurement System (PPMS). L-shape masks were fabricated on

the films in order to investigate the electrical transport properties of these films where one could measure the resistivity of thin films along c-axis and along Cu-O planes simultaneously using two independent measurement channels. Fig. 35 shows the temperature dependence of the resistance of a 2000 Å film along the c-axis and the Cu-O planes, respectively. The measurement shows the film to exhibit metallic behavior along the c-axis and the Cu-O planes which is considered as a fingerprint of high quality YBCO thin films. The resistivity in these films is around 10 fold higher than what is reported for single crystals. The anisotropy ratio of the resistivity between c-axis and ab-plane in our films (ρ_c/ρ_{ab}) at 100K is around 24 which is smaller than what have been previously reported in twin free single crystals, (ρ_c/ρ_a) = 63 [19]. The superconducting transition starts at 92 K and the resistance reaches zero at 86 K. The sharp transition together with the previous observations are proof of the high quality of the thin film.

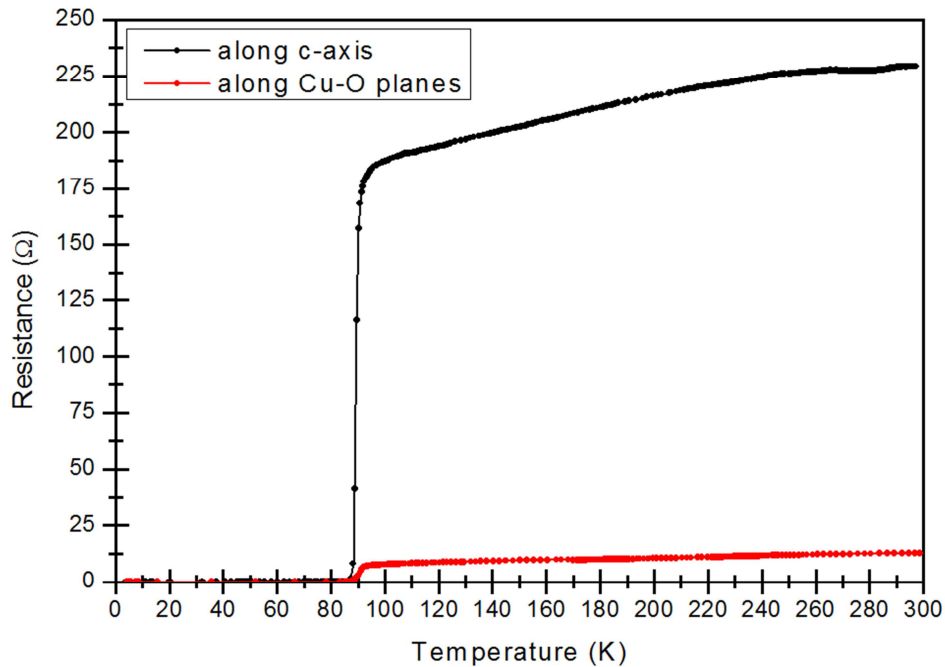


Fig. 35: Temperature dependence of a 1000 Å thick (110) oriented YBCO thin film (red: measuring along c-axis and black: measuring along Cu-O planes).

4.1.2 LCMO (110)-oriented films

(110) $\text{La}_{0.7}\text{Ca}_{0.3}\text{MnO}_3$ (LCMO) thin films exhibit an in-plane magnetic anisotropy which can be useful for the study of magnetic and superconducting interactions in heterostructures. This also opens the door to fabricate magnetic switches, spin valves and many more applications. The properties of LCMO thin films in general depend crucially on oxygenation level, strain and the microstructure of the film [126-129]. Because of this, more effort should be made in order to optimize film properties.

The growth conditions of (110) LCMO have been studied in other works [130, 131]. Optimally, LCMO is grown at $T_d = 750^\circ\text{C}$ and at 0.27 mbar Oxygen partial pressure. Unfortunately these conditions are not suitable for the growth of heterostructures as the temperature is too high and the pressure is too low for the growth of YBCO layers in these heterostructures. In this work, we restrict growth conditions of LCMO so we could grow (110) oriented YBCO layers in them. Namely the deposition temperature is $T_d = 720^\circ\text{C}$ and the O_2 pressure is 0.4 mbar.

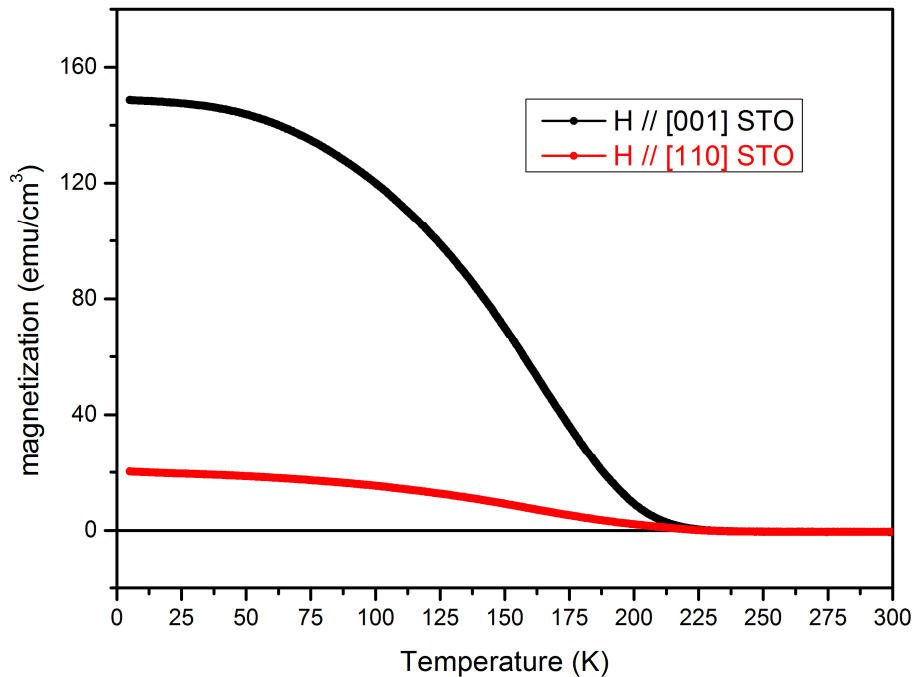


Fig. 36: Temperature dependence of magnetization of a 500 Å (110) oriented LCMO thin film

Fig. 36 shows the temperature dependence of magnetization of a (110)-oriented a 500 Å thick LCMO thin film. The external field was applied parallel to the film surface and along the crystallographic directions [001] and [1-10] of STO substrate. The results clearly show the in-plane magnetic anisotropy of LCMO where [001] and [1-10] are the soft and the hard axes respectively which is in agreement with literature data [130]. The ferromagnetic order starts to develop at $T_{\text{curie}} = 225$ K. The saturation magnetization of the film is around 160 emu/cm^3 which is much smaller than the magnetization value in bulk LCMO (550 emu/cm^3). Growing at relatively low deposition temperatures is one of the reasons that contribute to the small magnetization in these films.

4.2 (110)-Oriented YBCO-LCMO Heterostructures

(110) YBCO-LCMO heterostructures have been prepared using the PBCO-template technique according to the deposition scheme as described in Chap. 3.3. The PBCO template technique combined with the appropriate temperature-time profile during deposition yields single phase (110)-oriented bilayers. The inset of Fig. 37 shows a sketch of the resulting structure for a YBCO layer thickness of 100 nm and an LCMO layer thickness of 50 nm. The X-ray diffraction pattern displayed in the main panel of Fig. 37 exhibits sharp, intense doublets at scattering angles $2\theta \sim 32.5^\circ$ and $\sim 69^\circ$. The higher-intensity component comes from the (110) and (220) planes of the substrate, whereas the lower-intensity peaks arise from the LCMO/YBCO/PBCO film stack and can be assigned to the (110) and (220) reflections, respectively. These data confirm the absence of YBCO (001) grains as well as a perfect material purity (i.e. the absence of mixed composites). The peak marked with the asterisk is due to the sample holder of the diffractometer.

Heterostructures with LCMO layer thicknesses between 50 and 100 nm and YBCO layer thicknesses between 30 and 100 nm showed similar results.

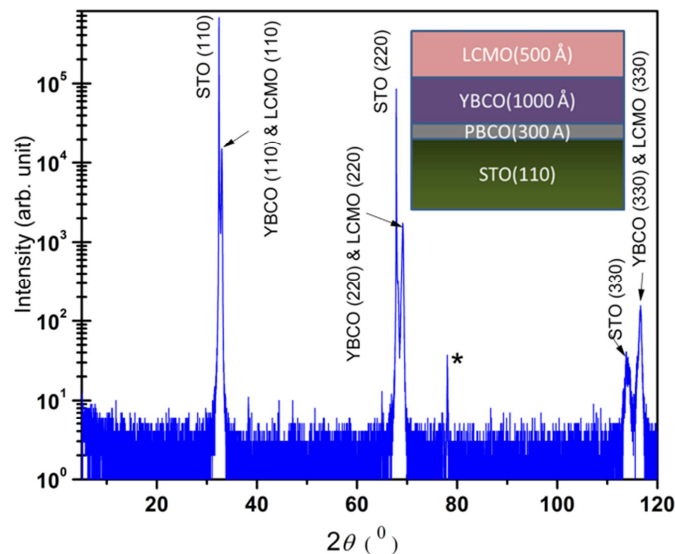


Fig. 37: X-ray diffraction of a (110) oriented heterostructure

Similar to the analysis of the orientation of single layer YBCO (110) films a careful x-ray pole figure analysis has to be made to prove the desired orientation of the YBCO-LCMO film stack. Since the (220) reflection of LCMO and the (110) and (103) reflections of YBCO appear at nearly identical 2θ -values in X-ray diffraction, additional measurements are required to confirm the (110) phase purity. To this end, pole figures in the YBCO (117) orientation were chosen, because there is no overlap with any of the STO or LCMO reflections (Fig. 38a). On the other hand, reflections arising from (103)- or $(10\bar{3})$ -oriented grains of YBCO would be clearly visible in addition to the YBCO (110) peaks. The absence of such reflections in the pole figures clearly demonstrates that the films are exclusively (110) oriented, within the detection limit of x-ray diffractometry. To check the orientation of the LCMO layer with respect to the substrate and the YBCO layer, the (116) plane of LCMO was chosen for an additional set of pole figures (Fig. 38b). Here, 12 peaks are observed in the scan, eight of which refer to reflections from the STO (221) plane, and four of which arise from the (116) reflection (or equivalent reflections) of LCMO. No other peaks of LCMO were observed, indicating that the LCMO layer is grown epitaxially with its (110) plane parallel to the (110) plane of STO. The pole figure analysis of the heterostructures thus demonstrates that the (110) planes of the STO substrate, the YBCO layer, and the LCMO layer are parallel to each other.

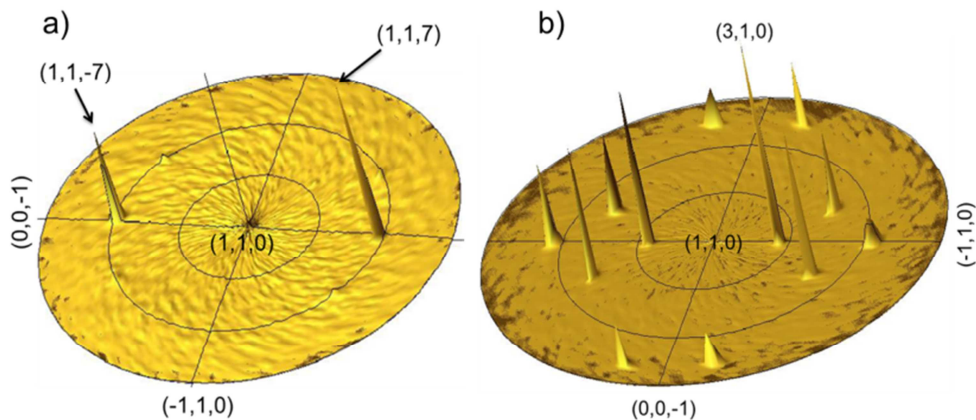


Fig. 38: X-ray pole figures of an LCMO (50 nm) – YBCO (100 nm) heterostructure (a) around the (117) reflection of YBCO, and (b) around the (116) reflection of LCMO.

The oxygenation state and perfection of the YBCO layer orientation were further investigated by Raman spectroscopy. Figure 39 shows Raman spectra with photon polarization parallel (zz configuration) and perpendicular (xx/yy configuration) to the YBCO c-axis. The frequency of the apical oxygen vibration around $\sim 500 \text{ cm}^{-1}$, which is very sensitive to doping, indicates a slight oxygen deficiency of the YBCO layer in our film ($\delta \sim 0.1$). The planar oxygen vibration at $\sim 340 \text{ cm}^{-1}$ of YBCO is present only if the incident and scattered photon polarizations are in the ab plane. Its absence in the zz configuration thus confirms the (110) orientation of the YBCO layer, in agreement with the x-ray analysis.

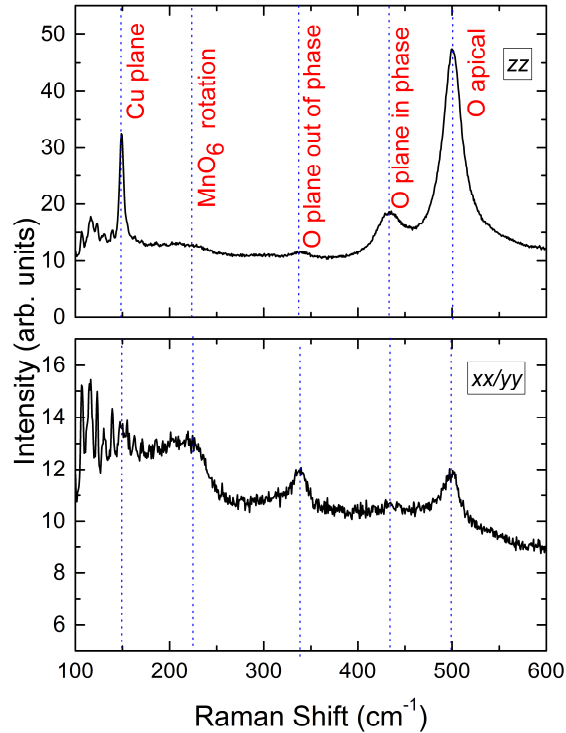


Fig. 39: Polarized Raman scattering spectra of an LCMO (50 nm) – YBCO (100 nm) heterostructure in a scattering geometry with incoming and reflected light parallel (top) and perpendicular (bottom) to the YBCO c-axis. The data were taken with a photon wavelength of 514.52 nm. The low-energy intensity seen in the xx/yy geometry is due to scattering from air.

Figure 40 represents the temperature dependence of the resistivity measured parallel (ρ_{ab}) and perpendicular (ρ_c) to the YBCO c-axis using a standard four-probe arrangement (inset in Fig. 40).

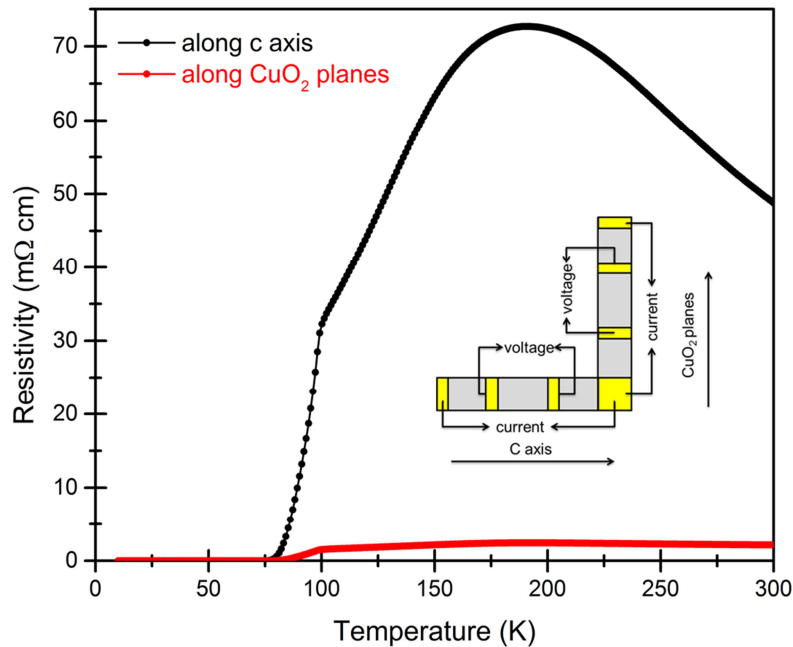


Fig. 40: Temperature dependence of resistivity of an LCMO (50 nm) – YBCO (100 nm) heterostructure parallel and perpendicular to the YBCO c-axis. The inset shows the arrangement of Au contact pads evaporated on the film surface.

The large anisotropy ($\rho_{ab}/\rho_c \sim 25$ at room temperature, ~ 35 at 180K) is consistent with the single-phase nature of the film inferred from the structural analysis. The temperature dependence of ρ_{ab} can be modeled as a network of parallel resistors and is hence dominated by the smallest value (~ 1 mΩcm for YBCO, compared to ~ 200 mΩcm for PBCO and ~ 20 mΩcm for LCMO). In the perpendicular direction (parallel to the c-axis of YBCO), the resistances of all layers of the film contribute in series. The contribution of the LCMO layer can be recognized in the resistivity peak around the Curie-temperature that is typical for ferromagnetic LCMO films. This contribution is presumably responsible for the lower resistivity anisotropy of the film compared to bulk YBCO, where $\rho_{ab}/\rho_c \sim 100$ at optimal doping. Both resistivity curves reveal a

superconducting transition with an onset around 90 K, and zero resistivity (within the measurement error) around 75 K. The rounding of the superconducting transition may reflect intrinsic interfacial effects (such as the transfer of spin-polarized quasiparticles across the interface) and/or residual inhomogeneity of the oxygen content within the YBCO layer.

Figure 41 shows the magnetic moment of the film measured in a magnetic field $H = 10$ Oe applied in different directions. The superconducting transition is most readily apparent if the field is applied perpendicular to the film plane (main panel of Fig. 41). The critical temperature determined in this way coincides with the zero-resistance state determined by the transport measurements (Fig. 40). When the field is applied in the film plane, the signature of superconductivity in the magnetization data is more subtle, due to the smaller screening current loops for fields applied in this direction. On the other hand, for this field direction the shape anisotropy that confines the ferromagnetic moment of the LCMO layer to the film plane greatly facilitates the determination of the Curie temperature, which is observed to be ~ 220 K – close to (but somewhat lower than) the bulk value of ~ 270 K. Likewise, the saturation magnetization of our film ($\sim 2 \mu\text{B}$ per Mn atom; data not shown) is lower than the corresponding value in bulk crystals and in bulk-like LCMO films [67]. Further work is required to assess whether the reduction of the Curie temperature and saturated moment has an intrinsic origin, or whether it is due to a slight off-stoichiometry of the LCMO layer in the film. In summary, we have shown that our YBCO-LCMO bilayers grow epitaxially, with the (110) planes of LCMO, YBCO, and STO parallel to each other. Admixtures of (001) and/or (103) grains of YBCO are below our detection limit. The charge transport and magnetic properties of the film are highly anisotropic, as expected based on the anisotropic electronic structure of YBCO. The deposition procedure we established thus opens new perspectives for the exploration of the interplay between high-temperature superconductivity and ferromagnetism in metal-oxide heterostructures.

By mastering the technological difficulties to fabricate high quality single phase (110)-oriented YBCO-LCMO bilayers and exploring their macroscopic properties, a fundamental prerequisite for in-depth microscopic investigations of YBCO-LCMO interfaces where the CuO_2 planes of YBCO are oriented perpendicular to the substrate plane has been accomplished. Comparing the results of the macroscopic measurements with those of c-axis oriented bilayers of the same composition, we observe a reduction of T_c from 89K (c-axis oriented bilayers) to 75 K for (110) bilayers. This may indicate that in the case of the (110) bilayers the interactions at the interface generate a different orbital reconstruction, charge transfer and magnetic polarization at the YBCO side compared to the c-axis bilayers. More elaborate experiments using advanced resonant x-ray techniques remain a task for the future.

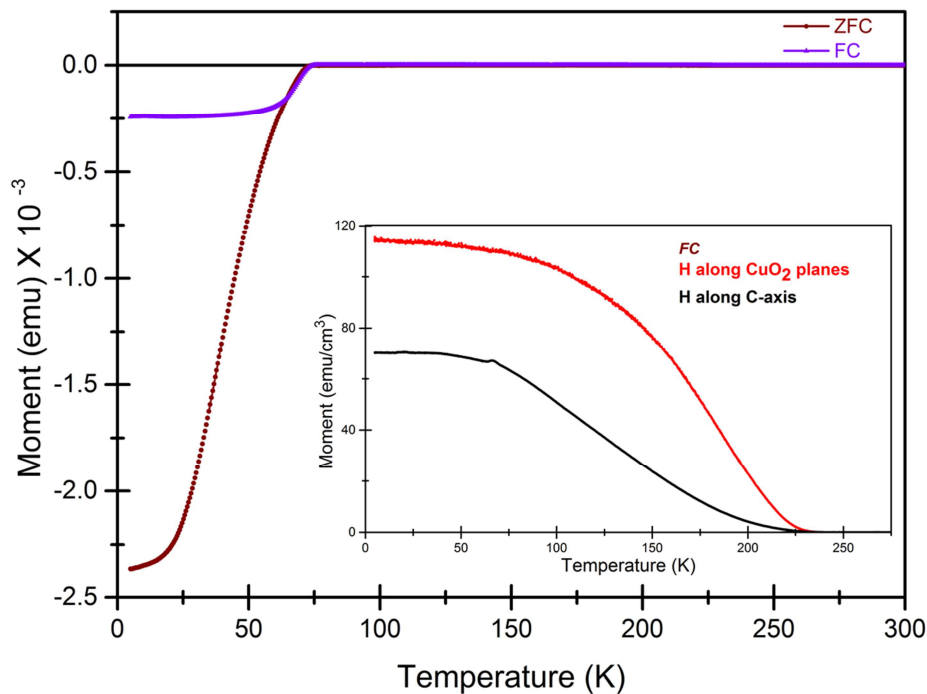


Fig. 41: Temperature dependence of the magnetic moment of an LCMO (50 nm) – YBCO (100 nm) heterostructure determined by Superconducting Quantum Interference Device (SQUID) magnetometry in a magnetic field $H=10$ Oe applied perpendicular to the film plane. The inset shows a measurement with $H=10$ Oe applied parallel to the film plane, either parallel or perpendicular to the YBCO c-axis.

4.3 FSF LCMO/YBCO/LCMO (LYL) Trilayers

As we have seen in the previous chapters, hybrid structures of YBCO and LCMO have extensively been used to explore possible interference effects between ferromagnetism and superconductivity. However, the vast majority of the investigations performed so far were done on (001) oriented systems. We took the chance to study the trilayers with the CuO_2 planes either perpendicular (in case of (110)) or with a well-defined tilt angle of 45° with respect to the YBCO-LCMO interface. Here we report on the structural and magnetic properties of (103)-oriented ferromagnet-superconductor-ferromagnet oxide trilayer thin films with the intention to explore the consequences of interference effects at the interface on the macroscopic magnetic properties.

(50-50-50) nm thin LCMO-YBCO-LCMO films were grown on (110) STO and 3.5° off-cut (110) STO substrates using conventional PLD techniques. It is well established that deposition under optimal growth conditions for YBCO on (110) STO would result a mixture of the competing (103) and $(10\bar{3})$ orientations. Using 3.5° off-cut (110) STO substrates favors the growth of only one of these competing orientations, and in optimized deposition conditions films can be obtained with one orientation completely suppressed [132]. It is important to note that in both cases YBCO will grow in such a way that the c-axis of YBCO is oriented at 45° with respect to the STO surface plane. In Fig. 42 the YBCO growth on a normal cut (110) STO (a) and on a 3.5° off cut (110) STO (b) is shown schematically.

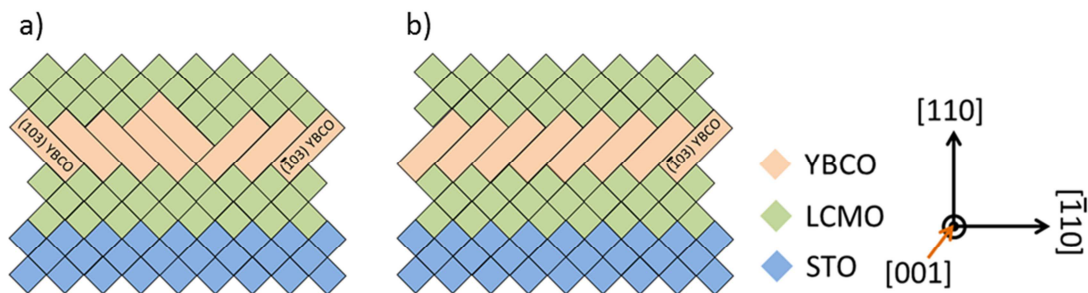


Fig. 42: a schematic of YBCO growth on a) normal cut (110) STO and b) on 3.5° off cut (110) STO.

The perfection of the YBCO orientation can be tested by pole figure XRD measurements where the relative positions of reflections indicate the out of plane orientation of the film. To accomplish this we focused on the reflection of the (117) plane of YBCO. If the YBCO thin film is grown with only one of the two orientations [(103) or (-103)], the pole figure will show two peaks at $\Psi = 30^\circ$ separated by an angle $\Delta \phi = 92^\circ$ and two more at $\Psi = 72^\circ$ separated by an angle $\Delta \phi = 46^\circ$. A mixture of the two orientations would appear as four peaks at $\Psi = 30^\circ$ and four peaks at $\Psi = 72^\circ$. The relative intensities of the peaks indicate the relative ratio of the different orientations i.e. if the peak intensities at say $\Psi = 30^\circ$ are equal this means that there is a 50% - 50% ratio of (103) and ($\bar{1}$ 03) domains.

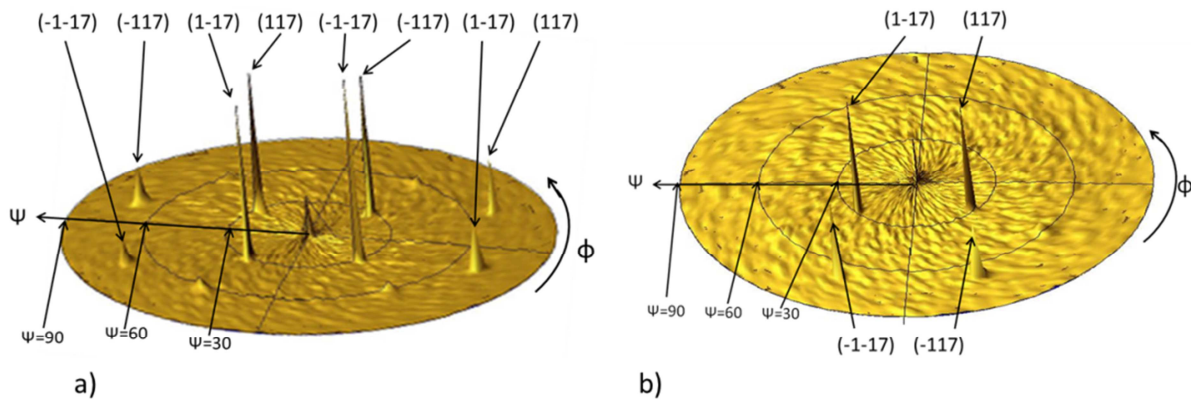


Fig. 43: Pole figures for a) Type-I and b) Type-II.

Fig. 43 shows the pole figures of trilayer samples grown on a) normal cut and b) 3.5° off-cut (110) STO. A mixed (103) and ($\bar{1}$ 03) is seen in a) whereas b) shows reflections of only one orientation which indicates perfect film orientation within the resolution of X-ray diffractometry. For simplicity we call trilayers grown on normal cut STO type-I and trilayers grown on off-cut STO type-II.

The magnetic properties of the films were investigated using a SQUID-Vibrating-Sample Magnetometer (SQUID-VSM) where external magnetic fields were applied parallel to the film surface either along the [001] or [1-10] direction, respectively, to investigate the in-plane magnetic anisotropy. Fig. 44 shows the magnetization as a function of external field at 100K for both films. The field was applied parallel to sample surface, again either parallel to the [001] or the [-110] directions. The blue line is for field applied along the easy axes and the red line is when field is applied along the hard ones. When the field is along the easy axes, two coercivities are observed with a difference of 100 Oe. These different coercivities correspond to the two different magnetic layers in the film which is caused by the different strain state for LCMO grown on STO or LCMO grown on YBCO. This could be potentially useful for magneto-transport measurements in these films where it is possible to switch the magnetization of one of the magnetic layers and leaving the other unchanged.

Fig. 45 a) and b) show the DC magnetization as a function of temperature for Type-I Type-II samples respectively. The external applied field for these measurements was 10 Oe. The magnetic response of the trilayer depends on the direction of the magnetic field as the LCMO layers exhibit an in-plane magnetic anisotropy. The measurements suggest that the hard axis of LCMO is aligned along the $[-110]$ direction of STO and the easy axis is aligned along the c-axis of STO.

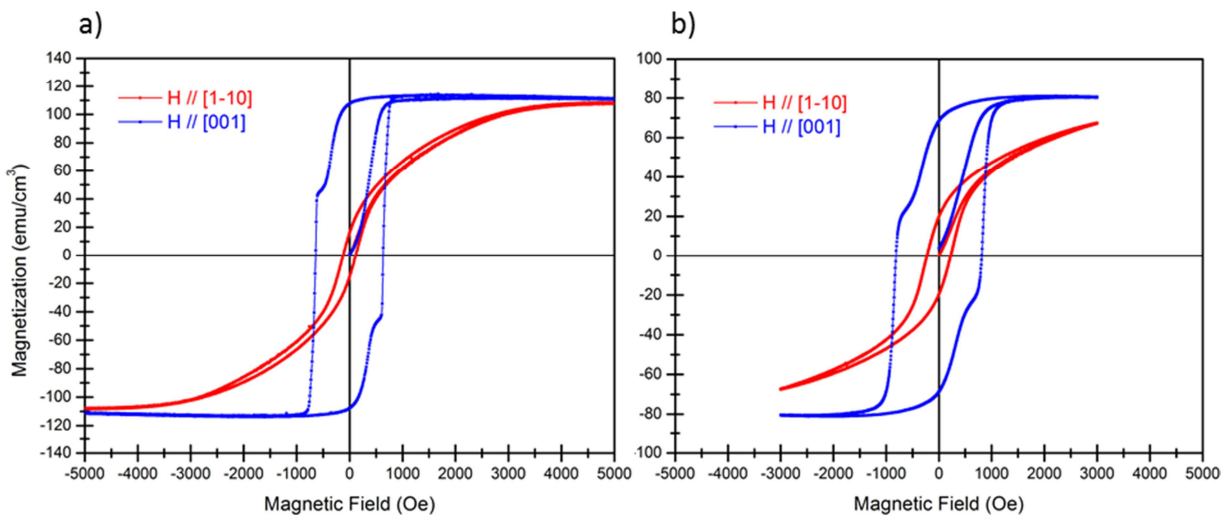


Fig. 44: Magnetization as a function of external field at 100K for a) Type-I and b) Type-II.

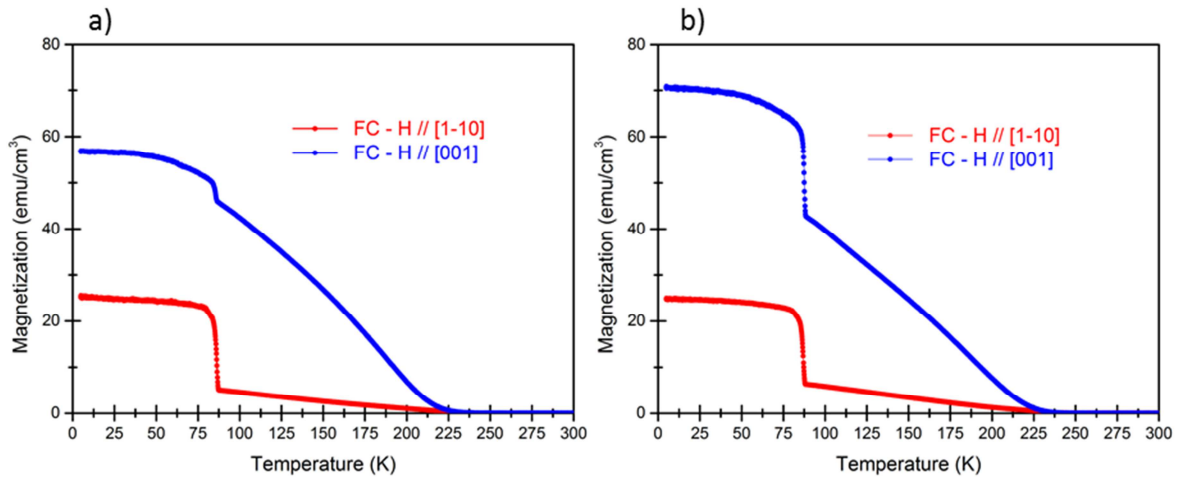


Fig. 45: FC magnetization as a function of Temperature with 10 Oe external field applied in plane for a) Type-I and b) Type-II.

FC measurements show that both films start to exhibit a ferromagnetic ordering upon cooling below T_{curie} around 235K. A sudden increase of the magnetization appeared at temperatures just below the superconducting transition and a saturation of the magnetization is reached as the temperatures decreases further. Such positive increase is counter-intuitive as the superconductor is expected to show a diamagnetic response (Meissner effect). This increase is often referred to as the Paramagnetic Meissner Effect (PME).

A similar effect, the increase of magnetic moment, was also observed recently in superconducting/ ferromagnetic heterostructures (S/F) of different composition [133–140] with both HTSC and conventional superconductors. Different models were proposed for the explanation of PME in S/F structures. One of them is based on an electrodynamical mechanism. It considers a stray field produced by the ferromagnetic layers and the response of the superconductor to it [136–138]. A second model is based on the exchange coupling of electrons at the S/F interface [132,133,139] due to the proximity effect. At the moment, the nature of PME in S/F structures is still under debate and a consensus has not yet been reached.

The field dependence of the PME signal is shown in Fig. 46. The magnetic field was applied in-plane along the hard axis of the film. At temperatures $T > T_c$ the film is close to saturation at 2000 Oe. However, as the film reaches T_c the magnetic moment starts increasing and continues to do so as the temperature goes down to 5 K. The magnetic moment at 5 K exceeds the expected saturation moment for the film, but it is still below the reported saturation magnetization of bulk LCMO.

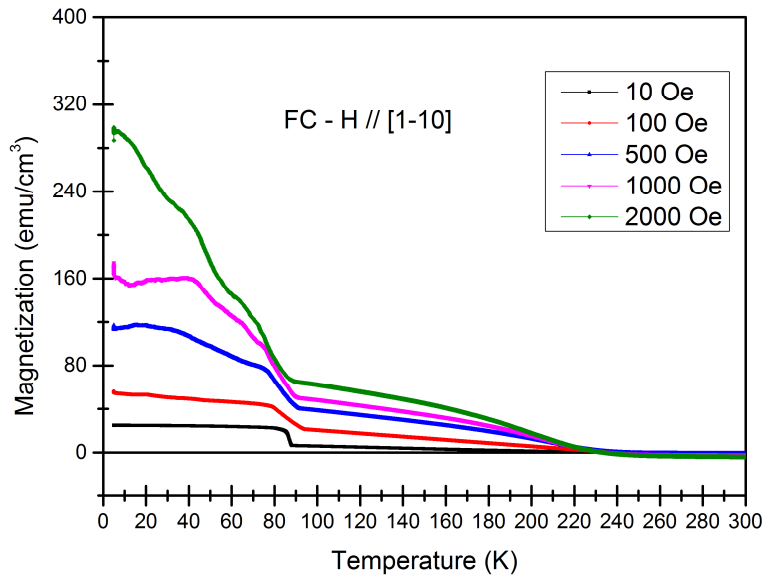


Fig.46: FC measurement of magnetization as a function of temperature for the sample Type-I at different external fields.

To explain the increase of the magnetic moment below T_c in these heterostructures we propose an alternative model. Since YBCO is a type II superconductor, vortices may play a role in this system. The magnetic induction of the vortex core is aligned parallel to the external field. During field cooling at temperatures just below T_c , vortices are created in the superconducting layer. Cooling well below T_c these vortices are attracted to the S/F interface. There are several explanations for the attraction of vortices to the S/F interface. For example the attraction of the vortices to the bulk superconductor surface discovered by Bean and Livingston [165], or pinning

of the vortices to the S/F interface by magnetic defects or roughness which may support the correlation of the PME and the granularity of the ferromagnetic layers [160].

Transport properties of this tri-layer system were investigated using the PPMS. The film mask was fabricated as explained in chapter 3.4.3. The voltage was applied in the film plane along the crystallographic directions [001] and [1-10] of the STO substrate. The in-plane transport anisotropy $\rho_{[1-10]} / \rho_{[001]}$ is around three, which is close to the anisotropy of (103) YBCO films. The metal-insulator transition in these films is apparent around $T=240\text{K}$ indicating a high Curie temperature. The superconducting transition starts at 90 K and reaches zero resistance at 72K.

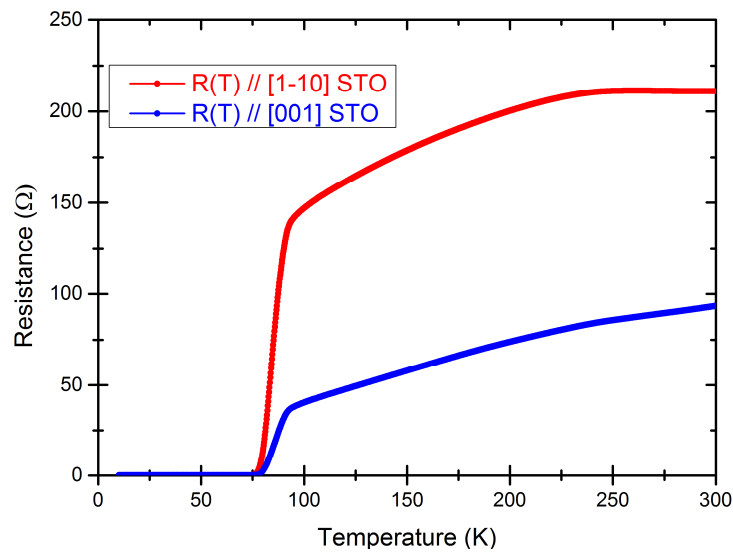


Fig. 47: Temperature dependence of resistance of a type II tri-layer film.

As mentioned earlier, the difference between the coercivities of the two LCMO layers in the film is useful for magnetotransport studies of this system, where one can control the relative orientations of the magnetization in the magnetic layers and study the effect of their alignment (parallel or antiparallel) on the transport properties of the trilayer. In this work, all transport measurements were performed in the film plane. In out of plane measurements the effect of spin orientation on electric transport is expected to be more pronounced, but these measurements require a more complex contact geometry.

To achieve parallel alignment one has to apply a magnetic field (negative or positive) that exceeds the coercivities of the two layers. To align the magnetic layers antiparallel to each other one should first apply a magnetic field higher than the coercivities of the two layers and then switch to a field with opposite direction and with a value higher than the coercivity of one layer and lower than the other ($H_{c1} < H_{ext} < H_{c2}$). Fig. 48 shows the possible parallel and antiparallel alignments and the field range in which the antiparallel alignment is possible.

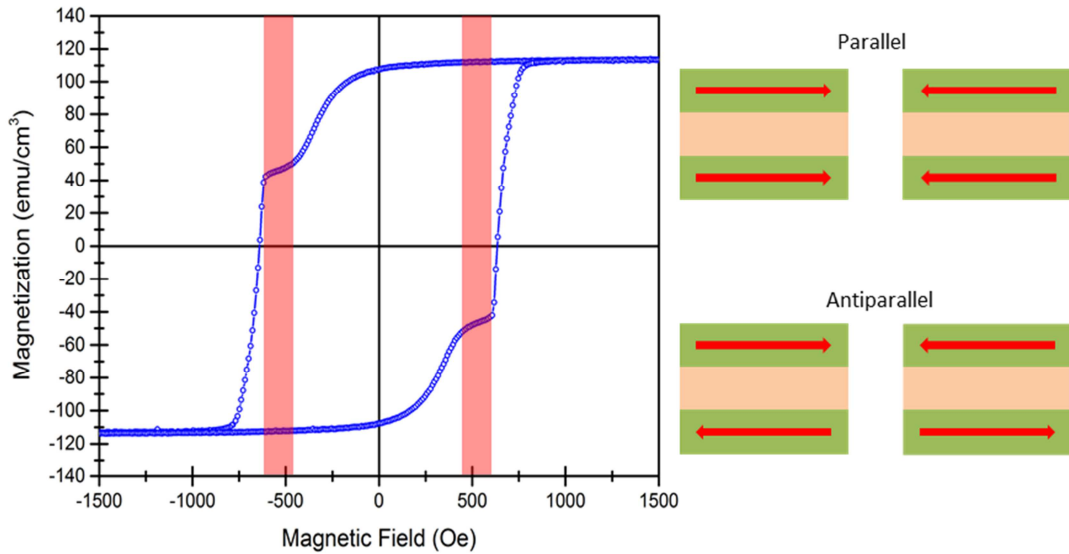


Fig.48: The red areas indicate the field in which the magnetic layer can be aligned in an antiparallel configuration.

Fig. 49 shows the normalized magnetization as a function of external field (blue) and the in-plane magnetoresistance measurement of the tri-layer (green). The red lines indicate the fields at which antiparallel alignment is established and the arrows point to the sweeping direction of the external magnetic field. The external field was applied in the sample plane and along the easy axis of the ferromagnetic layers.

In general, at temperatures close to T_c the transport is dominated by the superconductor response to the magnetic field, however, at $T > T_c$ the magnetoresistance is dominated by the response of the ferromagnetic layers. At higher fields, the response is typical of LCMO, namely, negative magnetoresistance. But at lower fields, the films exhibit double peaks and show a minimum in resistance whenever the two magnetic layers are aligned antiparallel to each other. This can be understood as a superposition of the Giant Magnetoresistance (GMR) effect and the change in resistance at the magnetic domain walls (DWs). As the magnetic layers starts to align antiparallel to each other the resistance starts to increase due to GMR and scattering from DWs. Once the softer magnetic layer is completely flipped the scattering from DWs is reduced which causes a drop in resistance. As the second magnetic layer starts to flip the resistance starts to increase again to reach the second maximum.

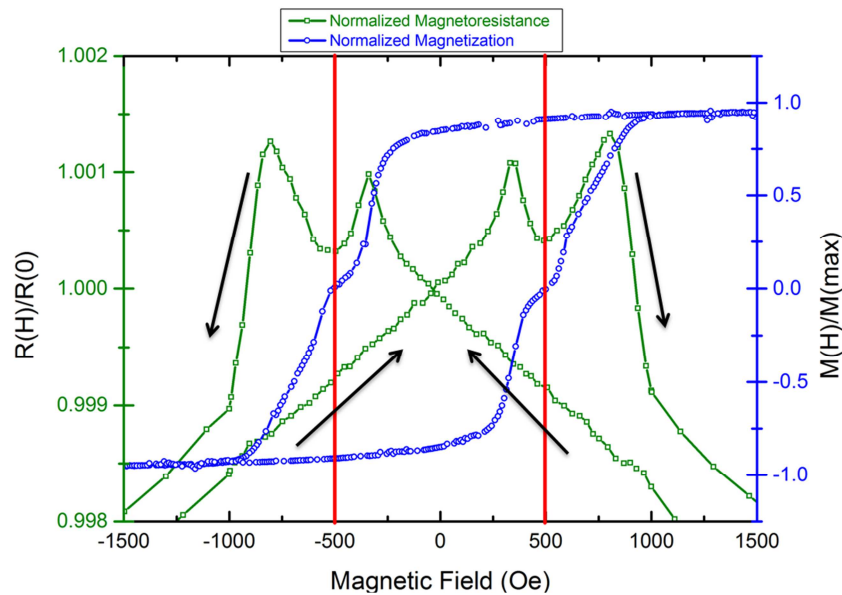


Fig. 49: In-plane magnetoresistance measurement of the tri-layer overlapped with the magnetization as a function of external field. The tri-layer exhibits a minimum whenever the magnetic layers are aligned in an antiparallel configuration.

Magnetoresistance was measured simultaneously along [001] and [1-10] directions of substrate and performed at different temperatures. The double peak effect is present in both directions and persists up to 150 K. Fig. 50 shows the data for $T = 90, 100,$ and 125 K .

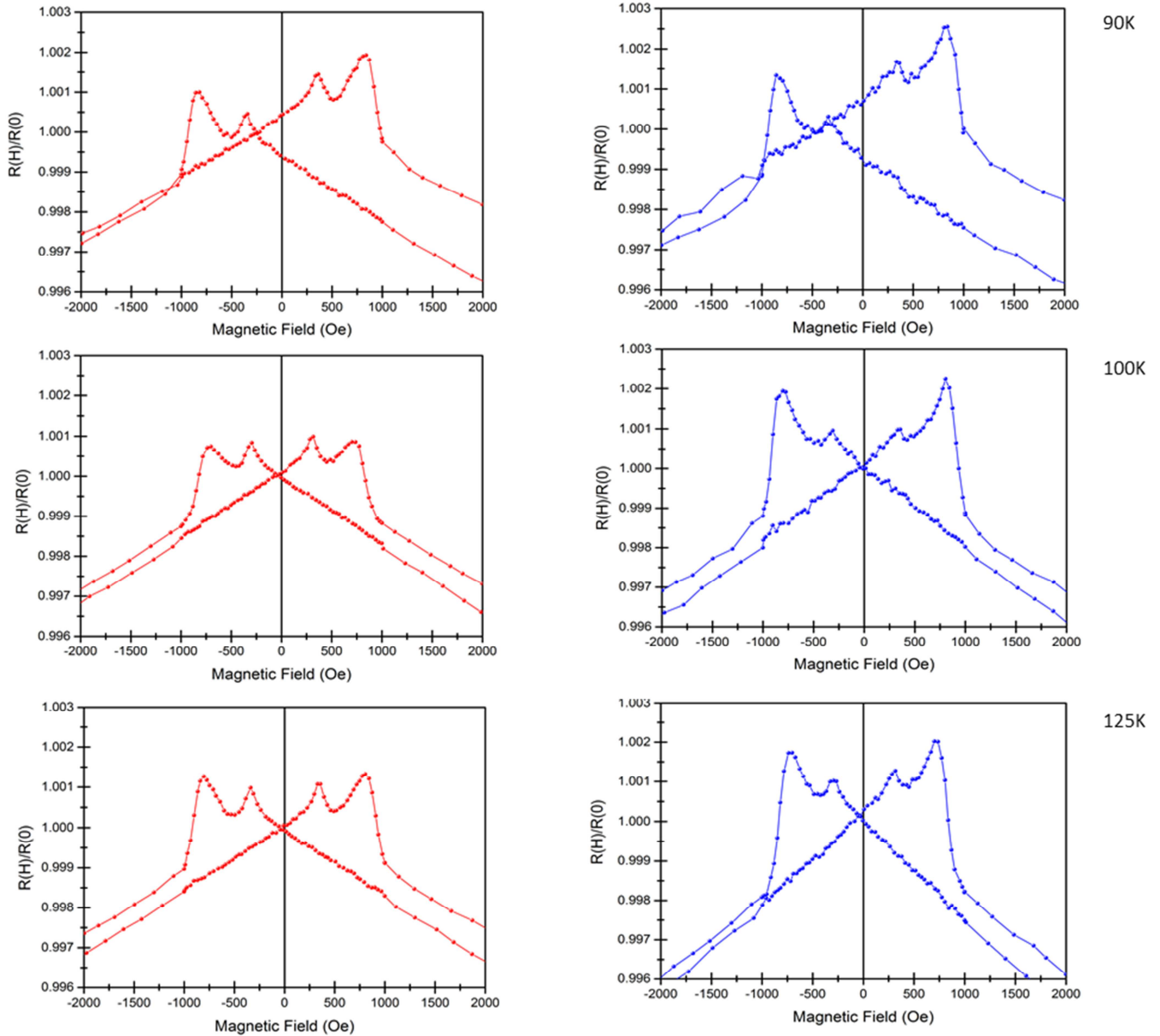


Fig. 50: Normalized magnetoresistance of the tri-layer at different temperatures along both directions ($\parallel[001]$ red and $\parallel[1-10]$ blue).

4.4 SFS YBCO/LCMO/YBCO (YLY) (110)-oriented Trilayers

After having accomplished the technological prerequisites to fabricate (110)-oriented YBCO single layers and (110) YBCO-LCMO bilayers the feasibility of fabricating (110) SFS trilayers and thus planar SFS-Josephson junctions is explored. In this section it is shown that an ultra-thin LCMO ferromagnetic layer with a thickness of a few unit cells can be grown in between two thick YBCO superconducting layers. In particular, the ferromagnetic transition temperature is found to be $T_{\text{Curie}} \sim 260\text{K}$, which is close to the bulk value. This opens up a way to investigate the electronic transport across the thin ferromagnetic layer with two possible perspectives: (i) to fabricate planar oxide SFS Josephson junctions and (ii) to contribute to the understanding of the proximity effects in oxide SFS-structures with strong correlation. Whereas in conventional Josephson junctions the participating superconducting parts are coupled across the barrier of a thickness corresponding to the coherence length by symmetric ground states, in SFS junctions the coupling can be antisymmetric, depending on the layer thickness. Unusual properties of SFS-Josephson junctions have been predicted for conventional s-wave metallic superconductors [141, 142]. An experimental breakthrough has come only recently [143,144]. In these studies SFS-Josephson junctions with weakly spin polarized ferromagnetic barriers like copper-nickel or palladium-nickel alloys were used to avoid strong suppression of the proximity effect. Recent observation of a supercurrent across the half-metal chromium dioxide [145-147] triggered intense activity to study triplet supercurrents (i.e., long range proximity effects) both theoretically [148-150] and experimentally [151-154]. Therefore the successful fabrication of oxide SFS-structures may help to investigate and understand the long-range proximity effects between d- wave high T_c superconductors and half-metallic ferromagnetic LCMO layers. Little is known about the feasibility of fabricating oxide SFS-Josephson junctions. This holds, in particular, for the subsequent exploration of the properties. Therefore the successful fabrication of oxide SFS-structures may help to investigate and understand the long-range proximity effects between d-wave high- T_c superconductors and half-metal ferromagnetic LCMO layers. The main difficulty in accomplishing this type of junctions is a technological one and arises from the fact that the barrier thickness and coherence length must match to obtain a

supercurrent. Additionally, charge transfer, spin polarization, [155, 156] and structural effects at the interface can strongly suppress superconducting transport across the oxide ferromagnetic interface. In YBCO, the superconducting coherence length is extremely small and at the same time highly anisotropic ($\xi_{ab} = 1.6 \text{ nm}$, $\xi_c = 0.1 - 0.2 \text{ nm}$) [157, 158]. Therefore, the realization of planar SFS-Josephson junctions requires a barrier thickness in the range of 2–3 unit cells (1 nm); this is experimentally achievable if one can grow high quality (110) oriented YBCO with a ferromagnetic layer in between. In these heterostructures the ab-plane is perpendicular to the film plane and fulfils our requirement. Such structures can successfully be prepared. Additionally, the structural, magnetic, and transport properties of these oxide YBCO/LCMO/YBCO trilayer structures are investigated, using LCMO layers in the thickness range of a few unit cells and with different orientation of YBCO layers: (110)-YBCO and (001)-YBCO. The same conditions and layer thicknesses were used for formation of the (001) oriented structures on the (001) oriented SrTiO₃ substrates without a PBCO template. Fig. 51 shows a sketch of a (110) oriented

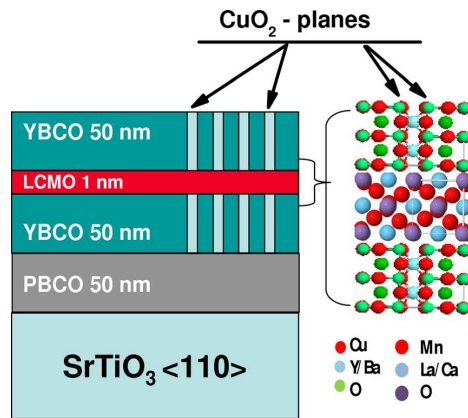


Fig. 51: Sketch of a typical sample used in this work. An ultra-thin ferromagnet is neighbored by two YBCO layers. A 50 nm PBCO buffer layer stabilizes the (110) orientation of YBCO.

structure with a 1 nm thick LCMO layer. A 1 nm thick LCMO layer consists of 2–3 unit cells (u.c.); therefore two out of three u.c. are exposed to a neighboring YBCO layer and their properties are strongly influenced by them, as found in many studies of LCMO/ YBCO hybrids and

superlattices. [9,16,107,159-162]. The film orientation and phase purity of every heterostructure were checked by X-ray diffraction (XRD). A $\Theta - 2\Theta$ scan for the sample displayed in Fig. 51 is shown in Fig. 52(a). Only two distinct peaks are found.

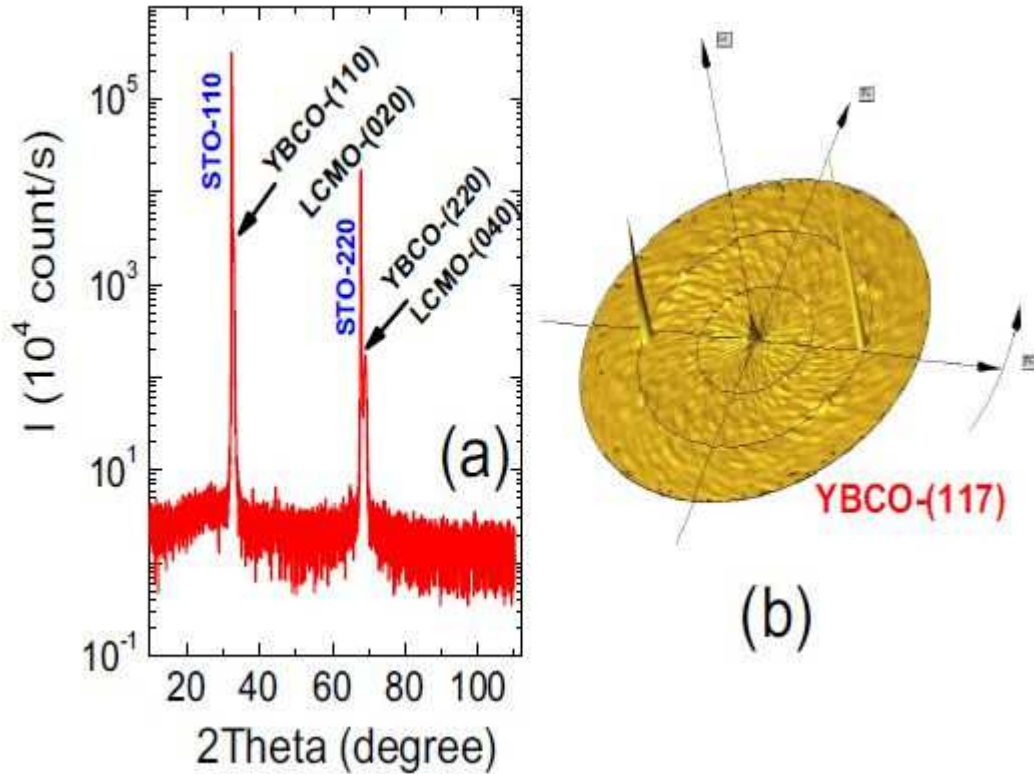


Fig. 52: (a) Θ - 2Θ scan (using Cu-source) for the sample shown in Fig. 52. Only (hk0) YBCO and (0k0) LCMO peaks appear. (b) Pole-figure for the YBCO (117) plane, the only two reflections appear from YBCO-(117). Here, no overlap from LCMO reflections prove that it is single phase and can be considered as textured film.

The first peak refers to the sum of overlapping YBCO, LCMO, and STO signals, namely, (110) for STO, (110) or (103) for YBCO, and (020) for LCMO. The second peak can be explained accordingly. In order to shed light on the YBCO orientation, a pole-figure analysis was made. The (117) reflection of YBCO was selected since there is no overlap to other reflections. The pole-figure in Fig. 52(b) shows two pronounced (117) YBCO peaks, (103) reflections of YBCO are not observed. This indicates that the YBCO layers in our heterostructures have (110) orientation. The results of the structural analysis of these films coincide perfectly with those

found in (110)-oriented YBCO-LCMO bilayers as described in section 4.2. A typical curve of the temperature-dependent magnetization $M(T)$ is shown in Fig. 53 for (110) YBCO/ LCMO/YBCO with $t_{\text{LCMO}} = 1$ nm. It is measured in an external field of $H=100$ Oe parallel to the film plane and, in this case, perpendicular to the copper oxide planes using a superconducting quantum interference device (SQUID)- magnetometer. The two curves show the zero field cooled (ZFC, blue) and field cooled (FC, red) regimes. The curves show a diamagnetic signal below $T=85$ K, which corresponds to the superconducting transition of the YBCO layers.

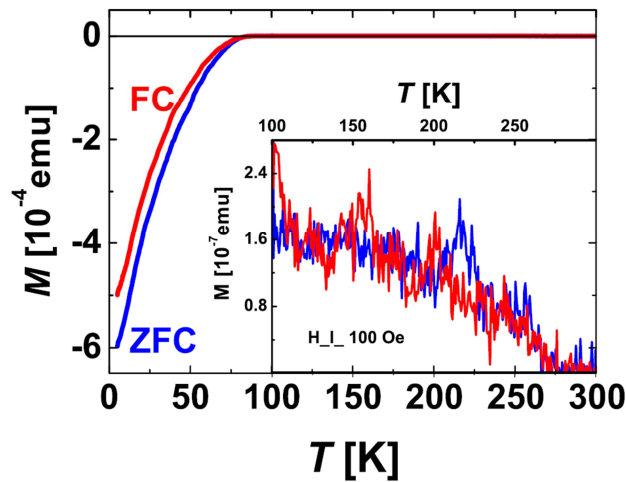


Fig. 53: Zero-field-cooled Magnetization measurements $M_{\text{zfc}}(T)$ (blue) of the YBCO-LCMO-YBCO heterostructures with 50 nm-1 nm-50 nm grown on a STO(110) substrate. The external field $H_{\text{ext}} = 100$ Oe is parallel to the substrate surface, i.e., perpendicular to the CuO_2 plane. T_c is 85 K.

The inset curve displays the magnification of both M_{zfc} and M_{fc} for $M(T > 100 \text{ K})$, identifying a typical behavior for a ferromagnetic LCMO layer with a Curie temperature of $T_{\text{Curie}} = 265$ K close to the bulk Curie temperature for LCMO ($T_{\text{Curie}} = 275$ K).

The inset shows a positive magnetization below $T=260$ K, indicating the ferromagnetic order of the LCMO layer with a thickness $t_{\text{LCMO}} = 1$ nm. Since it is known that the Curie temperature is strongly reduced in thin LCMO layers deposited on STO substrates,[88] a Curie temperature of $T_{\text{Curie}}=265\text{K}$ which is close to the bulk value of 275 K is a remarkable result. This is in agreement with previously published results [163], where we found that a 7 u.c. thick LCMO layer in between (001)- YBCO layers had a $T_{\text{Curie}}=210$ K. In all heterostructures used in the present study

we find a ferromagnetic ordering temperature of LCMO higher than 200K. Figures 54 (a) and 54(b) show the magnetic hysteresis loops $M(H)$ measured for different YBCO/LCMO/YBCO heterostructures at $T=5\text{K}$ (blue squares) and $T=100\text{K}$ (red circles). The top and bottom panels show measurements for LCMO thicknesses of $t_{\text{LCMO}} = 1\text{ nm}$ and $t_{\text{LCMO}} = 2\text{ nm}$, respectively, where the external applied field was applied perpendicular to the CuO_2 -planes in all cases. In the left column, the orientation of the YBCO is (110) and in the right column, (001). At $T = 100\text{ K}$, well above the superconducting transition of the YBCO layers and below the Curie temperature of the LCMO layer, the hysteresis loops (red circles) are typical for magnetic materials with slightly different values of the coercive field, remanence, and saturation magnetization M_s .

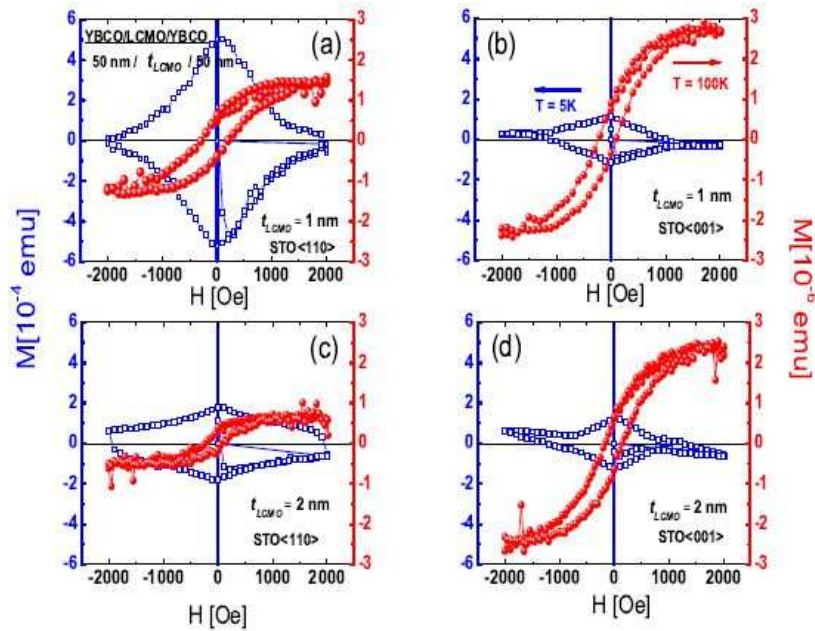


Fig. 54: Magnetization versus magnetic field $M(H)$ measured at $T = 5\text{ K}$ (blue) and at $T = 100\text{ K}$ (red) for the sample structure YBCO-50 nm/ t_{LCMO} /YBCO- 50 nm. The external applied field is oriented perpendicular to the CuO_2 -planes in all cases. The left panel (a and c) refers to samples grown on STO(110), where the right panel (b and d) to samples grown on STO(001). The upper panels shows the $t_{\text{LCMO}} = 2\text{ nm}$ films, the lower the $t_{\text{LCMO}} = 1\text{ nm}$ films.

Since we have a fraction of interface atoms of the order of 50% that are severely influenced by the interface configuration, these variations are not surprising. The measured magnetization

was corrected for the diamagnetic background of the STO-substrate in all cases. All samples show ferromagnetically ordered LCMO layers at 100K, however, the saturation magnetization per Mn-atom is in all cases much smaller ($0.2\text{--}0.4\mu_B/\text{Mn}$) than the bulk value of $3.6\mu_B/\text{Mn}$. The measurements at $T=5\text{K}$ (blue squares) in the superconducting state of the YBCO layers show wide hysteresis loops, characteristic for epitaxial YBCO films with strong pinning of Abrikosov vortices. Three out of four samples show similar behavior with a maximum magnetization at $H=0$ of about 2×10^{-4} emu. Only in the case of the (110)-YBCO/LCMO/ YBCO trilayer with $t_{\text{LCMO}}=1$ nm a strongly increased magnetization is found. The maximum value is found to be larger by a factor of 2.5, in this case 5×10^{-4} emu. This difference is attributed to the presence of a supercurrent across the 1 nm LCMO barrier in the (110)-YBCO/ LCMO/YBCO structure. This is reasonable for two reasons: the CuO-planes oriented perpendicular to the barrier exhibit a coherence length across the barrier to values larger than one nanometer. This is one order of magnitude more than in the case of the (001) oriented YBCO. This large coherence length might lead to a proximity coupling across a 1 nm thick LCMO layer, even if there is a significant suppression by the ferromagnetic state. In this simple picture, only one out of the four measured samples is a candidate for such a superconducting coupling. The combination of a small barrier thickness with a large coherence length is only fulfilled in the case of the (110)/1 nm sample. Only in this case is an increase in magnetization found. Note, a supercurrent flowing across the barrier would increase the sizes of possible closed current loops in the superconducting volume enormously. This leads to a significant increase of the measured diamagnetic signal. Similar effects were observed in magnetization loops measured in trilayer structures with non-magnetic barriers. Barrier layers of PBCO or STO in between (110) oriented YBCO layers can also lead to an increase of the measured magnetic moment when thin enough. This effect is only used as a preliminary test of the superconducting (Josephson) coupling in any type of barrier between two superconducting electrodes. Our data can be explained as well if the barrier is incomplete and pinholes allow the direct contact of two adjacent superconducting layers. For a more detailed test of the superconducting coupling between the YBCO electrodes, we patterned the heterostructures into smaller junctions with lateral dimensions of $300\mu\text{m} \times$

200 μm using photolithography and ion milling. The sketch of the junction is shown in the inner part of Fig. 55.

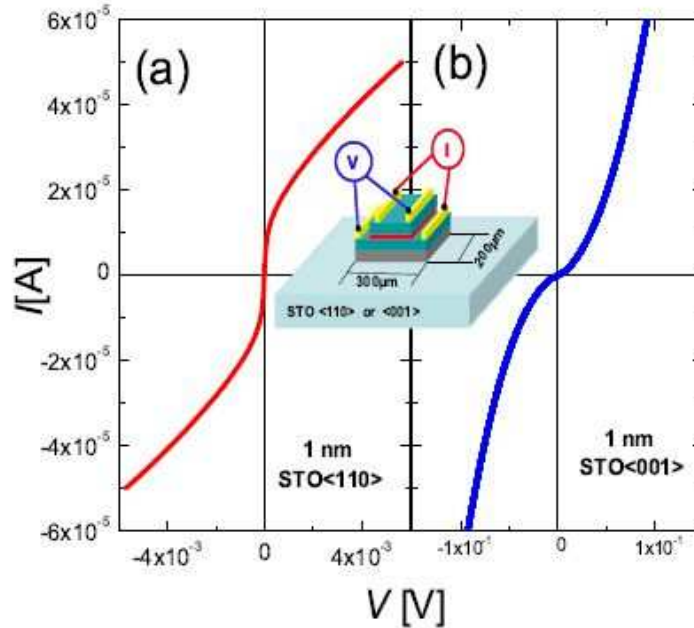


Fig. 55: I/V curves of current transport across the ferromagnetic barrier. Junctions with lateral dimension of 300 μm x 200 μm have been prepared by ion milling out of the heterostructures of YBCO-LCMO-YBCO (50 nm - 1 nm - 50 nm) grown on STO-110 (red) and 001 (blue), sketch is shown inset of panel (a). (a) I-V curve of the 110-sample shows a vertical slope at $V = 0$ indicating a superconducting transport with critical current of 1×10^{-5} A. (b) I-V curve of the 001-sample shows nonlinear behavior for I-V curve without any supercurrent flowing at $V = 0$.

Passing the current across the ferromagnetic junctions for both (110) and (001) cases in the (110)-sample (red curve) a nonlinear IV-curve with clear evidence of a finite supercurrent, I_s , 1×10^{-5} A, is observed. The non-linear shape of the I-V curve is not a typical one for Josephson junctions. Deviations might be related to flux flow effects but will not be considered any further. In contrast, the I-V curve of the (001)-sample (blue curve) does not show any supercurrent. The differential conductance does not show a zero bias conductance peak (ZBCP) in contrast to recent publications for ramp-type YBCO/LSMO ($\text{La}_{2/3}\text{Sr}_{1/3}\text{MnO}_3$) SFS-junctions, where the ZBCP is discussed in terms of an incomplete spin-polarization of the LSMO, the presence of domain walls, or faceting. [154, 164, 165] From the measured I-V curves of the

samples in (110) geometry, we extracted the values of the supercurrent with respect to temperature and magnetic field. Figure 56 depicts the temperature dependence of the critical current I_c . The top panel shows a critical current exhibiting a nearly linear behavior and vanishes at a temperature of about $T=20$ K. This is at least an unusual behavior for YBCO. A comparison with typical critical currents that can appear in YBCO along different crystallographic orientations is shown in the bottom panel of Fig. 57(b). The triangles refer to currents along the ab-plane and the circles indicate currents along the c-axis. All data are extracted from transport measurements performed in the adjacent YBCO films near the LCMO junction in the sample grown along the (110) direction. We can state that the current across the junction has a

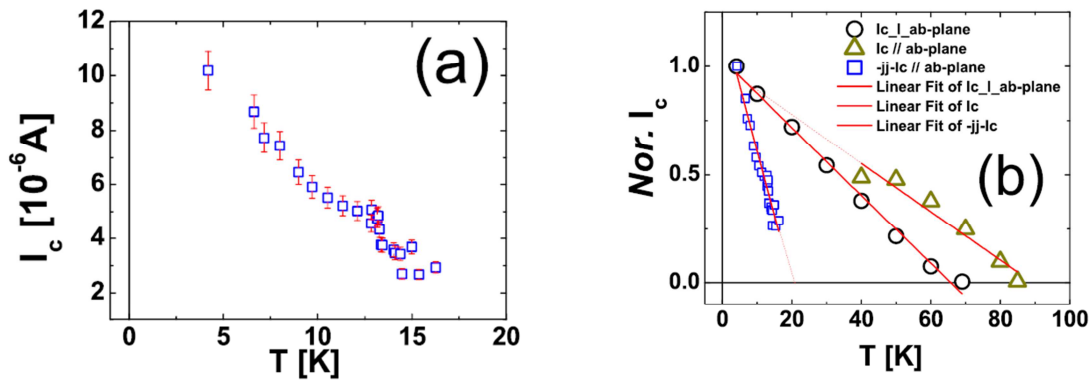


Fig. 56: (a) The temperature dependence of the critical current. (b) The critical current for junction and planer film. The triangles refer to currents along the ab-plane, the circles indicate currents along c-axis. All data are extracted from transport measurements performed in the adjacent YBCO films near the LCMO junction in the sample grown along (110) direction.

significantly different temperature dependence than any other current flowing inside the superconducting phase. This gives a significant indication that the observed current is not a regular current travelling across a pinhole in the LCMO layer allowing direct contact of both YBCO layers. Figure 57 depicts the field dependence of I_s ; the temperature is $T=4.2$ K and the field is oriented parallel to the ferromagnetic layer. A clear maximum of the critical current is found at $H=0$. With increasing field of either polarity, the critical current rapidly decreases. However, typical Fraunhofer patterns of a Josephson junction are not observed, which is attributed to two possible reasons.

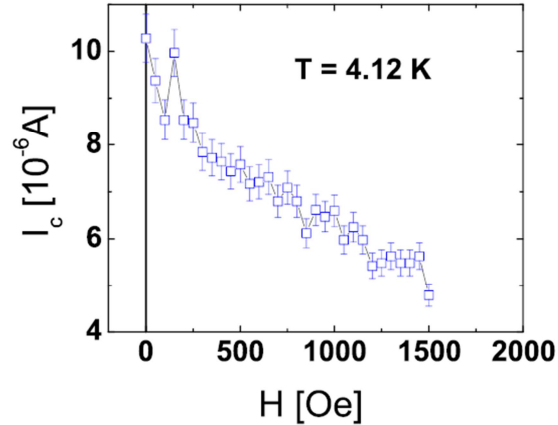


Fig. 57: Field dependence of the critical current at temperature $T = 4.12$ K the field is oriented parallel to the ferromagnetic layer.

First, the cross-section of the junction is very large, reducing the period of the expected Fraunhofer oscillations to a few micro-Tesla. Second, the large contact area probably leads to an inhomogeneous junction structure, which is also a reason for the absence of periodic structures. An interesting correlation can be found when comparing Fig. 58 with the blue curve in Fig. 55(a). Both measurements are plotted in the same magnetic field range and (roughly) at the same temperature. In both measurements a clear maximum is found at $H=0$ and an increase of the external field to values of about $H=1000$ Oe leads to a decrease of the measured property of about a factor of 2. Of course, the area of the interface is different and the magnetization data also include the contribution of the grains, but even under these restrictions it might be possible that the origin of the large magnetization in Fig. 55(a) is a current across the ferromagnetic barrier. The presence of pinholes in our structures leading to the observed supercurrents cannot decisively be ruled out. However, correlations of transport and magnetization experiments clearly suggest that the current across the barrier is the origin of the observed effects. A particular and extraordinary temperature dependence of the junction current might be an indicator of a Josephson current across a ferromagnetic barrier in YBCO. Whether or not this is necessarily a triplet supercurrent governed by a reduced T_c remains unclear at the moment. A definite proof for the presence of a ferromagnetic Josephson junction in YBCO can only be given when observing a distinct Fraunhofer pattern.

This result will only be accessible when realizing high quality micron-sized junctions. This has not been achieved yet. In conclusion, we fabricated ultra-thin ferromagnetic LCMO layers in between two epitaxially grown YBCO films with different crystallographic orientations, namely, (110) and (001). We found a clear and unexpected ferromagnetic response of 1 nm and 2 nm thick LCMO films with ordering temperatures above $T=200$ K. In combination with YBCO films grown in (110)-orientation using sophisticated buffer layers, it is possible to realize a high- T_c SFS-junction with a ferromagnetic layer thinner than the in-plane coherence length ξ_{ab} of YBCO. We observe evidence of supercurrent transport across the ferromagnetic barrier. The barrier roughness and temperature and field dependence of the transport current strongly suggest that the observed transport current is flowing at least partly across the ferromagnet.

5. Conclusions and Outlook

In this work the development of a reliable method for the preparation of YBCO-LCMO (110)-oriented heterostructures has been accomplished. It could be shown that the YBCO-LCMO bilayers grow epitaxially, with the (110) planes of LCMO, YBCO, and STO parallel to each other. Admixtures of (001) and/or (103) grains of YBCO are below our detection limit. The charge transport and magnetic properties of the film are highly anisotropic, as expected based on the anisotropic electronic structure of YBCO. By mastering the technological difficulties to fabricate high quality single phase (110)-oriented YBCO-LCMO bilayers and exploring their macroscopic properties, a fundamental prerequisite for in-depth microscopic investigations of YBCO-LCMO interfaces where the CuO_2 planes of YBCO are oriented perpendicular to the substrate plane has been accomplished. Comparing the results of the macroscopic measurements with those of c-axis oriented bilayers of the same composition, we observe a reduction of T_c from 89K (c-axis oriented bilayers) to 75 K for (110) bilayers. This may indicate that in the case of the (110) bilayers the interactions at the interface generate a different orbital reconstruction, charge transfer and magnetic polarization at the YBCO side compared to the c-axis bilayers. More elaborate experiments using advanced resonant x-ray techniques remain a task for the future.

Additionally, trilayer structures have been fabricated with ultra-thin ferromagnetic LCMO layers in between two epitaxially grown YBCO films with different crystallographic orientations, namely, (110) and (001) with the intention to pave the way for a technology to produce planar Josephson junctions with ferromagnetic barriers. A clear and unexpected ferromagnetic response of 1 nm and 2 nm thick LCMO films with ordering temperatures above $T = 200\text{K}$ have been found. In combination with YBCO films grown in (110)-orientation using sophisticated buffer layers, it is possible to realize a high- T_c SFS-junction with a ferromagnetic layer thinner than the coherence length ξ_{ab} YBCO. We observe evidence of supercurrent transport across the ferromagnetic barrier. The barrier roughness and temperature and field dependence of the transport current strongly suggest that the observed transport current is flowing at least partly across the ferromagnet. The absence of Fraunhofer patterns in the

current-magnetic field characteristics is ascribed to the relatively large junction area. The existence of pinholes, however, can not be excluded yet.

Finally, a method has been explored growing twin free YBCO-LCMO trilayers in the (103)-orientation by using slightly off-cut (110)-oriented STO substrates. The experiments show an unexpected positive Meissner effect at the superconducting transition temperature which is tentatively ascribed to an interplay of Meissner screening currents and the domain structure of the ferromagnet via stray fields. The carefully performed magnetoresistance measurements show that in contrast to the conventional interface related GMR effect the switching of the magnetization direction in the FSF structure in the normal state is affected by the influence of the magnetoresistance of the YBCO layer.

The work presented here paves the way for in depth microscopic research activities analyzing the interface electronic structure of YBCO-LCMO heterostructures with the superconducting coherence length ξ_{ab} pointing perpendicular to the interface plane as well as research on the electronic transport across the thin ferromagnetic layer with two possible perspectives: (i) to fabricate oxide SFS Josephson junctions and (ii) to understand in detail the proximity effects in oxide SFS-structures with strong electronic correlation

References

- 1 Physics of Transition Metal Oxides, S. Maekawa ed. Springer (2004).
- 2 E. Dagotta, Nanoscale Phase Separation and Colossal Magnetoresistance, Springer Series in Solid Sciences Vol. 136, (2003)
- 3 Y. Tokura and Y. Tomioka, JMMM 200, 1 (1999)
- 4 K. v. Klitzing, G. Dorda, and M. Pepper, Phys. Rev. Lett. 45, 494-497 (1980).
- 5 P. Grünberg, R. Schreiber, Y. Pang, M. B. Brodsky, and H. Sowers, Phys. Rev. Lett. 57, 2442-2445 (1986).
- 6 A. Ohtomo, D. A. Muller, J. L. Grazul & H. Y. Hwang, Nature 247, 378-380, (2002)
- 7 N. Reyren, S. Thiel, A. D. Caviglia, L. Fitting Kourkoutis, G. Hammerl, C. Richter, C. W. Schneider, T. Kopp, A.-S. Rüetschi, D. Jaccard, M. Gabay, D. A. Muller, J.-M. Triscone, J. Mannhart, Science 317. 1196-1199, (2007)
- 8 S. Thiel, Hammerl G, Schmehl A, Schneider CW, Mannhart J, Science 313, 1942-1945, (2006).
- 9 Jak Chakhalian, JW Freeland, G Srajer, J Stremper, G Khaliullin, JC Cezar, T Charlton, R Dalgliesh, Ch Bernhard, G Cristiani, H-U Habermeier, B Keimer, Nature Physics 2, 244-246, (2006).
- 10 Science 317, 1844, (2007).
- 11 MRS Bulletin 33 No 11 (2008).
- 12 J. Mannhart and D. G. Schlom, Science 327, 1607 (2010).
- 13 H. Y. Hwang, Y. Iwasa, M. Kawasaki, B. Keimer, N. Nagaosa and Y. Tokura, Nature Mat. 11, 103, (2012)
- 14 E. Benckiser et al Nature Mat. 10, 189, (2011)
- 15 V. V. Ryazanov et al., Phys. Rev. Lett., 86, 2427-2430 (2001)
- 16 J Chakhalian, JW Freeland, H-U Habermeier, G Cristiani, G Khaliullin, M Van Veenendaal, B Keimer, Science 318, 1114-1117, (2007).
- 17 P. Prieto, P. Vivas, G. Campillo, E. Baca, L. F. Castro, M. Varela, C. Ballesteros, J. E. Villegas, D. Arias, C. León and J. Santamaría, J. Appl. Phys. 89, 8026 -8029, (2001).

- 18 H.-U. Habermeier, G. Cristiani, R.K. Kremer, O. Lebedev, G. van Tendeloo, *Physica C* 364, 298-304, (2001).
- 19 P. Przysławski, I. Komissarov, P. Dłużewski, J. Pełka, E. Dynowska, M. Sawicki, *Physica C* 387, 40-43, (2003).
- 20 Z. Sefrioui et al., *Appl. Phys. Lett.* 81, 4568-4570, (2002).
- 21 S. Poelders, R. Auer, G. Linker, R. Smithey, R. Schneider. *Physica C* 247, 309-318 (1995).
- 22 H Kamerlingh Onnes, *Leiden Comm.* 120b 122b, 124c (1911)
- 23 W. Meissner, R. Ochsenfeld, *Naturwissenschaften* 21 (1933) 787
- 24 E. Maxwell, *Phys. Rev.* 78 (1950) 477
- 25 J. Bardeen, L. N. Cooper, and J. P. Schrieffer, *Phys. Rev.* 106 (1957) 162
- 26 J. R. Gavaler, *Appl. Phys. Lett.* 23 (1973) 480
- 27 J. G. Bednorz, K. A. Muller, *Zeitschrift für Physik B*, Volume 64 (1986) 189
- 28 M.K. Wu, J.R. Ashburn, C. J. Torng et al. *Phys. Rev. Lett.*, Vol 58 (1987) 908
- 29 R.J. Cava, B. Batlogg, R.B. van Dover, D. M. Murphy, S. Sunshine, T. Siegrist, J.P. Remeika, E. A. Rietman, S. Zahurak, and G.P. Espinosa, *Phys. Rev. Lett.* 58 (1987)
- 30 C. W. Chu, *Nature* 365 (1993) 323
- 31 J. Zaanen, *Nature Phys.* 2 138 (2006).
- 32 H.F. Poulsen, N.H. Andersen, J.V. Andersen, H. Bohr, and O.G. Mouritsen, *Nature*, Vol 349, 594(1991).
- 33 P. Monthoux, A. V. Balatsky, and D. Pines, *Phys. Rev B* 46 (1992) 14803
- 34 R.J. Cava, B. Batlogg, R.B. van Dover, D. M. Murphy, S. Sunshine, T. Siegrist, J.P. Remeika, E. A. Rietman, S. Zahurak, and G.P. Espinosa, *Phys. Rev. Lett.* 58 (1987), 1676 .
- 35 A. K. Saxena, *High Temperature Superconductors*, Springer Series in Materials Science Vol 125, (2010= p.42)
- 36 F. Beech, S. Miraglia, A. Santoro, and R. S. Roth, *Phys. Rev.B* , vol 35 (1987), 8778
- 37 J. D. Jorgensen, B. W. Veal , W. K. Kwok, G. W. Crabtree, A. Umezawa, L. J. Nowicki, and A. P. Paulikas, *Phys. Rev.B*, vol 36 (1987), 5731
- 38 P. A. Lee, N. Nagaosa and X.-G. Wen, *Rev. of Modern Phys.* , vol 78, 17 (2006)

- 39 B. Keimer et al. Nature 518 (2015) 179.
- 40 J.L. Tallon, G.V.M. Williams, J.W. Loram, Physica C, 338 (2000) 9.
- 41 G. Deutscher and K. A. Muller, Phys. Rev. Lett. 59 (1987) 1745.
- 42 D. Dimos, P. Chaudhari, J. Mannhart, and F. K. Legues, Phys. Rev. Lett. 61 (1988) 219.
- 43 M. Schuisky, J. W. Elam and S. M. George, Appl. Phys. Lett. 81, 180 (2002).
- 44 E. Llobet, X. Vilanova, J. Brezmes, R. Alcubilla, J. Calderer, J. E. Sueiras and X. Correig, Meas. Sci. Technol. 8, 1133 (1997).
- 45 R. von Helmolt, J. Wecker, B. Holzapfel, L. Schultz and K. Samwer, Phys. Rev. Lett. 71, 2331 (1993).
- 46 S. Jin, T. H. Tiefel, M. McCormack, R. A. Fastnacht, R. Ramesh and L. H. Chen, Science 264, 413 (1994).
- 47 E. Dagotto, New J. Phys. 7, 67 (2005).
- 48 S. Soltan, Dissertation, University of Stuttgart, 2005, p
- 49 S. S. P. Parkin, Ann. Rev. Mater. Sci. 25, 357 (1995).
- 50 A. Gupta and J. Z. Sun, J. Magn. Magn. Mater. 200, 24 (1999).
- 51 J. M. D. Coey, M. Viret and S. von Molnár, Adv. Phys. 48, 167 (1999).
- 52 M.-H. Jo, N. D. Mathur, J. E. Evetts and M. G. Blamire, Appl. Phys. Lett. 77, 3803 (2000).
- 53 J. Fleig, Annu. Rev. Mater. Res. 33, 361(2003).
- 54 V. Brichzin, J. Fleig, H.-U. Habermeier, G. Cristiani and J. Maier, Solid State Ionics 152, 499 (2002).
- 55 J. Fleig, F. S. Baumann, V. Brichzin, H.-R.Kim, J. Jamnik, G. Cristiani, H.-U. Habermeier and J. Maier, Fuel Cells 06, 284 (2006).
- 56 J. B. Goodenough, Rep. Prog. Phys. 67, 1915 (2004).
- 57 Y. Tokura, *Fundamental features of colossal magnetoresistive manganeseoxides* (Gordon & Breach, London, 1999).
- 58 J. A. M. van Roosmalen and E. H. P. Cordfunke, J. Solid State Chem., 93, 212 (1991)
- 59 J. A. M. van Roosmalen, E. H. P. Cordfunke, R. B. Helmholtz and H. W. Zandbergen, J. Solid State Chem. 110, 100 (1994).
- 60 L. Malavasi, C. Ritter, M. C. Mozzati, C. Tealdi, M. S. Islam, C. B. Azzoni and G.

- Flor, J. *Solid State Chem.* 178, 2042 (2005).
- 61 L. Malavasi, C. Ritter, M. C. Mozzati, C. Tealdi, C. B. Azzoni, G Chiodelli and G. Flor, *Solid State Comm.* 123, 321 (2002).
- 62 I. Walha, W. Boujelben, M. Koubaa, A. Chelkh-Rouhou and A. M. Haghiri-Gosnet, *Phys. Stat. Sol.* 201, 1416 (2004).
- 63 F. A. Kröger and H. J. Vink, *Solid State Physics Advances in Research and Applications* (Academic, New York, 1957).
- 64 V. Goldschmidt, *Geochemistry* (Oxford University Press, London, 1958).
- 65 A. P. Ramirez, *J. Phys.:Condens. Matter* 9, 8171 (1997).
- 66 C. N. R. Rao, A. K. Cheetham, R. Mahesh, *Chem. Matter* 8, 2421 (1996).
- 67 M. B. Salamon and M. Jaime, *Rev. Mod. Phys.* 73, 583 (2001).
- 68 S. W. Cheong and H. Y. Hwang, *Ferromagnetism vs charge orbital ordering in mixed valent manganites in colossal magnetoresistance oxides* (Gordon and Breach, London (1999).
- 69 T. Hotta, S. Yunoki, M. Mayr and E. Dagotto *Phys. Rev.* 60, R15009 (1999).
- 70 G. H. Jonker and J. H. van Santen, *Physica* 16, 337 (1950).
- 71 J. H. van Santen and G. H. Jonker, *Physica* 16, 599 (1950).
- 72 C. Zener, *Phys. Rev.* 82, 403 (1951).
- 73 P. W. Anderson and H. Hasegawa *Phys. Rev.* 100, 675 (1955).
- 74 J. B. Goodenough, *Phys. Rev.* 100, 564 (1955).
- 75 M. Atanasov and S. Angelov, *Chem. Phys.* 150, 383 (1991).
- 76 Y. Tokura and Y. Tomioka, *J. Magn. Magn. Mater.* 200, 1 (1999).
- 77 C. N. R. Rao and B. Raveau, *Colossal Magnetoresistance, Charge Ordering and Related Properties of Manganese Oxides* (World Scientific, Singapore, 1998).
- 78 H. A. Jahn and E. Teller, *Proc. R. Soc. London Ser. A* 161, 220 (1937).
- 79 H. S. Wang, E. Wertz, Y. F. Hu, Q. Li and D. G. Schlom, *J. Appl. Phys.* 87, 7409 (2000).
- 80 L. Ranno, A. Llobet, M. B. Hunt and J. Pierre, *Appl. Surf. Sci.* 138-139, 228 (1999).
- 81 N. C. Yeh, R. P. Vasquez, D. A. Beam, C. C. Fu, J. Huynh and G. Beach, *J. Phys.:*

- Condens. Matter 9, 3713 (1997).
- 82] V. Trtik, F. Sanchez, M. Varela, M. Bibes, B. Martinez and J. Fontcuberta, J. Magn. Mater. 203, 256 (1999).
- 83 O. Yu Gorbenko, I. E. Graboy, A. R. Kaul and H. W. Zandbergen, J. Magn. Mater. 211, 97 (2000).
- 84 M. Ziese, H. C. Semmelhack, K. H. Han, S. P. Sena and H. J. Blythe, J. Appl. Phys. 91, 9930 (2002).
- 85 T. Walter, K. Dörr, K. H. Müller, D. Eckert, K. Nenkov, M. Hecker, M. Lehmann and L. Schultz, J. Magn. Mater. 222, 175 (2000).
- 86 J. Z. Sun, D. W. Abraham, R. A. Rao and C. B. Eom, Appl. Phys. Lett. 74, 3017, (1999).
- 87 M. Sahana, T. Walter, K. Dörr, K.-H. Müller, D. Eckert and K. Brand, J. Appl. Phys. 89, 6834 (2001).
- 88 R. B. Praus, B. Leibold, G. M. Gross and H.-U. Habermeier, Appl. Sur. Sci. 138-139, 40 (1999).
- 89 M. Bibes, Ll. Balcells, S. Valencia, J. Fontcuberta, M. Wojcik, E. Jedryka and S. Nadolski, Phys. Rev. Lett. 87, 067210 (2001).
- 90 J. Aarts, S. Freisem, R. Hendrikx and H. W. Zandbergen, Appl. Phys. Lett. 72, 2975 (1998).
- 91 J. R. Sun, C. F. Yeung, K. Zhao, L. Z. Zhou, C. H. Leung, H. K. Wong and B. G. Shen, Appl. Phys. Lett. 76, 1164 (2000).
- 92 E. Beyreuther, S. Grafström, L. M. Eng, C. Thiele and K. Dörr, Phys. Rev. B 73, 155425 (2006).
- 93 B. Vengalis, V. Lissauskas, V. Pyragas, K. Sliuziene, A. Oginskis, A. Cesnys, J. Santiso and A. Figueras, J. Phys. IV 11, 209 (2001).
- 94 L. Malavasi, I. Alessandri, M. C. Mozzati, P. Ghigna, G. Chiodelli, C. B. Azzoni and G. Flor, Phys. Chem. Chem. Phys. 5, 2274 (2003).
- 95] H. Vincent, M. Audier, S. Pignard, G. Dezanneau and J. P. Senateur, J. Magn. Mater. 226-230, 788 (2001).
- 96 Srinivas V. Pietambaram, D. Kumar, Rajiv K. Singh and C. B. Lee, MRS Sympo.

- Proceed. 617, J 3.14.1 (2000).
- 97 S. W. Jin, X. Y. Zhou, W. B. Wu, C. F. Zhu, H. M. Weng, H. Y. Wang, X. F. Zhang, B. Ye and R. D. Han, *J. Phys. D: Appl. Phys.* 37, 1841 (2004).
- 98 J. R. Sun, H. W. Yeung, H. K. Wong, T. Zhu and B. G. Shen, *Eur. Phys. J. B* 35, 481 (2003).
- 99 A. Tebano, G. Balestrino, N. G. Boggio, C. Aruta, B. Davidson and P. G. Medaglia *Eur. Phys. J. B* 51, 337 (2006).
- 100 S. Degoy, J. Jiménez, P. Martín, O. Martínez, A. C. Prieto, D. Chambonnet, C. Audry, C. Belouet, J. Perrière, *Physica C: Superconductivity*, 256, 291-297, (1996).
- 101 W. Prellier, M. Rajeswari, T. Venkatesan and R. L. Greene, *Appl. Phys. Lett.* 75, 1446 (1999).
- 102 V. L. Ginzburg, *Zh. Eksp. Teor. Fiz.* 31, 202 (1956)
- 103 M. B. Maple, *Physics C* 341-348, 47 (2000).
- 104 A. I. Larkin and Y. N. Ovchinnikov, *Zh. Eksp. Teor. Fiz.* 47, 1136 (1964).
- 105 P. Fulde and R. A. Ferrell, *Phys. Rev.* 141, A550 (1964).
- 106 C. Bernhard, J. L. Tallon, Ch. Niedermayer, Th. Blasius, A. Golnik, E. Brücher, R. K. Kremer, D. R. Noakes, C. E. Stronach, J. Ansaldo, *Phys. Rev. B* 59 14099 (1999).
- 107 M. Varela, Zouhair Sefrioui, D. Arias, M. A. Navacerrada, M. Lucía, M. A. Lopez de La Torre, C. León, G. D. Loos, F. Sánchez-Quesada, J. Santamaría *Solid-State Electron.* 47, 2245 (2003).
- 108 J. Chakhalian, J. W. Freeland, G. Srajer, J. Stremper, G. Khaliullin, J. C. Cezar, T. Charlton, R. Dagliesh, C. Bernhard, G. Cristiani, H.-U. Habermeier, and B. Keimer, *Nature Physics* 2, 244 (2006).
- 109 N. Driza, S. Blanco-Canosa, M. Bakr, S. Soltan, M. Khalid, L. Mustafa, K. Kawashima, G. Cristiani, H.-U. Habermeier, G. Khaliullin, C. Ulrich, M. Le Tacon, and B. Keimer, *Nature Materials* 11, 675 (2012).
- 110 J. F. Ready, *Appl. Phys. Lett.* 3, 11 (1963), 117
- 111 R. M. White, *J. Appl. Phys.* 43, 3559 (1963).
- 112 K. Tomiyasu, *Laser bibliography II, IEEE Journal of Quantum Electronics* Volume: 1, Issue: 5, (1965).
- 113 H. M. Smith and A. F. Turner, *Appl. Opt.* 4, 147 (1965).

- 114 D. Dijkkamp, T. Venkatesan, X. D. Wu, S. A. Shaheen, N. Jisrawi, Y. H. Minlee, W. L. McLean and M. Croft, *Appl. Phys. Lett.* 51, 619 (1987).
- 115 S. M. Metev and V. P. Veiko, *Laser Assisted Microtechnology* (Springer, Berlin, Heidelberg, 1994).
- 116 J. F. M Cillessen, *Pulsed Laser Deposition of Oxide Film* (Philips electronics N.V., 1996)
- 117 T. A. Vanderah, *Chemistry of Superconducting Oxides* (Noyes Publications, N. Y. , 1991)
- 118 I. D. Raistrick in *Interfaces in High T_c Superconducting Systems*, S. L. Shinde and A. Rudman eds. (Springer Verlag Berlin, 1994)
- 119 Somekh, R. E., et al. In *Concise Encyclopedia of Magnetic and Superconducting Materials*, Evetts, J. (ed.), Pergamon Press, Oxford, (1992).
- 120 H.-U. Habermeier, A.A.C.S. Lourenco, B.Leibold, J.Kircher, and B. Friedl. in *High T_c Superconductor Thin Films*, L. Correr Edt. Elsevier 1992, p. 343.
- 121 L. Mustafa, N. Driza, M. Le Tacon, H.-U. Habermeier, B. Keimer, *Physica C* 505, 70 (2014)
- 122 C. Thomsen, *Adv. Mater.* 4, 341 (1992)
- 123 M. Bakr, A. P. Schnyder, L. Klam, D. Manske, C. T. Lin, B. Keimer, M. Cardona, and C. Ulrich . *Phys. Rev. B* 80, 064505 (2009)
- 124 K. F. McCarty, *Phys. Rev. B* 13 (1999).
- 125 C. Thomsen, R. Liu, A. Wittlin, L. Genzel, M. Cardona, W. König, M.V. Cabañas, E. García., *Sol. Stat. Com.* Vol 65, No. 1, 1988.
- 126 Lebedev, OI, Van Tendeloo, G; Amelinckx, S; Leibold, B. and Habermeier H.-U. *Phys. Rev. Lett.* B 58, 8065 (1998)
- 127 T. K. Nath, R. A. Rao, D. Lavric, C. B. Eom, L. Wu and F. Tsui , *Appl. Phys. Lett.* 74, 1615 (1999)
- 128 V. Moshnyaga, B. Damaschke, O. Shapova², A. Belenchuk, J. Faupel, O. I. Lebedev, J. Verbeeck, G. van Tendeloo, M. Mücksch, V. Tsurkan, R. Tidecks & K. Samwer, *Nature Mat.* 2, 247 (2003)
- 129 K. Kawashima, G. Logvenov, G. Christiani, H.-U. Habermeier, *J. MMM* 376, 539 (2015).

- 130 I. C. Infante, F. Sánchez, J. Fontcuberta, S. Fusil, K. Bouzehouane, G. Herranz, A. Barthélémy, S. Estradé, J. Arbiol, F. Peiró, R. J. O. Mossaneck, M. Abbate and M. Wojcik , J. Appl. Phys. 101, 093902 (2007).
- 131 Y. Li, J. R. Sun, J. Zhang, and B. G. Shen, J. Appl. Phys. 116, 043916 (2014).
- 132 U. Scotti di Uccio), F. Lombardi, F. Miletto Granozio, Physica C 323, 51 (1999)
- 133 D. K. Satapathy, M. A. Uribe-Laverde, I. Marozau, V. K. Malik, S. Das, Th. Wagner, C. Marcelot, J. Stahn, S. Brück, A. Rühm, S. Macke, T. Tietze, E. Goering, A. Frañó, J. -H. Kim, M. Wu, E. Benckiser, B. Keimer, A. Devishvili, B. P. Toperverg, M. Merz, P. Nagel, S. Schuppler, and C. Bernhard, Phys. Rev. Lett. 108, 197201 (2012).
- 134 A. Di Bernardo, Z. Salman, X. L. Wang, M. Amado, M. Egilmez, M. G. Flokstra, A. Suter, S. L. Lee, J. H. Zhao, T. Prokscha, E. Morenzoni, M. G. Blamire, J. Linder, and J. W. A. Robinson, Phys. Rev. X 5, 041021 (2015).
- 135 M. A. López de la Torre, V. Peña, Z. Sefrioui, D. Arias, C. Leon, J. Santamaria, and J. L. Martinez, Phys. Rev. B 73, 052503 (2006).
- 136 C. Z. Chen, C. B. Cai, L. Peng, Z. Y. Liu, Y. M. Lu, H. W. Wang and X. M. Xie, EPL, 83 37005 (2010).
- 137 Hong-ye Wu, Jing Ni, Jian-wang Cai, Zhao-hua Cheng, and Young Sun, Phys. Rev. B, 76 024416 (2007).
- 138 C. Monton, F. de la Cruz, and J. Guimpel, Phys. Rev. B, 77 104521 (2008).
- 139 G. A. Ovsyannikov , V. V. Demidov, Yu. N. Khaydukov, L. Mustafa, K. Y. Constantinian, A. V. Kalabukhov, and D. Winkler, JETP, 122 (2016) 738.
- 140 C. P. Bean and J. D. Livingston, Phys. Rev. Lett., 12 14 (1964).
- 141 L. N. Bulaevskii, V. V. Kuzii, and A. A. Sobyanin, JETP Lett. 25, 290, (1977).
- 142 A. I. Buzdin, L. N. Bulaevskii, and S. V. Panyukov, JETP Lett. 35, 178 (1982).
- 143 V. V. Ryazanov, V. A. Oboznov, A. Yu. Rusanov, A. V. Veretennikov, A. A. Golubov, and J. Aarts, Phys. Rev. Lett. 86, 2427 (2001).
- 144 T. Kontos, M. Aprili, J. Lesueur, F. Genet, B. Stephanidis, and R. Boursier, Phys. Rev. Lett. 89, 137007 (2002).
- 145 R. S. Keizer, S. T. B. Goennenwein, T. M. Klapwijk, G. Miao, G. Xiao, and A. Gupta, Nature

- 439 , 825 (2006).
- 146 J. W. A. Robinson, J. D. S. Witt, and M. G. Blamire, *Science* 329, 59 (2010).
- 147 T. S. Khaire, M. A. Khasawneh, W. P. Pratt, Jr., and N. O. Birge, *Phys. Rev. Lett.* 104, 137002 (2010).
- 148 M. Eschrig, J. Kopu, J. C. Cuevas, and G. Schön, *Phys. Rev. Lett.* 90, 137003 (2003).
- 149 M. Eschrig and T. Lofwander, *Nat. Phys.* 4, 138 (2008).
- 150 F. S. Bergeret, A. F. Volkov, and K. B. Efetov, *Rev. Mod. Phys.* 77, 1321 (2005).
- 151 K. Dybko, K. Werner-Malento, P. Aleshkevych, M. Wojcik, M. Sawicki, and P. Przyslupski, *Phys. Rev. B* 80, 144504 (2009).
- 152 T. Hu, H. Xiao, C. Visani, Z. Sefrioui, J. Santamaria, and C. C. Almasan, *Phys. Rev. B* 80, 060506 (2009).
- 153 M. Alidoust, J. Linder, G. Rashedi, T. Yokoyama, and A. Sudbø, *Phys. Rev. B* 81, 014512 (2010).
- 154 M. van Zalk, A. Brinkman, J. Aarts, and H. Hilgenkamp, *Phys. Rev. B* 82, 134513 (2010).
- 155 J. Y. T. Wei, N.-C. Yeh, C. C. Fu, and R. P. Vasquez, *J. Appl. Phys.* 85, 5350 (1999).
- 156 S. Soltan, J. Albrecht, and H.-U. Habermeier, *Solid State Commun.* 135, 461 (2005).
- 157 T. K. Worthington, W. J. Gallagher, and T. R. Dinger, *Phys. Rev. Lett.* 59, 1160 (1987).
- 158 K. Winzer and G. Kumm, *Z. Phys. B* 82, 317 (1991).
- 159 G. Jakob, V. V. Moshchalkov, and Y. Bruynseraede, *Appl. Phys. Lett.* 66, 2564 (1995).
- 160 Z. Sefrioui, D. Arias, V. Pena, J. E. Villegas, M. Varela, P. Prieto, C. Len, J. L. Martinez, and J. Santamaria, *Phys. Rev. B* 67, 214511 (2003).
- 161 S. Soltan, J. Albrecht, and H.-U. Habermeier, *Phys. Rev. B* 70, 144517 (2004).
- 162 V. Pena, Z. Sefrioui, D. Arias, C. Leon, J. Santamaria, J. L. Martinez, S. G. E. Velthuis, and A. Hoffmann, *Phys. Rev. Lett.* 94, 057002 (2005).
- 163 Z.L. Zhang, U. Kaiser, S. Soltan, H.-U. Habermeier, and B. Keimer, *Appl. Phys. Lett.* 95, 242505 (2009).
- 164 J. Albrecht, S. Soltan, and H.-U. Habermeier, *Phys. Rev. B* 72, 092502 (2005).
- 165 M.S. Anwar, F. Czeschka, M. Hesselberth, M. Porcu, and J. Aarts, *Phys. Rev. B* 82, 100501(R) (2010).

Acknowledgments

This work would have not been possible without the help of numerous people inside and outside the institute. I am deeply indebted to all of them and here I would like to thank them for all there help and support.

First, and foremost, I would like to express my sincere gratitude to Prof. Bernhard Keimer who welcomed me to the Max Planck Institute and gave me the opportunity to do this work in his group. I am very grateful for his continuous support throughout this work and for his patience, motivation and good advice in the times where I really needed it.

I also would like to thank Prof. M. Dressel for acting as second referee for this thesis and Prof. Draghofer for being the head of my promotion committee.

I'm very grateful to Prof. Hanns-Ulrich Habermeier, the direct supervisor of my thesis who welcomed me in the Technology group and supported me in every step I took in this work. I will always be thankful for his guidance and for his open door for my questions. His advice is always appreciated and the discussions we had, proved to be fruitful and encouraging.

I am very thankful for Dr. Gennady Logvenov, the head of the Technology group, for his support and the fruitful discussions we had. I am also grateful for Yury Khaydukov and Soltan Soltan for their continuous support and insightful suggestions. Many thanks for Eva Benckiser and Mathieu Le Tacon for the interesting discussions.

I am grateful for Armin Schulz, Maritta Dudek and Michael Schulz for their continuous technical support.

I would like to thank all the members of the Technology group for their support during my time at the institute. Special thanks go to Georg Cristiani, Benjamin Stuhlhofer, Birgit Lemke, Stephan Schmid and Yvonne Stuhlhofer for their continuous technical support and sample preparation. I've enjoyed their company and felt as a part of this team.

I am very thankful for my colleagues, Ingo Fritsch, Peter Yordanov, Nadir Driza, Kazuhiro Kawashima and Stefan Heinze and all the member of Prof. Keimer's group for all the good time we shared together and for the lovely environment they created.

Finally, I would like to deeply thank my beloved parents and family in Zarqa and Stuttgart. Without their unconditional love, support and guidance, this work would have never been realized.

Publication list:

- L. Mustafa, N. Driza, S. Soltan, M. Le Tacon, H.-U. Habermeier and B. Keimer: Structural and electronic properties of epitaxial $\text{YBa}_2\text{Cu}_3\text{O}_{7-\delta}\text{-La}_{0.67}\text{Ca}_{0.33}\text{MnO}_3$ bilayers grown on SrTiO_3 (110) substrates; *Physica C* 505 70-73 (2014).
- S. Soltan, J. Albrecht, E. Goering, G. Schütz, L. Mustafa, B. Keimer, and H.-U. Habermeier: Preparation of a ferromagnetic barrier in $\text{YBa}_2\text{Cu}_3\text{O}_{7-\delta}$ thinner than the coherence length; *Journal of Applied Physics* 118, 223902 (2015).
- Yu. N. Khaydukov, G. A. Ovsyannikov, A. E. Sheyerman, K. Y. Constantinian, L. Mustafa, T. Keller, M. Uribe-Laverde, Yu. V. Kislinskii, A. V. Shadrin, A. Kalaboukhov, B. Keimer, and D. Winkler : Evidence for spin-triplet superconducting correlations in metal-oxide heterostructures with noncollinear magnetization; *PRB* 90, 035130 (2014).
- G A Ovsyannikov , K Y Constantinian¹, A E Sheerman, A V Shadrin, Yu V Kislinski, Yu N Khaydukov, L Mustafa, A Kalabukhov and D Winkler: Triplet superconductivity in oxide ferromagnetic interlayer of mesa-structure; *Journal of Physics: Conference Series* 592 012136 (2015).
- N. Driza, S. Blanco-Canosa, M. Bakr, S. Soltan, M. Khalid, L. Mustafa, K. Kawashima, G. Christiani, H-U. Habermeier, G. Khaliullin, C. Ulrich, M. Le Tacon and B. Keimer: Long-range transfer of electron–phonon coupling in oxide superlattices; *Nature Materials* 11, 675–681 (2012).

- G. A. Ovsyannikov, V. V. Demidov, Yu. N. Khaydukov, L. Mustafa, K. Y. Constantinian, A. V. Kalabukhov, and D. Winkler: Magnetic Proximity Effect at the Interface between a Cuprate Superconductor and an Oxide Spin Valve; JOURNAL OF EXPERIMENTAL AND THEORETICAL PHYSICS Vol. 122 No. 4 pp. 738–747 (2016).
- A. M. Petrzhik, G. A. Ovsyannikov, A. V. Shadrin, Yu. N. Khaidukov, and L. Mustafa: Spin Transport in Epitaxial Magnetic Manganite/Ruthenate Heterostructures with an LaMnO₃ Layer; Journal of Experimental and Theoretical Physics, 2014, Vol. 119, No. 4, pp. 745–752. (2014).
- Y. Khaydukov, R. Morari, L. Mustafa, J.-H. Kim, T. Keller, S. Belevski, A. Csik, L. Tagirov, G. Logvenov, A. Sidorenko and B. Keimer: Structural, Magnetic, and Superconducting Characterization of the CuNi/Nb Bilayers of the S/F Type Using Polarized Neutron Reflectometry and Complementary Techniques; J Supercond Nov Magn 28:1143–1147 (2015).
- Karén Constantinian, Gennady Ovsyannikov, Alexander Sheyerman, Yulii Kislinskii, Anton Shadrin, Alexei Kalaboukhov, Luqman Mustafa, Yurii Khaydukov, and Dag Winkler: Spin-Triplet Superconducting Current in Metal–Oxide Heterostructures With Composite Ferromagnetic Interlayer; IEEE TRANSACTIONS ON APPLIED SUPERCONDUCTIVITY, VOL. 26, NO. 3, APRIL (2016).
- B. Nagy, Yu. Khaydukov, D. Efremov, A. S. Vasenko, L. Mustafa, J.-H. Kim, T. Keller, K. Zhernenkov, A. Devishvili, R. Steitz, B. Keimer and L. Bottyan: On the Explanation of the Paramagnetic Meissner Effect in Superconductor/Ferromagnet Heterostructures, submitted.

Declaration of Authorship:

I hereby certify that the dissertation entitled

“Magnetic and Transport Properties of $\text{YBa}_2\text{Cu}_3\text{O}_7 - \text{La}_{0.7}\text{Ca}_{0.3}\text{MnO}_3$ Heterostructures”

is entirely my own work except where otherwise indicated. Passages and ideas from other sources have been clearly indicated.

Stuttgart, 31.10.2016



Luqman Mustafa